Dissertation zur Erlangung des Doktorgrades

der Fakultät für Chemie und Pharmazie

der Ludwig-Maximilians-Universität München

Solution Processed Perovskite Solar Cells

Fabian Cornelius Alban Hanusch

aus

München, Deutschland

2015

Erklärung

Diese Dissertation wurde im Sinne von § 7 der Promotionsordnung vom 28. November 2011

von Herrn Prof. Dr. Thomas Bein betreut.

Eidesstattliche Versicherung

Diese Dissertation wurde eigenständig und ohne unerlaubte Hilfe bearbeitet.

München, 20.08.2015

Fabian Hanusch

Dissertation eingereicht am 24.08.2015

1. Gutachter: Prof. Dr. Thomas Bein

2. Gutachter: Prof. Dr. Dina Fattakhova-Rohlfing

Mündliche Prüfung am 15.10.2015

1 Danksagung

Ich möchte mich zuerst einmal bei meinem Doktorvater Prof. Dr. Thomas Bein für die wiederholte Aufnahme in seine Gruppe für Bachelor-, Master- und Doktorarbeit bedanken. Er gab mir immer die Möglichkeit an sehr interessanten Forschungsprojekten zu arbeiten und hat durch die Diversität in den Forschungsbereichen mein Interesse an den unterschiedlichsten Aspekten der physikalischen Chemie geweckt.

Des Weiteren danke ich Frau Prof. Dr. Dina Fattakhova-Rohlfing, die sich bereit erklärt hat meine Doktorarbeit als zweite Gutachterin zu bewerten. Vielen Dank auch für die zahlreichen Ratschläge, wie ich meine Forschungsergebnisse mit Hilfe von elektrochemischen Experimenten unterstützen kann.

Dr. Pablo Docampo möchte ich herzlich dafür danken, dass er die Leitung meiner Perowskit Projekte übernommen hat. Ohne ihn und seine ständige Motivation wäre es vermutlich nicht möglich gewesen so schnell so viele Ergebnisse zu produzieren. Ich hatte viel Spaß dabei gemeinsam das Labor umzuräumen und einzurichten. Unseren Forschungsaufenthalt in Oxford (Dank an Prof. Snaith) werde ich wohl nie vergessen (4000 Solarzellen in 2 Wochen).

In diesem Zusammenhang möchte ich auch allen meinen hausinternen und -externen Kollaborationspartnern danken. Ohne euch wären viele Projekte nicht möglich gewesen. Genauso haben auch alle meine Praktikanten, egal ob einheimisch oder international durch das NIM Summer Research Program, sehr viel Arbeit in die erreichten Ergebnisse gesteckt und einen wichtigen Beitrag zu meiner Promotion geleistet. Danke Emily, Frederik, Nayyera, Christina, Philipp, Jürgen und Simon.

Auch wenn meine Subgroup im Laufe der Jahre immer wieder den Namen gewechselt hat sind die Kollegen doch immer gleich angenehm und der Input aus Diskussionen gleich hochwertig geblieben. Vielen Dank an alle Ex-Subgroup Mitglieder (Keili, Johann, Jörg, Benni, Flo, Askhat, Alesja, Halina, Dina, Kun, Norma, Hans, Markus) und an alle, die immer noch alle zwei Wochen aufstehen müssen (Andi, Enrico, Tina, Meltem, Hongi, Nadja, Pablo, Michiel).

Regina und Tina, ich möchte euch meinen tiefsten Dank aussprechen, dass ihr hier immer alles am Laufen haltet. Seien es labortechnische Probleme (warum haben wir eigentlich 3 verschiedene Orte für Swagelok Verbindungen?), vergessene Reisegenehmigungen oder die

Abstract

Today's carbon-based economy will not be sustainable in the future. Not only will the known reserves of fossil fuels, like oil, natural gas or coal, be significantly reduced within the next 100 years, but the continued burning of fossil fuels also emits greenhouse gases, which have led to a global increase in temperature, called global warming. To preserve the environment for future generations and to prepare for the time when we will inevitably run out of fossil fuel, we have to change the way we produce our primary energy and focus research and investments on renewable energy sources. While energy from wind and water is already harvested with very high efficiencies, the utilization of solar energy still offers big room for improvements. Although conventional crystalline silicon cells achieve efficiencies around 25 %, their production is very energy intensive and relies on advanced production technologies, which makes them still rather expensive. To make photovoltaics a major part of our energy landscape, an easily prepared type of solar cell consisting of cheap and abundant materials is required.

Novel organometal halide perovskite-type materials fulfill these requirements and have proven to be serious competitors for conventional photovoltaics. After only four years of research they already achieve power conversion efficiencies above 20 %.

This thesis introduces a fast and easy way to prepare planar heterojunction solar cells based on methylammonium lead iodide ($MAPbI_3$). The photoactive layer is deposited in a 2-step deposition approach, where a thin film of the lead precursor is converted into the final perovskite simply by immersing it into a solution of the other component. The resulting films consist of individual crystals sizes a few 100 nm and covering the whole substrate without significant gaps or holes. Solar cells prepared by this method achieve power conversion efficiencies of 15 %. Furthermore, by adjusting the temperature of the immersion bath, the orientation of the perovskite crystals can be controlled. The orientation, together with the

resulting change in efficiency and resistance, gives interesting insights into the anisotropic charge transport properties of this class of materials.

Additionally, the conventionally used hole blocking layer, titanium dioxide, was replaced by one made of fullerene molecules. The efficiencies achieved by solar cells employing this kind of electron selective contact reached almost 10 %, although the reproducibility was initially very low. This was attributed to a partial dissolution of the fullerene film during the subsequent preparation steps. To increase the stability of the layer, it was photo-polymerized using UV radiation. This not only reduces the solubility and therefore increases the fraction of solar cells achieving high efficiencies; it also changed the energy levels close to the bandgap.

The bandgap energy of organic lead halide perovskite materials is strongly dependent on the composition. By exchanging some or all of the iodide in $MAPbI_3$ with bromide, the difference between valence and conduction band can be changed from 1.5 eV (pure iodide) to 2.25 eV (pure bromide). This substitution can be performed gradually, so that phase pure materials with properties in between the two extremes are obtained. The pure bromide $MAPbBr_3$ perovskite, however, does not perform efficiently in a planar heterojunction solar cell. Its close relative based on formamidinium $FAPbBr_3$ has also been investigated for its suitability as active solar cell material. Although it is structurally very similar to $MAPbBr_3$, with equivalent light absorption and emission properties, a 10 fold higher efficiency was observed for the FA-based compound. This striking difference is mainly attributed to an increased photoluminescence lifetime, resulting in an increased diffusion length of the free charge carriers.

Apart from their application as light absorbing materials in solar cells, perovskites have also been investigated for their application as light emitters. Depending on the perovskite used, it was possible to demonstrate red light emission ($MAPbI_3$) or green emission ($MAPbBr_3$).

Table of contents

2   Introduction

2.1   The Global Energy Challenge

Today's energy landscape is dominated by the use of fossil fuels, like oil, natural gas and coal. These types of energy carrier took millions of years to be formed and thus humankind will run out of them sooner or later.[1] New forms of energy will have to be utilized to sustain our energy intake past this point. But the development of so-called renewable energies, like wind, tide and solar, is not only driven by the need to satisfy our ever-growing demand for energy. Continuously burning fossil fuels over the past 150 years and the concurrent release of the combustion products into the atmosphere has caused a so-called greenhouse effect. This means that the energy emitted from the sun and being reflected from the earth cannot be emitted back into space as efficiently, but rather stays in our atmosphere to a greater extent. This additional energy heats up the world's atmosphere – we encounter global warming.[2]

To keep the Earth an inhabitable planet for future generations, we need to change the way we produce our energy as soon as possible. While energy from wind and water is already utilized with high efficiencies,[3] solar energy only encounters a niche importance. Less than 1 percent of the world's total electricity production can be attributed to photovoltaic installations (Figure 2-1).[4] It is estimated that about 3.5×10^{24} J of solar energy reach the Earth's surface every year. That is approximately 10.000 times more energy than the total annual human consumption.[5]

Figure 2-1: World Electricity production broken down to shares of fossil, nuclear and renewable energy sources.[4]

To increase the impact of solar energy, already existing photovoltaic technologies have to be improved and novel approaches and materials have to be investigated for their applicability as solar cell materials. One main focus of this research has to be put on the ease of fabrication of the cells and the use of cheap and abundant materials.

2.2 Basic Operation Principles of Photovoltaics

Solar cells consist of semiconductor materials. A semiconductor is a material that has a forbidden energy gap between the valence band (VB) and the conduction band (CB). It can become conducting when electrons in the VB are excited (by absorption of photons or by application of an external electric field) into the CB. The energy needed to excite electrons from the VB to the CB is called band-gap energy (see Figure 2-2). The remaining positive charge in

the VB can be treated as a quasi-particle and is called a hole. Both, electrons and holes, are free to diffuse through the CB and the VB of the material, respectively.[6]
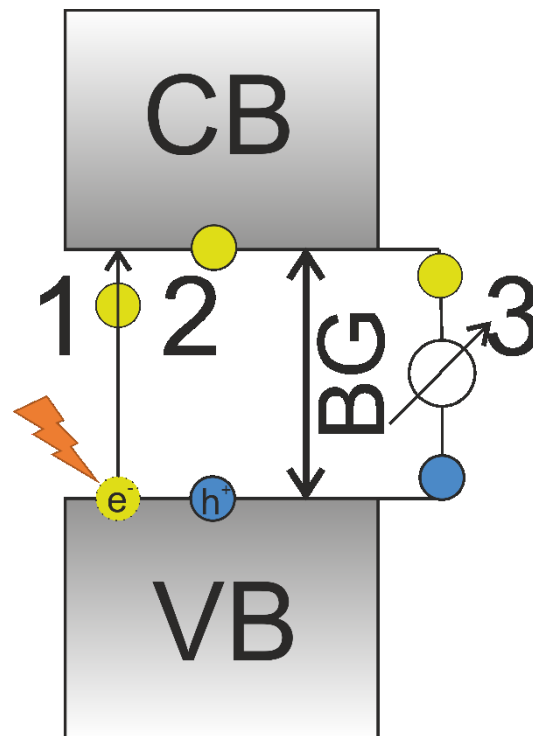
Figure 2-2: Light absorption process in a semiconductor. A photon with energy larger than the bandgap (BG) excites an electron e- from the valence band (VB) into the conduction band (CB) (1). A positively charged hole h+ remains in the valence band (2). Electrons and holes can recombine via an external circuit (3).

The magnitude of the band-gap energy has a strong influence on the light absorption properties of the material since only photons with an energy exceeding the band-gap energy can be absorbed. This also determines the maximum current that can be generated by a device employing a certain semiconductor because the solar spectrum consists of a certain number of photons for every wavelength. The more light is absorbed, the higher is the potential current.[7]

In a fully assembled solar cell carefully engineered material interfaces are used to extract the photoexcited electrons out of the device. Charge separation occurs at a junction between a material with a high electron conductivity (n-doped) and a material with a high hole conductivity (p-doped), as photogenerated charges move into their respective higer conductive

material. Upon formation of the p-n junction, electrons from the n-doped side tend to diffuse towards the positively charged p-doped side and vice-versa. These electrons and holes recombine in the center of the solar cell and create a so-called depletion region, where no mobile charges are present. Due to the diffusion of electrons out of the n-doped side, this part of the solar cell becomes positively charged, while the p-doped side, due to the loss of the holes, is charged negatively. This charge difference creates an in-built electric field that pushes electrons towards the n-doped side. At this point, there are no mobile charges left in the junction region.[2]
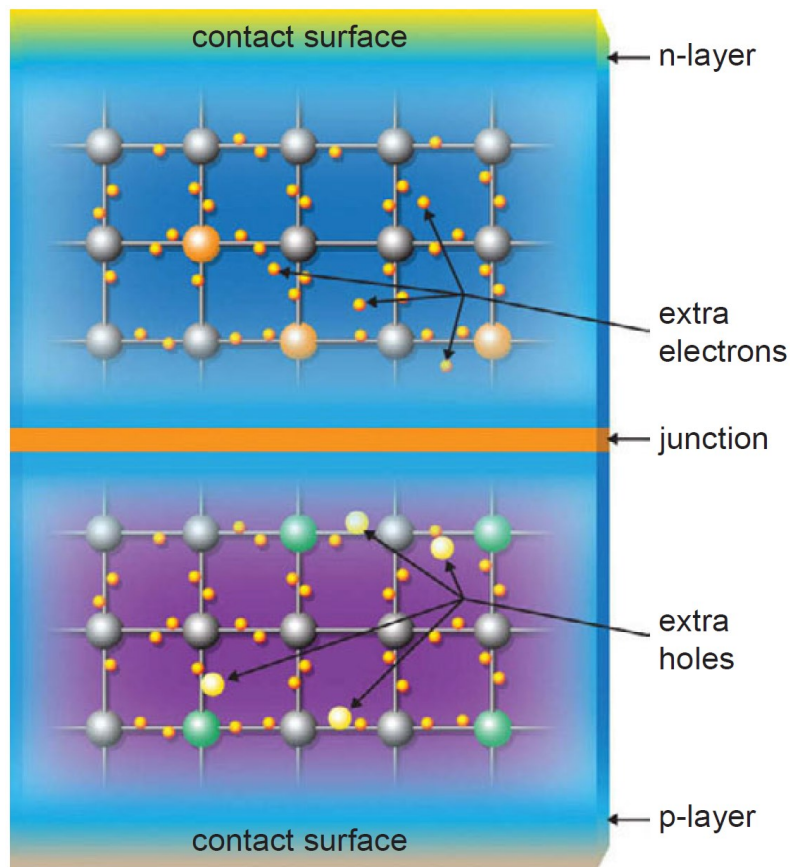
Figure 2-3: Schematic diagram of a p-n-junction of the same semiconductor with different doping levels[2]

Upon illumination photons are absorbed by this p-n-junction and electrons are excited to the CB, leaving free holes in the VB. These electrons diffuse towards the n-doped side of the solar cell and can be extracted via an external circuit. It can drive an external load, connected to this

circuit, before re-entering the solar cell on the p-doped side to recombine with a hole present there.

In the case of silicon solar cells the junction is made between p- and n-type silicon and the junction is therefore known as a homojunction. It is also possible to make a junction between p- and n-type semiconductors of different materials, for example CdS/CdTe. These are called heterojunctions. In the case of heterojunction solar cells charge separation happens due to the contact of the light absorbing material with a different material (hetero-junction), whose energy levels are carefully selected to enable the extraction of electrons from the CB. [8]

Many newly developed solar cells, like dye-sensitized, organic or perovskite solar cells, are based on a heterojunction layout. An example solar cell stack and the corresponding band-alignment for a perovskite solar cell is depicted in Figure 2-4. The active material is placed between titanium dioxide and the polymeric hole-transporter 2,2',7,7'-tetrakis-(N,N-di-4-methoxyphenylamino)-9,9'-spirobifluorene (spiro-OMeTAD).[9] In this configuration photogenerated electrons are transferred to the external circuit via the TiO_2, while holes are transported through the spiro-OMeTAD.
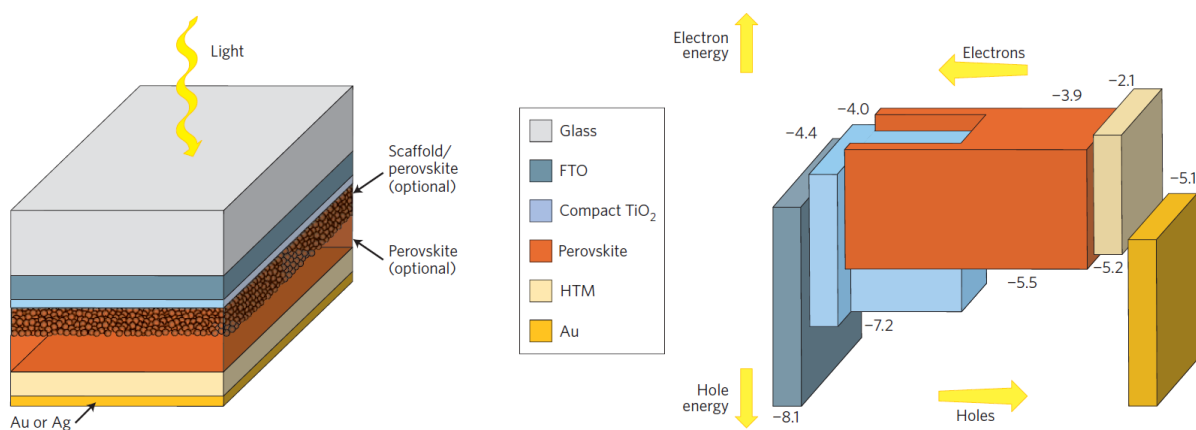
Figure 2-4: Cell layout and energy level alignment of a standard perovskite solar cell.[9]

2.3 Perovskites

The term perovskite describes in general a material with the composition ABX_3 and the same crystal structure as $CaTiO_3$. In the early 90s, researchers focused on the synthesis and characterization of a special class of organic-inorganic hybrid perovskites.[10, 11] These materials incorporate an organic cation (such as methylammonium or formamidinium, MA or FA) on the A site and a divalent metal (Pb^{2+} or Sn^{2+}) on the B site. The metal ions are octahedrally coordinated by 8 halide anions (Cl^-, Br^- or I^-), see Figure 2-5. Mitzi, Era and co-workers studied this type of materials due to their easy solution-based room temperature synthesis and their interesting optoelectronic properties.[12, 13] In particular, their suitability for the formation of thin film transistors and light emitting diodes (LEDs) was investigated.[14, 15]
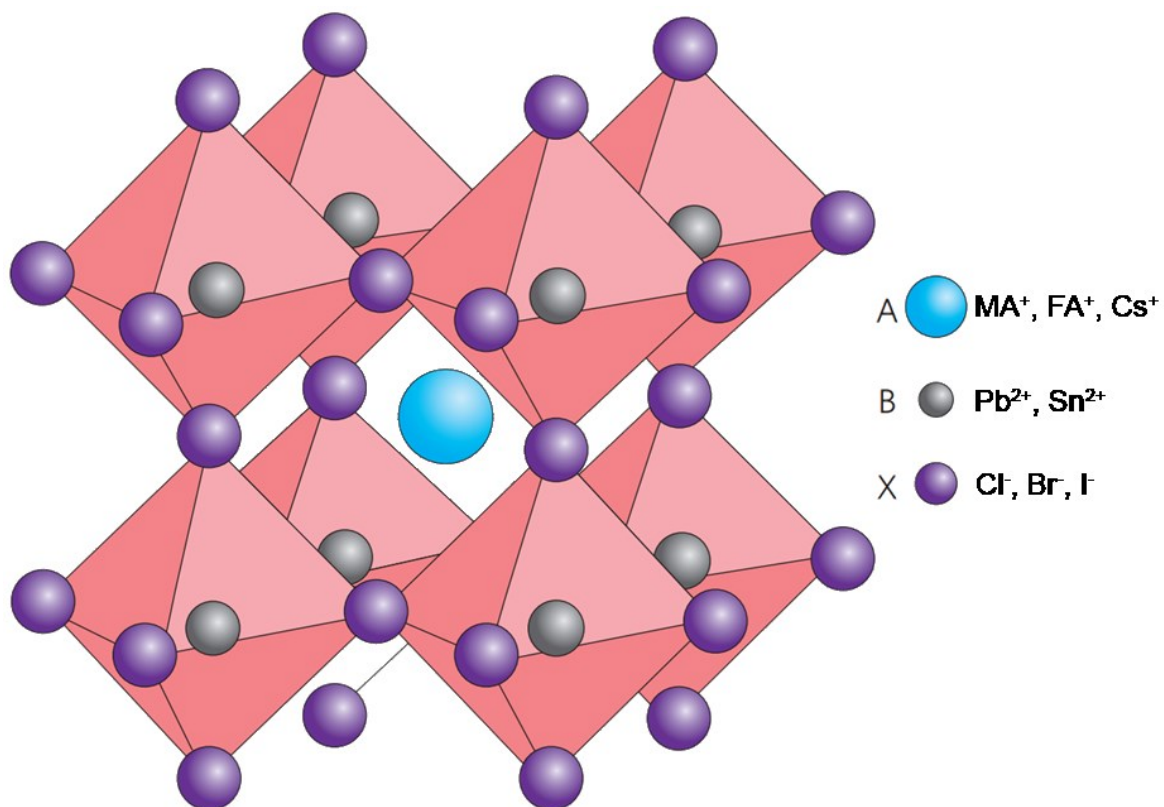
Figure 2-5: Typical ABX₃ perovskite structure with an organic cation on the A site, a heavy metal cation on the B site and halide anions on the X site.[9]

Recently, in the context of solar cell applications, other exciting properties moved into the focus of the research. Special emphasis has been placed on the high absorption coefficient,[16] the long lifetime of photogenerated species[17] and the tunability of the band-gap.[18, 19] Within only 4 years of intensive research, the efficiency of perovskite solar cells has increased from about 3 % to over 20 % in the last reports.[20, 21] The first reported solar cells were based on a conventional dye-sensitized solar cell (DSSC) layout.[20] A mesoporous titania layer was coated with perovskite particles as light absorbers and a red-ox electrolyte was used for the regeneration of the perovskite. Unfortunately, these cells suffered from chemical instability due to the used electrolyte and only survived one measurement.[22] This problem was solved soon after by employing a polymeric solid state hole-transporter, while still maintaining the mesoporous electron extraction layer.[23] This small change already lifted the efficiency of the prepared cells close to the 10 % mark.[24] The next milestone in the development of perovskite solar cells was the realisation that the perovskite itself is a good electron transport material with diffusion lengths exceeding 1 μm[17] and that the several micrometer thick mesoporous TiO_2 electrode could be reduced to only a few nanometer thin electron selective contact.[25, 26] This enabled the fabrication of thin film solar cells, without employing high-temperature sintered titania layers. Instead, layers of preformed nanoparticles or organic electron selective contacts have been used to prepare solar cells on conductive glass or even flexible substrates.[27, 28] From this point on, most of the increase in efficiency can be attributed to the optimization of the morphology of the perovskite layer.[29-31] For the fabrication of planar heterojunction solar cells, it is very important that the light absorbing material is processed as a smooth film with homogeneous thickness. It must not contain pinholes and voids, where the direct contact of electron and hole selective contact leads to increased shunting and therefore reduced device efficiency.[31] To achieve this kind of high quality perovskite films, new deposition techniques had to be developed and every aspect of the synthesis, such as the thermal annealing step,[32-35]

the addition of certain chemicals that aid the film formation,[36-44] the used solvent,[45-47] the precursor composition,[36, 39, 42, 48-50] the precursor concentration[51] and the substrate conditions had to be optimized. The synthetic strategies presented include the utilization of intermediate lead-based compounds which then slowly convert into the perovskite phase,[45, 49, 52] intercalation of organic compounds into lead-halide crystal structures,[31, 53-55] the inclusion of additives into the precursor mixture[37-39, 42-44] and solvent-induced immediate crystallization of the perovskite phase.[56-58]

2.4   Towards the Optimum Morphology of Thin Film Perovskite Solar Cells

The following part of the introduction about the morphological control and optimization of perovskite thin films will be published as a chapter in the Book 'Unconventional Thin Film Photovoltaics: Organic and Perovskite Solar Cells' as part of the RSC Energy and Environment Series.

The influence of the lead precursor

The conventional methylammonium lead iodide (MAPbI$_3$) perovskite is normally prepared by spin-coating a 1:1 molar mixture of PbI$_2$ and MAI in a suitable solvent like dimethylformamide (DMF), dimethylsulfoxide (DMSO) or γ-butyrolactone (γ-GBL) on a substrate.[59] The resulting film is then heat-treated to remove the excess solvent and induce the perovskite formation.[34] When using GBL as the solvent, the crystallization of the perovskite phase starts as soon as a critical precursor concentration is reached upon drying. For DMF and DMSO, however, an intermediate phase is formed, where layers of lead iodide (PbI$_2$) are separated by a mixture of the solvent and MAI.[45, 57] This precursor phase has a high ion mobility due to the remaining solvent. Upon further heat treatment the excess solvent is removed and the perovskite crystallizes. The morphology of the resulting perovskite film is strongly dependent on the

temperature and time of the heating step and can range from full surface coverage to sponge-like disrupted films.[34]

Halide mixtures, such as those resulting from the addition of chloride to the iodide-based perovskites, can have beneficial effects on the resulting perovskite solar cells.[31] Although the general spin-coating procedure is the same for $MAPbI_3$ and the $MAPbI_{3-x}Cl_x$ perovskite, it is necessary to use a 3:1 molar ratio of MAI to $PbCl_2$ for the mixed halide perovskite in order to achieve the correct final stoichiometry.[25] Detailed analysis of the crystallization process showed that the $MAPbI_{3-x}Cl_x$ forms an intermediate organolead mixed halide phase, which is later transformed into the pure perovskite phase through the evaporation of MACl.[60, 61] Little to no remaining chloride was found in samples derived from $PbCl_2$ and MAI.[61, 62] The chloride ions and the excess of organic compared to lead cations in the solution, slow down the crystallization rate and thus lead to the growth of large, continuous crystal domains within the film and a high degree of surface coverage (Figure 2-6 a).[62] Additionally, Williams *et al* proposed that the formation of an intermediate short-lived phase of pure $MAPbCl_3$ acts as a topotactic template for the crystallization of the $MAPbI_{3-x}Cl_x$ perovskite and therefore aids the formation of smooth films.[60]
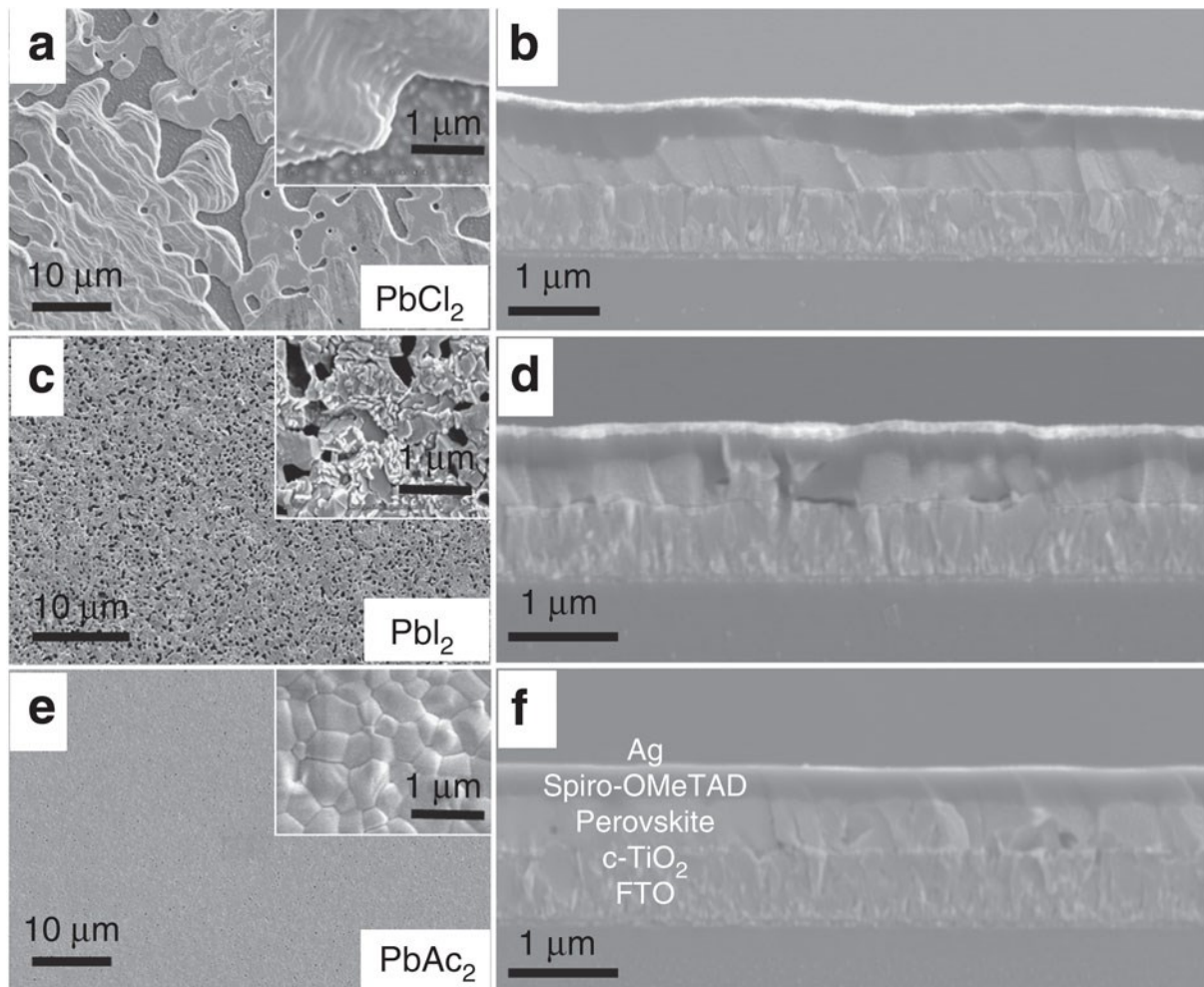
Figure 2-6: Comparative SEM micrographs in top and cross-section view using PbCl₂ (a,b) PbI₂ (c,d) or Pb(OAc)₂ (e,f) as lead source. Figure 1-6 is reproduced from Ref. [49] with permission from the Nature Publishing Group.

Even more homogeneous and smoother layers of MAPbI$_3$ perovskite have been achieved when starting from lead acetate (Pb(OAc)$_2$) as the precursor salt (Figure 2-6e).[49, 63] All three processing routes result in the formation of MAPbI$_3$ with only very little impurities. The films processed from PbI$_2$ and PbCl$_2$ were non-continuous with large gaps in between perovskite clusters and with inhomogeneous film thickness (Figure 2-6 a,b,c,d). However, films prepared from Pb(OAc)$_2$ achieve nearly 100 % surface coverage, are very smooth and highly consistent in thickness over the whole substrate (Figure 2-6 e,f).

Table 1: Summary of the performance and morphology quality of the assembled films starting from different lead sources.[49]

Lead precursor	reported PCE_{max}	Grain size (approx)	Surface coverage	RMS roughness
PbI_2	9.3	100 – 500 nm	90 %	52.2 nm
$PbCl_2$	12.0	10-50 μm	90 %	62.4 nm
$Pb(OAc)_2$	14.0	0.5 – 1 μm	100 %	12.3 nm

The smoothness and high surface coverage of the resulting films is attributed to the rapid crystallization of perovskite crystals with a high nucleation rate. $MA(OAc)_2$ evaporates at temperatures much lower than the sublimation temperature of MACl and MAI. While these two compounds evaporate at temperatures of 226 °C and 245 °C, respectively, $MA(OAc)_2$ only needs a temperature of 97 °C to sublime.[49] With this in mind, it is clear that the use of an acetate based lead precursor has a strong influence on the evaporation and therefore the crystallization dynamics, resulting in the observed strong differences in morphology for the different preparation routes. The obtained efficiencies for optimized solar cells for each lead precursor follow the same trend as the morphology and surface coverage of the thin films. For solar cells prepared with comparable architectures, i.e. employing undoped TiO_2 and spiro-OMeTAD as the charge extraction layers, the lead acetate route gave the highest efficiency, followed by $PbCl_2$ and PbI_2 in this order (see Table 1).

Additive-controlled crystallization

A different approach to ensure the formation of homogeneous films is the use of additives in the spin-coating solution, which affect the crystallization and formation of the perovskite layer. The primarily used additives are ammonium or phosphonium halides,[39, 40, 44] dihalide alkanes[37, 43] or protic acids.[38, 41]

2.4. Towards the Optimum Morphology of Thin Film Perovskite Solar Cells

When incorporating small amounts of ammonium chloride (NH_4Cl) or methylammonium chloride (MACl) into the spin-coating solution for the $MAPbI_3$ perovskite, the film homogeneity is greatly improved (Figure 2-7 a and b). A similar effect has been reported for the phosphonium halides tetraphenylphosphonium iodide and chloride (TPPI and TPPCl).[39] Since the TPP^+ cation is stable on its own, there is an excess of iodide and chloride anions in the solution. These free ions speed up the growth kinetics, leading to a larger number of crystal nuclei,[39] smoother films and therefore more efficient solar cells (Figure 2-7 c and d).

The addition of dihalide alkanes, like 1,8-diiodooctane (DIO) or the smaller 1,4-diiodobutane (DIB) have a similar profound effect on the morphology of the prepared perovskite thin films.[37, 43] Not only do these additives increase the solubility of the lead precursors in DMF,[43] but they also slow down the crystallization rate of the perovskite during the thermal annealing, which leads to a film consisting of fewer, but larger crystals. These effects are attributed to a chelation of the Pb^{2+} ions in the solution by the DIO or DIB.[37, 43] Before the perovskite can form crystals, the chelating agents have to be thermally removed. Since this process is much slower than the actual crystallization, homogenous planar films with large crystals are formed (Figure 2-7 e and f).
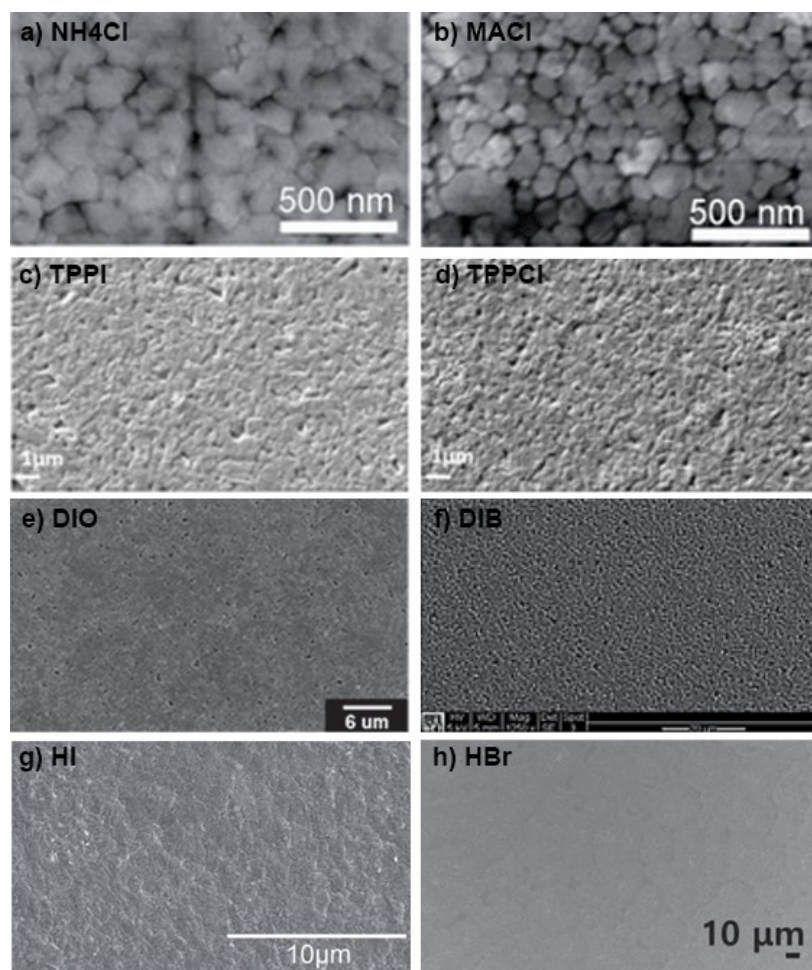
Figure 2-7: Perovskite film morphologies obtained using various additives a) ammonium chloride (NH₄Cl), b) methylammonium chloride (MACl), c) tetraphenylphosphonium iodide (TPPI), d) tetraphenylphosphonium chloride (TPPCl), e) diiodooctane (DIO), f) diiodobutane (DIB), g) hydriodic acid (HI) and h) hydrobromic acid (HBr). Figures 1-7 a, b, f and g are reproduced from Ref. [37, 41, 44] with permission from The Royal Society of Chemistry. Figure 1-7 c, d, e and h are reproduced from Ref [38, 39, 43] with permission from John Wiley and Sons.

A comparable slow-down of the crystallization rate can be achieved by adding solvents to the reaction mixture that enhance the solubility of the precursor. This approach has been demonstrated for the formation of FAPbI₃ and MAPbBr₃. The solvents used were HI for FAPbI₃ and HBr for MAPbBr₃.[38, 41] In each of these cases, the addition of only 10 % of the second solvent was enough to increase the concentration of the precursors in the solution to a level where, upon drying, a highly super-saturated solution is formed. Further heating of this solution leads to the rapid formation of many crystal nuclei. This in turn leads to a homogeneous crystallite size distribution and therefore homogeneous thin films ((Figure 2-7 g and h).).[38, 41]

2.4. Towards the Optimum Morphology of Thin Film Perovskite Solar Cells

Table 2: Influence of different additives on the morphological quality of perovskite thin films and the efficiency of resulting solar cells.

Additive	perovskite	reported PCE$_{max}$	Grain size (approx)	Surface coverage
NH$_4$Cl[40, 44]	MAPbI$_3$	9.93	250 nm	~99%
TPPI/TPPCl[39]	MAPbI$_3$	11.7	< 1μm	~99%
DIO[43]	MAPbI$_3$	11.8	1 μm	95%
DIB[37]	MAPbI$_3$	13.1		95%
HI[41]	FAPbI$_3$	14.2	1 μm	100 %
HBr[38]	MAPbBr$_3$	10.4		100 %

In general, the addition of easily removable species, like ammonium or phosphonium halides, speeds up the crystallization reaction and leads to films with a high number of crystal nuclei followed by the growth of smaller crystals (100 to 500 nm), which form a polycrystalline dense layer. With the addition of less volatile species, like the dihalide alkanes or aqueous acids, however, the reaction is slowed down, leading to the formation of fewer crystal nuclei which can grow to sizes above 1 μm. The crystallite sizes and the approximate surface coverage for the different additives are summarized in Table 2. When looking at the performance of the resulting solar cells, it appears to be correlated with the size of the crystalline domains, where larger crystals result in more efficient solar cells.

Solvent-induced crystallization

Solvent-induced crystallization is generally based on the deposition of an initial wet film of the perovskite precursor mixture on a substrate. This is followed by the quick addition of or the immersion into a second solvent where the precursors are insoluble to force a rapid crystallization of the perovskite layer.
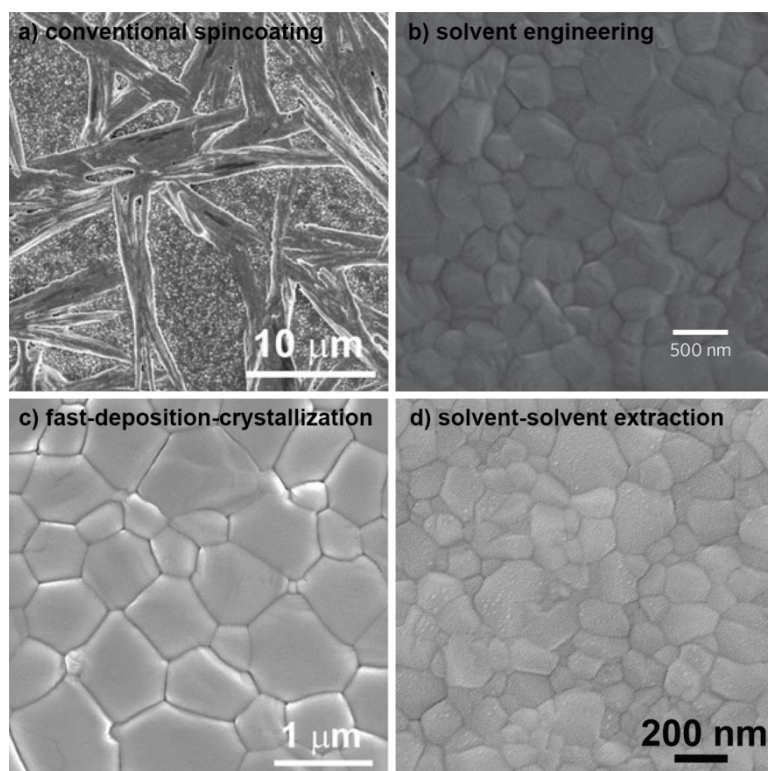
Figure 2-8: SEM micrographs of perovskite thin films obtained via the a) conventional spin-coating, b) solvent engineering, c) fast deposition-crystallization and d) solvent-solvent extraction approach. Figure 1-8 a and c are reproduced from Ref. [56] with permission from John Wiley and Sons. Figure 1-8 b is reproduced from Ref. [57] with permission from the Nature Publishing Group. Figure 1-8 d is reproduced from Ref. [58] with permission from The Royal Society of Chemistry.

For the solvent engineering approach, Seok et al dissolved the perovskite precursors in a mixture of GBL and DMSO and spincoated them on a 200 nm thick mesoporous TiO_2 layer.[57] In a subsequent spin-coating step, the still wet film was treated with a toluene drop to force the precursors to precipitate out of the GBL/DMSO solution and to crystallize in the PbI_2/MAI/DMSO intermediate phase described in the previous section. After heating for 10 minutes at 100 °C, the DMSO was removed and an extremely smooth film was obtained with crystallite sizes of a few 100 nm (Figure 2-8 b).

A similar approach for the preparation of extremely smooth $MAPbI_3$ layers has been reported by Spiccia and co-workers.[56] 4-5 seconds after the precursor film has been deposited from DMF, rapid crystallization of the perovskite phase is induced by dropping chlorobenzene (CBZ) on the still spinning film. By adding CBZ, the solubility of the precursors in the DMF phase is

strongly decreased. This can be contrasted to the standard spin-coating procedure, where the crystallization is slowly induced by evaporation of the solvent and the crystals grow in a less defined manner during a longer time period (Figure 2-8 a). The high number of simultaneously created nuclei and the rapid crystal growth in the fast deposition conversion (FDC) procedure results in an extremely smooth film with micrometer sized grains (Figure 2-8 c).

Another "anti-solvent" approach has been reported by Zhou et al.[58] In this case, the precursors are dissolved in a high boiling solvent (T_B = 200 °C). The high boiling temperature of the solvent ensures that the film still contains some residual solvent after the spin-coating process. The still wet film is then immersed in a bath of diethylether (DEE) at room temperature, in which neither the precursors nor the perovskite is soluble. The ether extracts the NMP out of the wet film, leading to an abrupt supersaturation of the liquid film and the formation of a high number of perovskite nuclei. This process is called solvent-solvent extraction (SSE) and can be used to prepare extremely smooth perovskite thin films with grain sizes of about 100 nm (Figure 2-8 d).

All of these procedures enable the formation of films with very high surface coverage and comparably large crystal grains (see Table 3). Solar cells fabricated with these methods all exhibit high efficiencies above 13%.

Table 3: Film quality parameters and solar cell efficiencies for perovskite films prepared via different solvent-induced crystallization approaches.

Process	Solvent/antisolvent	reported PCE_{max}	Grain size (approx)	Surface coverage
Solvent engineering[57]	GBL+DMSO/toluene	16.7	500 nm	100 %
Fast deposition conversion[56]	DMF/chlorobenzene	13.9	0.5 - 1 μm	100 %
Solvent/solvent extraction[58]	NMP/Ether	15.2	100 – 500 nm	100 %

Perovskite conversion via cation infiltration

The two-step deposition approach is an alternative solution processing route for the preparation of perovskite thin films first reported by Liang et al. in the late 90s, later expanded by Burschka et al. for mesoporous substrates and finally introduced by Liu et al. in planar heterojunction solar cells.[53, 54, 64] It consists of two main steps (Figure 2-9 a). Firstly, a layer of the lead precursor is deposited on the substrate via spin-coating from DMF or a comparable solvent. To obtain a smooth precursor film, it can be necessary to preheat the solution and the substrate to induce rapid crystallization of the lead precursor.[65] After obtaining a smooth lead precursor film, it is immersed in a solution of the ammonium halide salt (MAI, MACl, FAI, etc) in isopropanol (IPA). The lead precursor is insoluble in IPA, but the organic and halide ions can diffuse from the immersion bath through the lead precursor layer and induce the crystallization of the perovskite phase.[64] Since the diffusion speed of the ions and the crystallization rate of the perovskite depend on the temperature and on the concentration of the solution, fine-tuning of these parameters is necessary to obtain full surface coverage and complete conversion.[66]

2.4. Towards the Optimum Morphology of Thin Film Perovskite Solar Cells
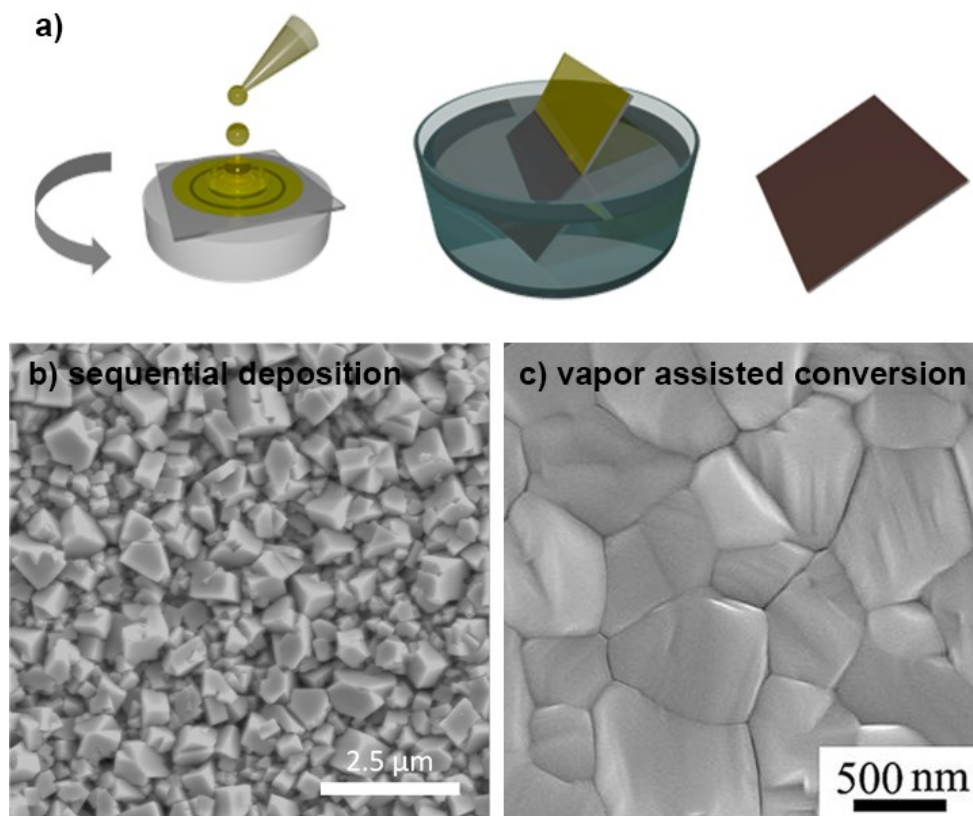
Figure 2-9: General procedure for the sequential deposition of perovskite thin films (a) and SEM micrographs of films obtained for sequential deposition (b) and vapor assisted conversion (c). Figure 1-9 b is reproduced from Ref. [65] with permission from John Wiley and Sons. Figure 1-9 c isreprinted with permission from Ref. [55]. Copyright (2014) American Chemical Society.

Recent studies performed with 2-D X-ray scattering methods revealed more insights into the actual crystallization process of the MAPbI$_3$ perovskite (Figure 2-10).[67] Starting from a film of PbI$_2$, which consists of crystalline sheets on top of each other, the MAI diffuses in between these sheets and starts the crystallization. As the PbI$_2$ layers expand upon inclusion of the MAI, growth is constrained in the lateral direction. This leads to a predominant growth direction perpendicular to the substrate. The crystallites closer to the substrate experience a stronger confinement and start to crack, leaving smaller grains of perovskite, while the crystals closer to the surface can expand in a unrestricted way and form large cuboid crystals.[67]
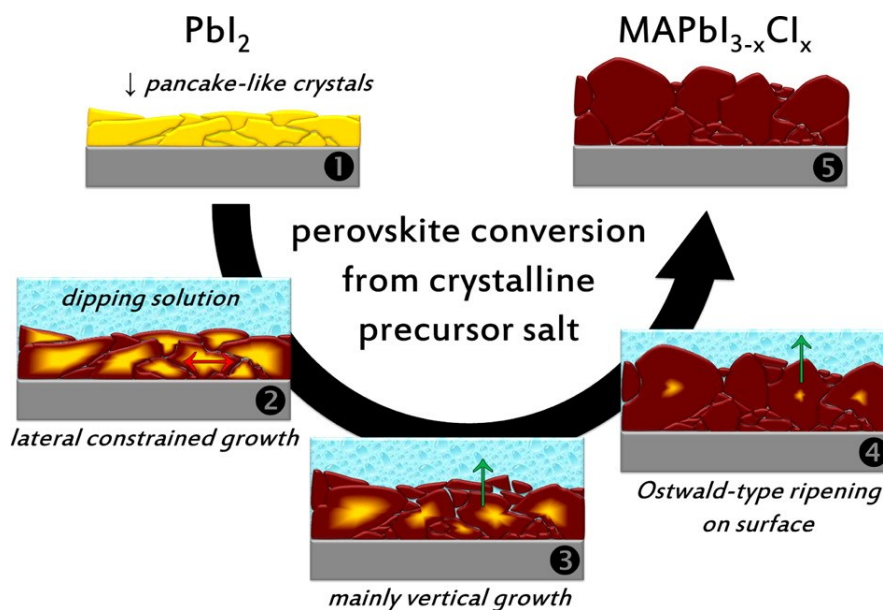
Figure 2-10: Schematic representation of the crystallization procedure of perovskite films prepared via sequential deposition. Reprinted with permission from Ref.[67]. Copyright (2015) American Chemical Society.

Similarly to the 1-step protocols, the addition of small amounts of MACl to the MAI immersion solution (up to 5%) improve the solar cell performance.[65] These films consist of $MAPbI_3$ cuboids, which cover nearly 100% of the surface (Figure 2-9 b). Additionally, the rough surface created by the randomly oriented cuboids can act as a light trap and therefore enhance the light absorbed in the active layer without modifying its thickness.[68]

The vapor-assisted solution process (VASP) works in a way similar to the sequential deposition. Instead of an MAI solution, the PbI_2 layer is exposed to a vapor of the ammonium halide salt.[55] As the MAI evaporates, it diffuses into the PbI_2 layer and starts forming the perovskite phase. As there is equilibrium with the MAI atmosphere surrounding the PbI_2 film and the formed perovskite phase, the crystallization takes place very slowly, forming large crystal plates (Figure 2-9 c). The resulting films are much smoother than those obtained by the solution induced crystallization, with crystallites reaching through the whole thickness of the film.[55]

The crystal size, surface coverage and the obtained efficiencies for the different 2-step approaches are shown in Table 4.

2.4. Towards the Optimum Morphology of Thin Film Perovskite Solar Cells

Table 4: Film quality parameters and solar cell efficiencies for perovskite films prepared via sequential deposition or vapor assisted conversion

Synthesis procedure	Reported PCE$_{max}$	Grain size (approx)	Surface coverage
MAI[53]	15.7	0.1 – 1 μm	100%
MAI+ MACl[31]	14.8	100 – 600 nm	100%
Vapor assisted conversion[55]	12.1	> 1 μm	100%

The perovskite films described above generally follow the trend where the larger the crystal, the higher the resulting performance of the solar cell, as long as the surface area coverage approaches 100%. This result is rather intuitive, as larger grains are expected to result in fewer grain boundaries, and thus, fewer trap states and recombination centers.[69] A more direct look into these phenomena can be seen in the work of Xiao et al.. Here, the introduction of an additional solvent annealing (SA) step after perovskite deposition led to micrometer sized perovskite grains spanning the whole thickness of the sample.[70, 71] This resulted in a significant performance increase over thermally annealed (TA) films from 8.2 % to 14.8%, as shown on in Figure 2-11c. The superior photovoltaic suitability of SA vs. TA annealed samples is also indicated by a longer open circuit voltage decay, which implies slower charge recombination rates (Figure 2-11d). The concept was recently extended by Nie et al. to achieve millimeter-sized grains.[69] Here, the precursor solution was spin-coated on a hot substrate. The presence of excess high-boiling point solvent combined with the high temperature above the super-saturation point prolongs the growth period of the perovskite crystals.
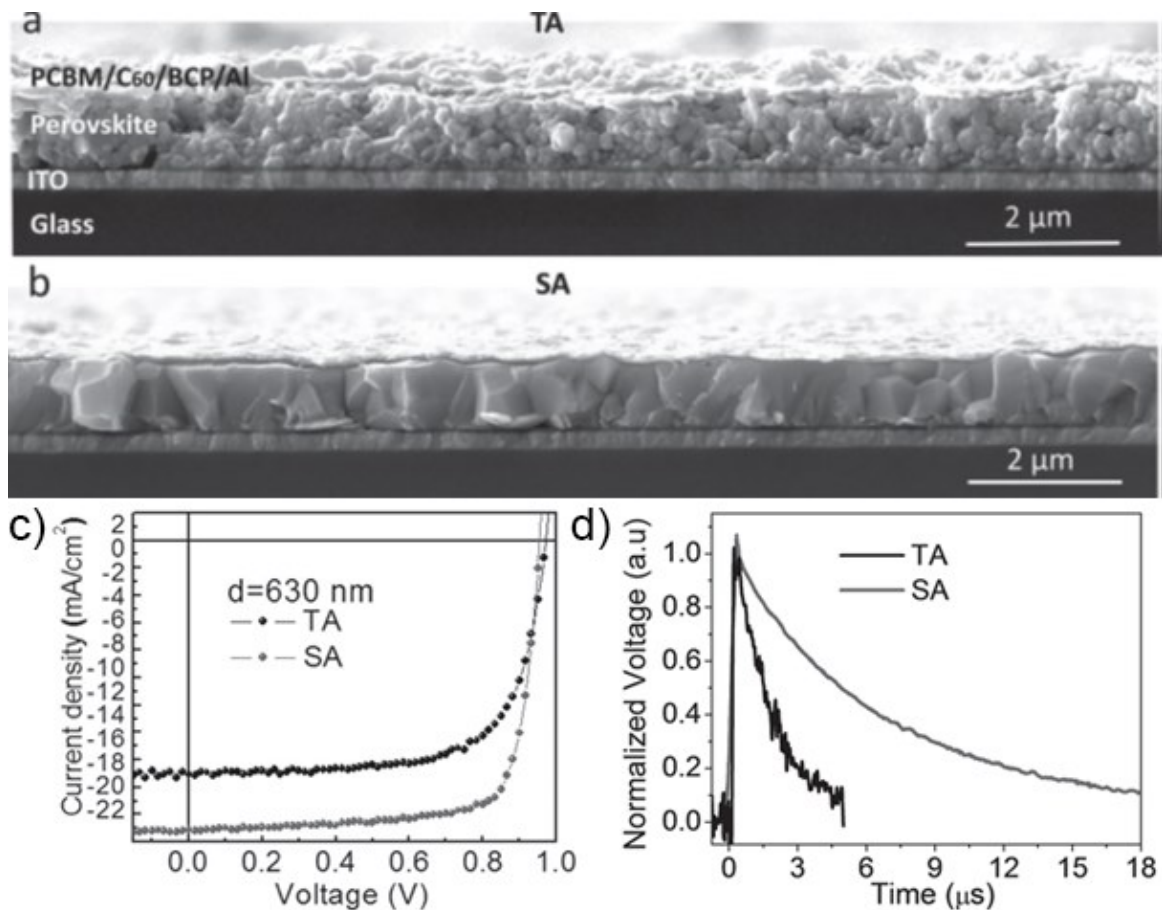
Figure 2-11: Morphology of perovskite layers prepared by thermal annealing (TA, a) and solvent annealing (SA, b). The influence of the crystallite size can be seen in the JV measurements (c) and the open circuit voltage decay (d). Figure 1-11 is adapted from Ref. [70] with permission from John Wiley and Sons.

Not only the grain size but also the grain orientation has an influence on the device performance.

For instance, Docampo et al. have shown for perovskite converted samples that with a higher

orientation of the 110 plane perpendicular to the substrate, higher short circuit currents on

average can be achieved.[66] A similar effect was observed by Saliba et al., where flash-annealed

samples were compared with those obtained by slow annealing, both in devices and with

grazing incidence wide angle scattering (GIWAXS).[34] They observed that for the fast and hot

annealing step highly uniform micron sized crystallites were obtained with a higher degree of

orientation in the 2D-Xray scattering experiments, which also resulted in higher short circuit

currents. These experimental results have been recently substantiated by theoretical studies that

point towards anisotropy in terms of charge transfer for different perovskite surfaces.[72]

Overall, films exhibiting a preferential orientation of the 002 plane parallel to the substrate are expected to exhibit optimum performance.

2.5 Band-Gap Tuning

One remarkable property of organic-inorganic perovskites is that the halides in the structure can be mixed in wide concentration ranges. This has first been demonstrated for mixtures of iodide and bromide[18, 73] and later also for bromide/chloride systems.[74] In both cases the band-gap energy increases with addition of the smaller halide. Figure 2-12 shows a photograph of a series of $MAPbI_{3-x}Br_x$ perovskites ranging from 100 % iodide content (top left) to 100 % bromide (bottom right).

Figure 2-12: Photograph of a series of $MAPbI_{3-x}Br_x$ perovskites ranging from 100 % iodide content (top left) to 100 % bromide (bottom right). The change in band-gap energy can be observed as color change.

It has been shown with X-ray analysis and photothermal deflection spectroscopy (PDS) that the materials formed are phase-pure and do not consist of mixtures of the pure halide perovskites. [19]

2.6 Other Applications for Perovskites

Recently, the application of perovskites as light emitters has been rediscovered, after substantial earlier research activities in the 1990s.[12] While the focus back then was put on 2-dimensional layered perovskites, today the same 3-dimensionally connected perovskite materials that are used for solar cell applications also are also investigated in the context of light emission.[66, 74] One of the main reasons for this interest is the band-gap tunability of the perovskite materials.[18, 41] It has been demonstrated that by substituting the iodide in the $MAPbI_3$ with bromide, the color of the resulting LED changes from red to green (Figure 2-13).[75] By mixing chloride into the $MAPbBr_3$ perovskite, it is even possible to widen the bandgap to a level where blue electroluminescence is visible.[74]
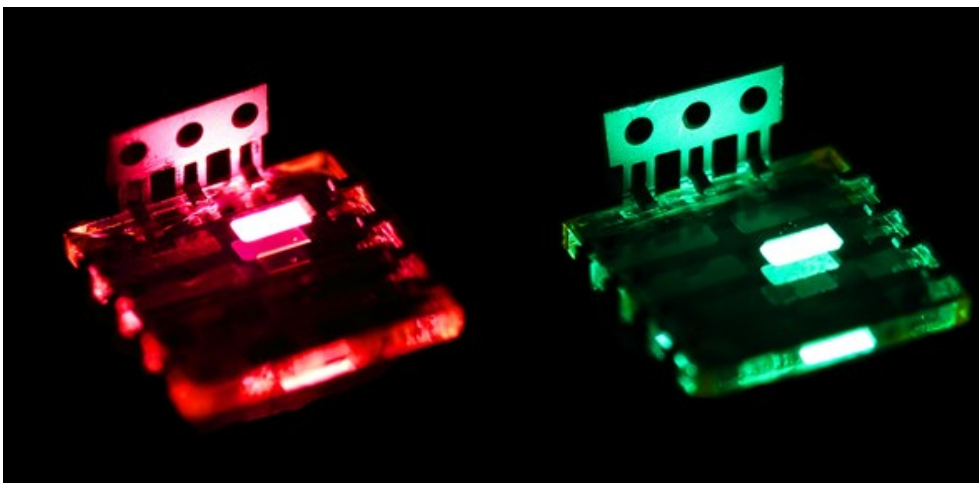
Figure 2-13: Red and green light emission from $MAPbI_3$ and $MAPBBr_3$, respectively.[75]

2.6. Other Applications for Perovskites

Another approach to achieve blue emission has recently been published and is based on the quantum confinement effect, where the bandgap energy of a material becomes larger with reducing particle size.[4]

Due to the strong and efficient photoluminescence of the perovskite materials, it was possible to induce lasing under high optical pump fluences. This was first demonstrated for MAPbI$_3$,[76] and was later extended to iodide/bromide and bromide/chloride mixtures, enabling the fine-tuning of the emission wavelength over the whole visible spectrum.[5, 77]
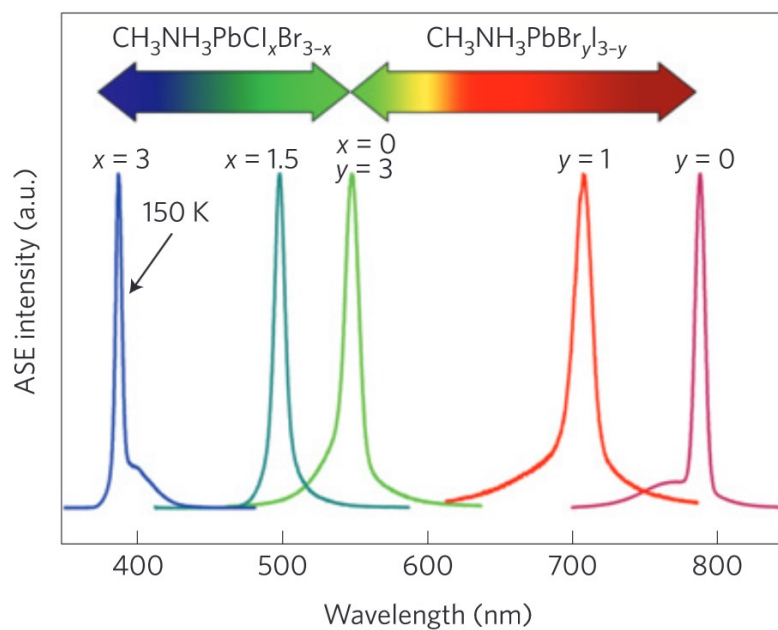
Figure 2-14: Compositional tuning of the emission wavelength of mixed halide perovskites based on MAPbI$_{3-x}$Br$_x$ and MAPbBr$_{3-x}$Cl$_x$.[5]

2.7 Literature

[1]   V. Scott, R. S. Haszeldine, S. F. B. Tett, A. Oschlies, *Nature Clim. Change* **2015**, *5*, 419.

[2]   *Fundamentals of Materials for Energy and Environmental Sustainability*, Cambridge University Press, Cambridge, UK **2011**.

[3]   P. Denholm, G. L. Kulcinski, T. Holloway, *Environ. Sci. Technol.* **2005**, *39*, 1903.

[4]   D. Di, K. P. Musselman, G. Li, A. Sadhanala, Y. Ievskaya, Q. Song, Z.-K. Tan, M. L. Lai, J. L. MacManus-Driscoll, N. C. Greenham, R. H. Friend, *J. Phys. Chem. Lett.* **2015**, *6*, 446.

[5]   G. Xing, N. Mathews, S. S. Lim, N. Yantara, X. Liu, D. Sabba, M. Grätzel, S. Mhaisalkar, T. C. Sum, *Nat. Mater.* **2014**, *13*, 476.

[6]   P. Würfel, *Physics of Solar Cells: From Basic Principles to Advanced Concepts*, Wiley-VCH, Weinheim **2009**.

[7]   H. J. Snaith, *Adv. Funct. Mater.* **2010**, *20*, 13.

[8]   M. C. Scharber, D. Mühlbacher, M. Koppe, P. Denk, C. Waldauf, A. J. Heeger, C. J. Brabec, *Adv. Mater.* **2006**, *18*, 789.

[9]   M. A. Green, A. Ho-Baillie, H. J. Snaith, *Nat. Photon.* **2014**, *8*, 506.

[10]   D. B. Mitzi, C. A. Feild, Z. Schlesinger, R. B. Laibowitz, *J. Solid State Chem.* **1995**, *114*, 159.

[11]   K. Liang, D. B. Mitzi, M. T. Prikas, *Chemistry of materials* **1998**, *10*, 403.

[12]   T. Hattori, T. Taira, M. Era, T. Tsutsui, S. Saito, *Chem. Phys. Lett.* **1996**, *254*, 103.

[13]   C.-q. Xu, H. Sakakura, T. Kondo, S. Takeyama, N. Miura, Y. Takahashi, K. Kumata, R. Ito, *Solid State Commun.* **1991**, *79*, 249.

[14]   K. Chondroudis, D. B. Mitzi, *Chem. Mater.* **1999**, *11*, 3028.

[15]   M. Era, S. Morimoto, T. Tsutsui, S. Saito, *Synth. Met.* **1995**, *71*, 2013.

[16]   S. De Wolf, J. Holovsky, S.-J. Moon, P. Löper, B. Niesen, M. Ledinsky, F.-J. Haug, J.-H. Yum, C. Ballif, *J. Phys. Chem. Lett.* **2014**, *5*, 1035.

[17]   S. D. Stranks, G. E. Eperon, G. Grancini, C. Menelaou, M. J. P. Alcocer, T. Leijtens, L. M. Herz, A. Petrozza, H. J. Snaith, *Science* **2013**, *342*, 341.

[18]   J. H. Noh, S. H. Im, J. H. Heo, T. N. Mandal, S. I. Seok, *Nano Lett.* **2013**, *13*, 1764.

[19]   A. Sadhanala, F. Deschler, T. H. Thomas, S. E. Dutton, K. C. Goedel, F. C. Hanusch, M. L. Lai, U. Steiner, T. Bein, P. Docampo, D. Cahen, R. H. Friend, *J. Phys. Chem. Lett.* **2014**, *5*, 2501.

[20]   A. Kojima, K. Teshima, Y. Shirai, T. Miyasaka, *J. Am. Chem. Soc.* **2009**, *131*, 6050.

[21]   W. S. Yang, J. H. Noh, N. J. Jeon, Y. C. Kim, S. Ryu, J. Seo, S. I. Seok, *Science* **2015**, *348*, 1234.

[22]   J. H. Im, C. R. Lee, J. W. Lee, S. W. Park, N. G. Park, *Nanoscale* **2011**, *3*, 4088.

[23]   L. Etgar, P. Gao, Z. S. Xue, Q. Peng, A. K. Chandiran, B. Liu, M. K. Nazeeruddin, M. Gratzel, *J. Am. Chem. Soc.* **2012**, *134*, 17396.

[24]   H. S. Kim, C. R. Lee, J. H. Im, K. B. Lee, T. Moehl, A. Marchioro, S. J. Moon, R. Humphry-Baker, J. H. Yum, J. E. Moser, M. Gratzel, N. G. Park, *Sci. Rep.* **2012**, *2*, 591.

[25]   M. M. Lee, J. Teuscher, T. Miyasaka, T. N. Murakami, H. J. Snaith, *Science* **2012**, *338*, 643.

[26]   J. M. Ball, M. M. Lee, A. Hey, H. J. Snaith, *Energy Environ. Sci.* **2013**, *6*, 1739.

[27]   D. Liu, T. L. Kelly, *Nat. Photon.* **2013**, *advance online publication*.

[28]   P. Docampo, J. M. Ball, M. Darwich, G. E. Eperon, H. J. Snaith, *Nat. Commun.* **2013**, *4*, 2761.

[29]   V. M. Burlakov, G. E. Eperon, H. J. Snaith, S. J. Chapman, A. Goriely, *Appl. Phys. Lett.* **2014**, *104*, 091602.

[30]   G. Li, K. L. Ching, J. Y. L. Ho, M. Wong, H.-S. Kwok, *Adv. Energy Mater.* **2015**, n/a.

[31]   G. E. Eperon, V. M. Burlakov, P. Docampo, A. Goriely, H. J. Snaith, *Adv. Funct. Mater.* **2014**, *24*, 151.

[32]   H.-L. Hsu, C.-P. Chen, J.-Y. Chang, Y.-Y. Yu, Y.-K. Shen, *Nanoscale* **2014**, *6*, 10281.

[33]   J. Troughton, C. Charbonneau, M. J. Carnie, M. L. Davies, D. A. Worsley, T. M. Watson, *J. Mater. Chem. A* **2015**, *3*, 9123.

[34]   M. Saliba, K. W. Tan, H. Sai, D. T. Moore, T. Scott, W. Zhang, L. A. Estroff, U. Wiesner, H. J. Snaith, *J. Phys. Chem. C* **2014**, *118*, 17171.

[35]   A. Dualeh, N. Tétreault, T. Moehl, P. Gao, M. K. Nazeeruddin, M. Grätzel, *Adv. Funct. Mater.* **2014**, *24*, 3250.

[36]   C.-Y. Chang, C.-Y. Chu, Y.-C. Huang, C.-W. Huang, S.-Y. Chang, C.-A. Chen, C.-Y. Chao, W.-F. Su, *ACS Appl. Mater. Interfaces* **2015**, *7*, 4955.

[37]   C.-C. Chueh, C.-Y. Liao, F. Zuo, S. T. Williams, P.-W. Liang, A. K. Y. Jen, *J. Mater. Chem. A* **2015**, *3*, 9058.

[38]   J. H. Heo, D. H. Song, S. H. Im, *Adv. Mater.* **2014**, *26*, 8179.

[39]   C. Sun, Q. Xue, Z. Hu, Z. Chen, F. Huang, H.-L. Yip, Y. Cao, *Small* **2015**.

[40]   Y. Chen, Y. Zhao, Z. Liang, *Chem. Mater.* **2015**, *27*, 1448.

[41]   G. E. Eperon, S. D. Stranks, C. Menelaou, M. B. Johnston, L. M. Herz, H. J. Snaith, *Energy Environ. Sci.* **2014**, *7*, 982.

[42]   X. Song, W. Wang, P. Sun, W. Ma, Z.-K. Chen, *Appl. Phys. Lett.* **2015**, *106*, 033901.

[43]   P.-W. Liang, C.-Y. Liao, C.-C. Chueh, F. Zuo, S. T. Williams, X.-K. Xin, J. Lin, A. K. Y. Jen, *Adv. Mater.* **2014**, *26*, 3748.

[44]   C. Zuo, L. Ding, *Nanoscale* **2014**, *6*, 9935.

[45]   D. Shen, X. Yu, X. Cai, M. Peng, Y. Ma, X. Su, L. Xiao, D. Zou, *J. Mater. Chem. A* **2014**, *2*, 20454.

[46]   H.-B. Kim, H. Choi, J. Jeong, S. Kim, B. Walker, S. Song, J. Y. Kim, *Nanoscale* **2014**, *6*, 6679.

[47]   S. Paek, N. Cho, H. Choi, H. Jeong, J. S. Lim, J.-Y. Hwang, J. K. Lee, J. Ko, *J. Phys. Chem. C* **2014**, *118*, 25899.

[48]   S. Pang, H. Hu, J. Zhang, S. Lv, Y. Yu, F. Wei, T. Qin, H. Xu, Z. Liu, G. Cui, *Chem. Mater.* **2014**, *26*, 1485.

[49]   W. Zhang, M. Saliba, D. T. Moore, S. K. Pathak, M. T. Hörantner, T. Stergiopoulos, S. D. Stranks, G. E. Eperon, J. A. Alexander-Webber, A. Abate, A. Sadhanala, S. Yao, Y. Chen, R. H. Friend, L. A. Estroff, U. Wiesner, H. J. Snaith, *Nat. Commun.* **2015**, *6*, 6142.

[50]   F. Wang, H. Yu, H. Xu, N. Zhao, *Adv. Funct. Mater.* **2015**, *25*, 1120.

[51]   T. Leijtens, B. Lauber, G. E. Eperon, S. D. Stranks, H. J. Snaith, *J. Phys. Chem. Lett.* **2014**, *5*, 1096.

[52]   Y. Wu, A. Islam, X. Yang, C. Qin, J. Liu, K. Zhang, W. Peng, L. Han, *Energy Environ. Sci.* **2014**, *7*, 2934.

[53]   D. Liu, T. L. Kelly, *Nat. Photon.* **2014**, *8*, 133.

[54]   J. Burschka, N. Pellet, S.-J. Moon, R. Humphry-Baker, P. Gao, M. K. Nazeeruddin, M. Gratzel, *Nature* **2013**, *499*, 316.

[55]   Q. Chen, H. Zhou, Z. Hong, S. Luo, H.-S. Duan, H.-H. Wang, Y. Liu, G. Li, Y. Yang, *J. Am. Chem. Soc.* **2014**, *136*, 622.

[56]   M. Xiao, F. Huang, W. Huang, Y. Dkhissi, Y. Zhu, J. Etheridge, A. Gray-Weale, U. Bach, Y.-B. Cheng, L. Spiccia, *Angew. Chem.* **2014**, *53*, 9898.

[57]   N. J. Jeon, J. H. Noh, Y. C. Kim, W. S. Yang, S. Ryu, S. I. Seok, *Nat. Mater.* **2014**, *13*, 897.

[58]   Y. Zhou, M. Yang, W. Wu, A. L. Vasiliev, K. Zhu, N. P. Padture, *J. Mater. Chem. A* **2015**, *3*, 8178.

[59] H. S. Kim, C. R. Lee, J. H. Im, K. B. Lee, T. Moehl, A. Marchioro, S. J. Moon, R. Humphry-Baker, J. H. Yum, J. E. Moser, M. Gratzel, N. G. Park, *Scientific Reports* **2012**, *2*.

[60] S. T. Williams, F. Zuo, C.-C. Chueh, C.-Y. Liao, P.-W. Liang, A. K. Y. Jen, *ACS Nano* **2014**, *8*, 10640.

[61] E. L. Unger, A. R. Bowring, C. J. Tassone, V. L. Pool, A. Gold-Parker, R. Cheacharoen, K. H. Stone, E. T. Hoke, M. F. Toney, M. D. McGehee, *Chem. Mater.* **2014**, *26*, 7158.

[62] H. Yu, F. Wang, F. Xie, W. Li, J. Chen, N. Zhao, *Adv. Funct. Mater.* **2014**, *24*, 7102.

[63] A. Buin, P. Pietsch, J. Xu, O. Voznyy, A. H. Ip, R. Comin, E. H. Sargent, *Nano Lett.* **2014**, *14*, 6281.

[64] K. Liang, D. B. Mitzi, M. T. Prikas, *Chem. Mater.* **1998**, *10*, 403.

[65] P. Docampo, F. Hanusch, S. D. Stranks, M. Döblinger, J. M. Feckl, M. Ehrensperger, N. K. Minar, M. B. Johnston, H. J. Snaith, T. Bein, *Advanced Energy Materials* **2014**, *4*.

[66] Z.-K. Tan, R. S. Moghaddam, M. L. Lai, P. Docampo, R. Higler, F. Deschler, M. Price, A. Sadhanala, L. M. Pazos, D. Credgington, F. Hanusch, T. Bein, H. J. Snaith, R. H. Friend, *Nat. Nanotechnol.* **2014**, *9*, 687.

[67] J. Schlipf, P. Docampo, C. J. Schaffer, V. Körstgens, L. Bießmann, F. C. Hanusch, N. Giesbrecht, S. Bernstorff, T. Bein, P. Muller-Buschbaum, *J. Phys. Chem. Lett.* **2015**, *6*, 1265.

[68] L. Zheng, Y. Ma, S. Chu, S. Wang, B. Qu, L. Xiao, Z. Chen, Q. Gong, Z. Wu, X. Hou, *Nanoscale* **2014**, *6*, 8171.

[69] W. Nie, H. Tsai, R. Asadpour, J.-C. Blancon, A. J. Neukirch, G. Gupta, J. J. Crochet, M. Chhowalla, S. Tretiak, M. A. Alam, *Science* **2015**, *347*, 522.

[70] Z. Xiao, Q. Dong, C. Bi, Y. Shao, Y. Yuan, J. Huang, *Adv. Mater.* **2014**, *26*, 6503.

[71] Z. Xiao, C. Bi, Y. Shao, Q. Dong, Q. Wang, Y. Yuan, C. Wang, Y. Gao, J. Huang, *Energy Environ. Sci.* **2014**, *7*, 2619.

[72] J. Yin, D. Cortecchia, A. Krishna, S. Chen, N. Mathews, A. C. Grimsdale, C. Soci, *J. Phys. Chem. Lett.* **2015**, *6*, 1396.

[73] K. Tanaka, T. Takahashi, T. Ban, T. Kondo, K. Uchida, N. Miura, *Solid State Commun.* **2003**, *127*, 619.

[74] N. K. Kumawat, A. Dey, A. Kumar, S. P. Gopinathan, K. L. Narasimhan, D. Kabra, *ACS Appl. Mater. Interfaces* **2015**.

[75]   Z.-K. Tan, R. S. Moghaddam, M. L. Lai, P. Docampo, R. Higler, F. Deschler, M. Price, A. Sadhanala, L. M. Pazos, D. Credgington, *Nature nanotechnology* **2014**.

[76]   F. Deschler, M. Price, S. Pathak, L. E. Klintberg, D.-D. Jarausch, R. Higler, S. Hüttner, T. Leijtens, S. D. Stranks, H. J. Snaith, M. Atatüre, R. T. Phillips, R. H. Friend, *J. Phys. Chem. Lett.* **2014**, *5*, 1421.

[77]   H. Zhu, Y. Fu, F. Meng, X. Wu, Z. Gong, Q. Ding, M. V. Gustafsson, M. T. Trinh, S. Jin, X. Y. Zhu, *Nat. Mater.* **2015**, *14*, 636.

3 Characterization

3.1 X-Ray Diffraction

X-ray diffraction (XRD) is a powerful tool to determine the atomic structure of crystalline materials and to analyze the composition of phase mixtures. The principle of XRD measurements is based on the scattering of electromagnetic waves in the Ångstrøm range (X-rays) on structures, which have about the same physical dimension (see Figure 3-1).
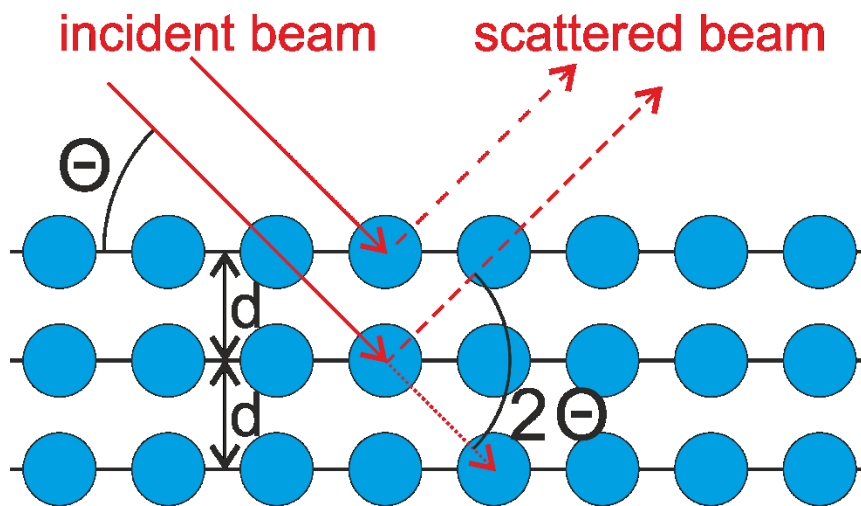
Figure 3-1: Schematic representation of the scattering processes in an XRD measurement

Constructive interference can only occur on periodic lattices of matter and therefore leads to diffraction patterns. The relationship between the angle of constructive interference and the distance of lattice planes (d) is given by Bragg's law:

$$n\lambda = 2d \sin(\theta) \tag{1}$$

where n is the order of interference, λ is the wavelength of X-rays (usually Cu Kα: $\lambda = 1.540562$ Å), d is the lattice spacing and θ is the angle of incidence. The dimension of structures that can be resolved is in a range of about 0.1 nm to 20 nm, if angles from 0.5° 2θ to 100° 2θ are considered.[1]

3.2   Scanning Electron Microscopy (SEM)

Scanning electron microscopy (SEM) is a useful tool to characterize surfaces and morphologies at the nanoscale. The typical setup is depicted in Figure 3-2.
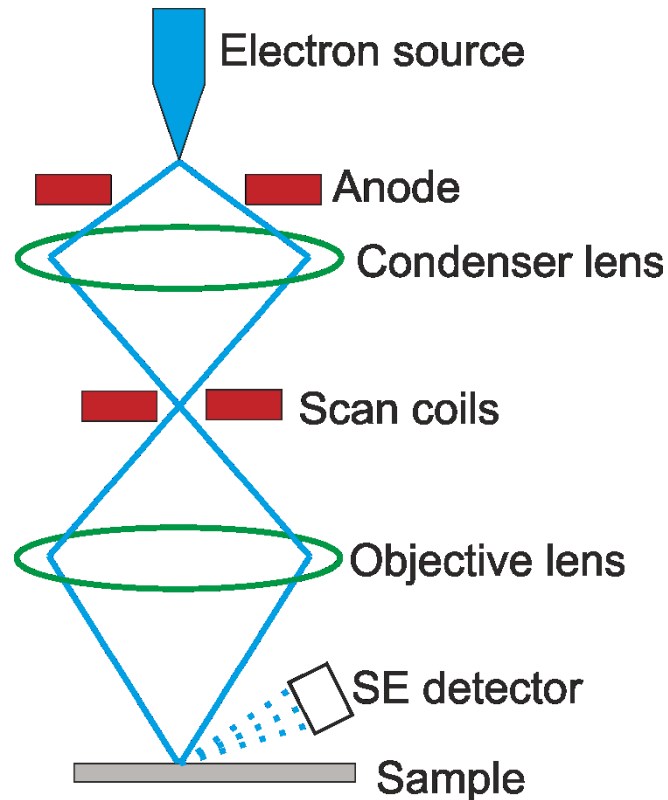
Figure 3-2: Typical set-up of a scanning electron microscope (SEM)

An electron beam is created in the electron source, which is typically a heated tungsten filament with a voltage of 3 to 30 kV applied. The electrons are accelerated with an aperture-like anode and the beam is focused on the sample with various condenser lenses and moved around with the help of the scan-coils. When the beam hits the specimen several things can happen: The electron beam can simply be transmitted through the sample, gaining phase and diffraction information (TEM), it can be backscattered from the surface (BE), remaining almost constant in energy, or, necessary for SEM measurements, can be absorbed by the sample. These absorbed electrons will relax within the sample and can be emitted again as electrons with lower energy, so-called secondary electrons (SE).

These secondary electrons can be detected with an SE detector, which is placed at a certain angle to the sample holder. In this way different heights and surface orientations, as well as the composition of the illuminated spot, have a strong influence of the amount of secondary electrons reaching the detector. By scanning the sample surface point for point with the electron beam and recording the SE intensity for each point, it is possible to generate a microscopic image of the sample.[2]

Furthermore, when an atom is hit by an electron beam, it emits characteristic radiation, typically X-rays. The energy of the emitted radiation depends on the atomic structure of the atoms in the sample. These X-rays are sorted by wavelength in the analyzer and recorded by an X-ray detector. The obtained spectrum can be used to estimate the atomic composition of the analyzed sample. This technique is called energy dispersive X-ray spectroscopy (EDX).[3]

3.3   UV-Vis Absorption Spectroscopy

Ultraviolet-Visible (UV-Vis) spectroscopy can provide valuable insights in the electronic structure of materials by probing optical transitions from the ground state to various excited states. This method can be applied for the quantitative and qualitative determination of the absorption properties of liquid as well as solid samples.

In a liquid sample, where the chromophore is dissolved in a suitable solvent at a concentration where molecular interactions are negligible, the absorbance A at a certain wavelength is defined in equation 2, where I is the measured intensity and I_0 the intensity of the incident beam (measured without inserted sample).

$$A(\lambda) = -log\frac{I(\lambda)}{I_0(\lambda)} \tag{2}$$

3.3. UV-Vis Absorption Spectroscopy

The absorbance is related to the concentration of the absorbing species via the Lambert-Beer law (equation 3), where A is the absorbance at a certain wavelength λ, ε the specific absorption coefficient, c the concentration and L the optical path length.

$$A(\lambda) = \varepsilon(\lambda)\, c\, L \tag{3}$$

The determination of the amount of light absorbed can become more difficult if the sample is not perfectly translucent, but involves scattering parts, as is normally the case for solar cells supported on a transparent conductive oxide substrate. Due to the different refractive indices of the different layers in a solar cell, light is scattered and refracted at the interfaces between the different layers. In a simple model geometry for the determination of the absorption in the active layer of a solar cell (sample on glass substrate), there are already three interfaces present that involve scattering of light, namely the air-substrate, the substrate-sample and the sample-air interface. In a fully assembled solar cell this becomes even more complicated, as a solar cell typically also contains various charge selective layers as well as a reflective metal electrode.

The Lambert-Beer-Law is not applicable for the determination of the absorbance in such complicated samples. Instead, a reliable determination of the absorbance can be achieved by optical modelling based on the optical constants of each individual layer,[4] or measurements with an integrating sphere corrected by choosing a suitable reference.[5]

The following procedure has been found to produce reliable results for a wide variety of thin films samples and has been used throughout this thesis to estimate aborption in thin films:[6]

It is assumed that all light is either absorbed, transmitted or reflected by the sample. The intensity of the incident light can therefore be written as percentages of absorbed (%A), reflected (%R) and transmitted (%T) light.

$$\%A + \%R + \%T = 1 \tag{4}$$

The different components of the light can be determined by transmission and reflectance measurements of the reference and sample with the help of an integrating sphere.

For the transmittance measurement the sample has to be positioned just at the entrance port of the integrating sphere. This way, all the transmitted light and the light scattered toward the edges of the sample is collected. For reflectance measurements the sample is positioned at the opposite end of the integrating sphere, just outside of the sphere. Only light reflected from the surface will be taken into account in this measurement. These measurements have to be performed for the reference and the sample. A suitable reference for thin film samples is the supporting transparent substrate without the active layer. Additionally, the instrument transmission baseline (100% T) without any optical obstacles in the beam path and a Spectralon white standard (100% R) have to be acquired.

According to equation 4 the absorbance for each the sample and the substrate can be calculated from the reflectance and transmittance. The absorption can be calculated from the absorbance following equation 5.

$$A = -\log(1 - \%A) \tag{5}$$

The absorption of the active layer is therefore the absorption of the complete sample reduced by the aborption typical for the substrate (reference).

3.4 Photothermal Deflection Spectroscopy (PDS)

Photothermal deflection spectroscopy (PDS) is a tool to estimate wavelength dependent optical absorption in thin film samples. In contrast to conventional UV-Vis spectroscopy, PDS is not influenced by scattering and can detect light absorption 4 to 5 orders of magnitude lower.[7]

3.5. Steady State Photo Luminescence (ssPL)

A schematic PDS setup is depicted in Figure 3-3. The sample is irradiated with a monochromatic light beam normal to the sample surface. Upon absorption of the light the sample heats up via non-radiative relaxation and creates a thermal gradient at the surface reaching into the surrounding medium. The temperature change leads to a change in refractive index. This refractive index gradient can be increased by immersing the sample in an inert liquid that features a high change in refractive index per change in temperature. This changed refractive index is probed with a CW laser that is directed parallel and very close to the sample surface. Due to the varying refractive index in the light path through the medium, the beam is deflected. The angle of deflection is a measure for the change in refractive index and therefore the temperature increase in the sample induced by and proportional to the absorption of light. By scanning the monochromatic pump beam through various wavelengths, an absorption spectrum can be recorded.
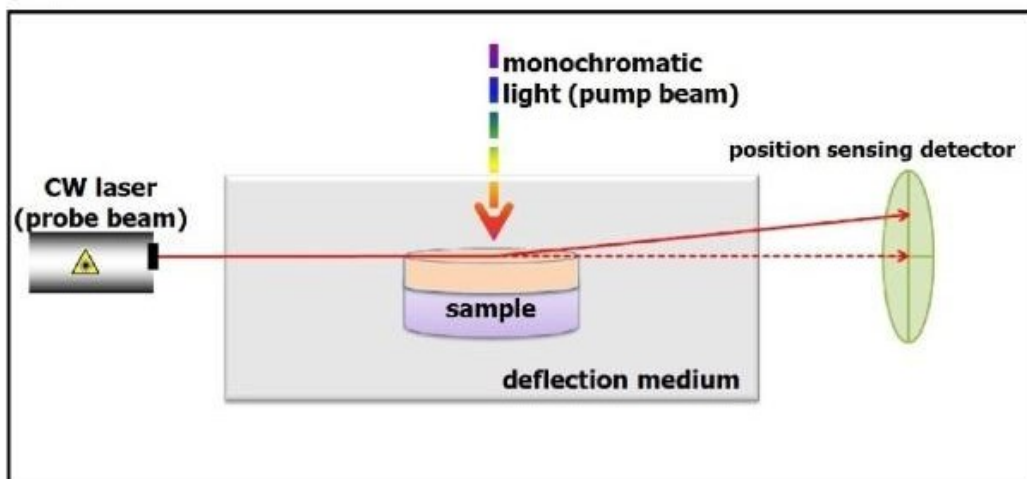

Figure 3-3: Schematic representation of the PDS set-up.

3.5   Steady State Photo Luminescence (ssPL)

Upon photo-excitation of an electron in a semiconductor, excited states within the conduction band are occupied. These states will rapidly thermalize to the ground state of the conduction

band. The energy difference between the conduction band and the valence band (band gap), however will most likely be released in the form of a photon. A schematic representation of the absorption and emission processes is depicted in Figure 3-4.

Since the emitted photons possess the energy of the bandgap, valuable information of the energy levels of a certain sample can be obtained by recording the photoluminescence signal.
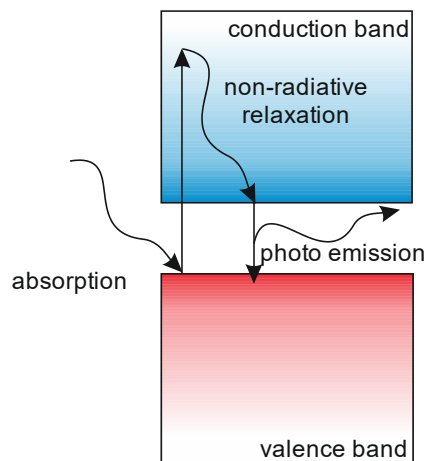
Figure 3-4: Schematic representation of absorption and relaxation processes leading to photoluminescence

3.6 Time Correlated Single Photon Counting (TCSPC)

Time correlated single photon counting (TCSPC) is similar to ssPL in terms of the origin of the signal. However, while in ssPL only the absolute energy and the intensity of the emitted photons is registered, TCSPC offers the possibility to record the time-resolved kinetics of photoemission from the band-edge. TCSPC is based on the repetitive and precisely timed registration of single photons emitted from the sample.

In a typical experimental set-up, the sample is excited with a pulsed laser source. Every laser pulse starts a stopwatch, which is used to measure the time until a photon is detected. As depicted in Figure 3-5 the time difference between the photo excitation and emission is not a constant value. As quantum mechanics predict, it is not possible to know when exactly the

relaxation process will occur. All we can predict about the lifetime of an excited species is its statistical expectation over time.
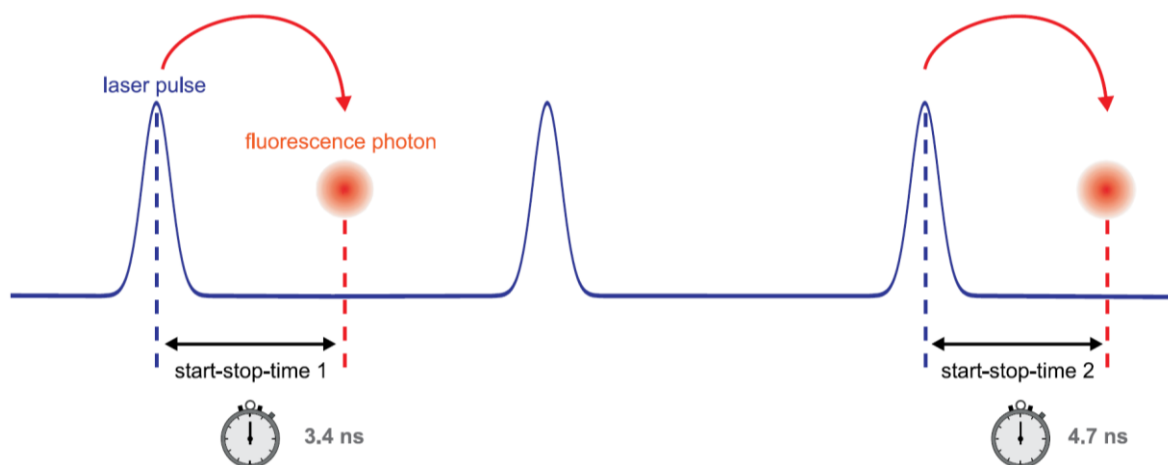
Figure 3-5: Measurement of start-stop times in a time-resolved fluorescence measurement with TCSPC.[8]

Therefore, it is not possible to determine the photoluminescence decay dynamics in a single experiment. In a typical TCSPC experiment the laser is pulsed at frequencies between 100 kHz and 80 MHz, so that a single experiment consists of a multitude of individual single photon measurements. It is important to ensure that the excitation source is weak enough to allow a maximum of one photoemission event per laser pulse cycle. Every individually measured decay time is sorted into a histogram consisting of a range of time bins (Figure 3-6).

The resulting histogram normally shows an exponential decrease along the time axis. This again is due to the quantum mechanical interpretation of decay processes, where it is only known that half of the excited species will decay in a given time interval. The exponential decay can be fitted with a matching function to extract this half-life time.
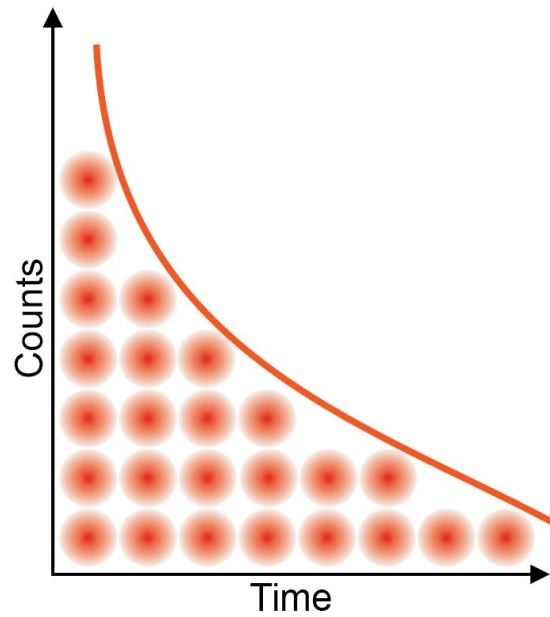
Figure 3-6: Histogram of start-stop times in time-resolved fluorescence measurement with TCSPC[8]

3.7 Current-Voltage Measurements

Solar cells are generally rated and compared to each other by their power conversion efficiency (PCE, η). To ensure comparable results in different laboratories, the testing takes place under standardized conditions, i.e. light intensity. The current standard for solar cell measurements is the ASTM G173-03 air mass 1.5 global (AM1.5G) at a total light intensity of 100 mW/cm^{-2} (1 sun).[9] This spectrum corresponds to the standard spectrum emitted by the sun corrected for absorption and scattering by the atmosphere.

The efficiency of a solar cell is obtained by performing current-voltage (IV) measurements under 1 sun illumination. For this measurement, a range of voltages is applied to the test-device and the resulting current flowing through the solar cell is recorded. A typical IV-curve for a perovskite solar cell is shown in Figure 3-7.

3.7. Current-Voltage Measurements
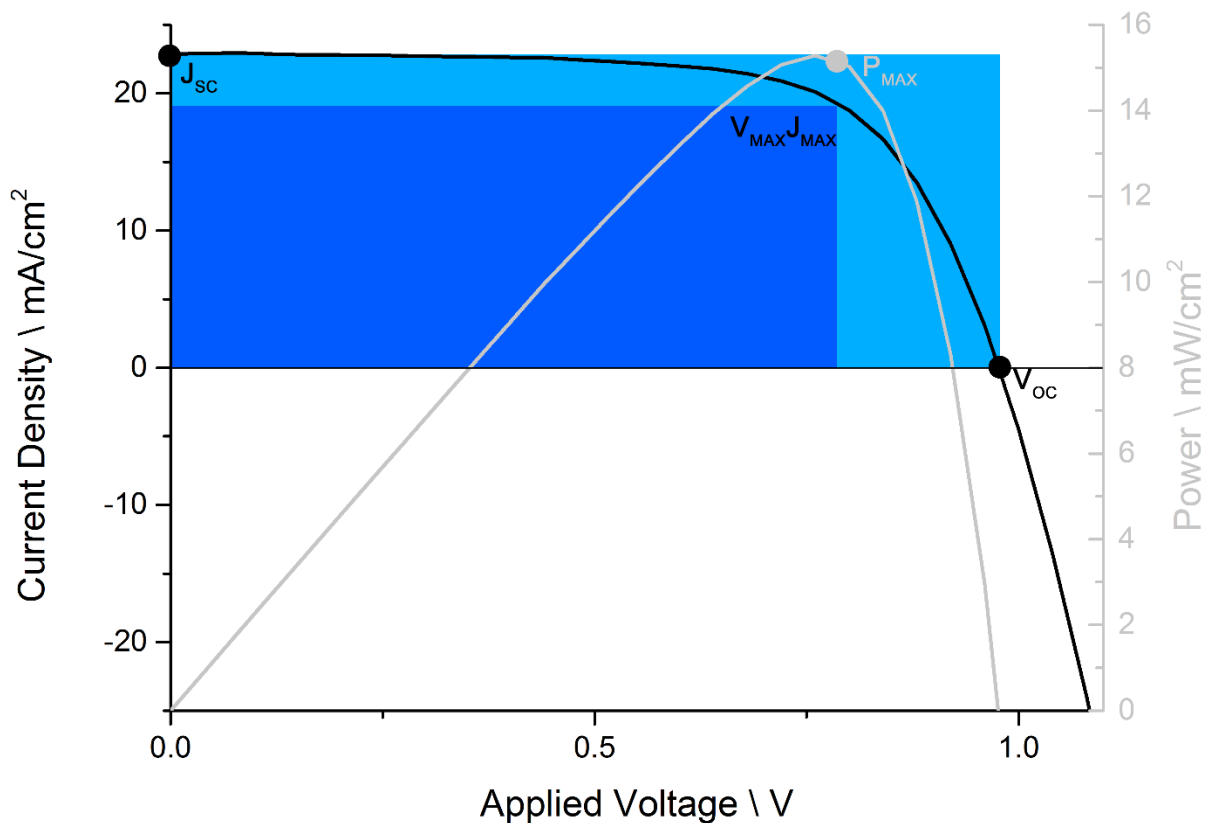
Figure 3-7: Typical I-V and power curve for a perovskite solar cell.

The characteristic points in the IV curve are the short circuit current (J_{SC}) and the open circuit voltage (V_{OC}). The short circuit current corresponds to the current running through the cell with no applied bias voltage. It depends on its optical absorption, the tendency to produce charge carriers under illumination and the transport of these charge carriers to the electrodes. The open circuit voltage is the voltage that has to be applied to neutralize the internal electrical field of the solar cell, so that no current flows.

The product of J_{SC} and V_{OC} corresponds to the power that is produced by the cell at any given applied voltage. The point where the power curve is at its maximum value is called the maximum power point (P_{MAX}) and indicates the voltage needed for the solar cell to perform the most efficiently. P_{MAX} is related to the PCE via the relation

$$PCE = \frac{P_{MAX}}{P_{in}} = \frac{V_{MAX} \cdot J_{MAX}}{P_{in}} \qquad (6)$$

where P_{in} is the power of the incident light.

To determine how good the performance of a solar cell is with respect to its maximum possible efficiency, set by the J_{SC} and V_{OC}, the fill factor (FF) was introduced. It is defined as

$$FF = \frac{V_{MAX} \cdot J_{MAX}}{V_{OC} \cdot J_{SC}} = \frac{P_{MAX}}{V_{OC} \cdot J_{SC}} \qquad (7)$$

This equals the ratio between the light blue and dark blue rectangle in Figure 3-7. For a good working solar cell the fill factor should be above 70 %.

3.8   Incident Photon to Current Conversion Efficiency (IPCE)

While standard IV measurements can only tell something about the overall efficiency of a solar cell under sun-like white light illumination, it can be interesting to see how a solar cell reacts to a monochromatic illumination. This kind of measurement is called incident photon to current conversion efficiency (IPCE) or external quantum efficiency (EQE) measurement. The IPCE can be expressed as

$$IPCE(\lambda) = \eta_{LHE} \cdot \eta_{inj} \cdot \eta_c \qquad (8)$$

where η_{LHE} is the light harvesting efficiency, η_{inj} the electron injection efficiency and η_c is the electron collection efficiency. For the measurement, the solar cell is illuminated with monochromatic light and the resulting short circuit current ($J_{SC}(\lambda)$) of the solar cell is recorded in dependence of the incident wavelength λ. It can be calculated as

3.9. Cyclic Voltammetry

$$IPCE(\lambda) = 1240 \frac{J_{SC}(\lambda)}{\lambda \cdot P_{in}} \tag{9}$$

where λ is the wavelength and P_{in} the power of the incident light. The overall short circuit current J_{SC} under white light illumination can therefore be calculated as the integral of the product of the wavelength dependent $IPCE(\lambda)$ and the incident photon flux density ($F(\lambda)$) following the expression

$$J_{SC} = \int e \cdot F(\lambda) \cdot IPCE(\lambda) d\lambda \tag{10}$$

where e is the elemental charge of an electron. For an ideal solar cell measurement the J_{SC} calculated from IPCE measurements should be equal to the J_{SC} obtained from white light measurements.

3.9 Cyclic Voltammetry

Cyclic Voltammetry (CV) is a type of potentiodynamic electrochemical measurement. It is generally performed in a three-electrode setup, consisting of a working electrode (the sample), a counter electrode (typically a platinum mesh) and a reference electrode (for example a Ag/Ag^+ reference electrode) immersed in an electrolyte. The voltage applied between the working and the counter electrode is increased and decreased linearly in a cycling manner (sawtooth potential) and the current flowing is recorded. Figure 3-8 shows the time-dependent trace of the applied voltage. Starting from a certain potential at t_1 (equals t_5) the voltage is increased to the setpoint at t_3, passing the standard potential of the sample at t_2. After reaching the setpoint, the voltage is again linearly decreased past the red-ox potential (t4) to an opposite turning point at t_5. From now on, the value of the applied potential is cycled between the two extreme values and the current is continuously recorded in dependence of the voltage.
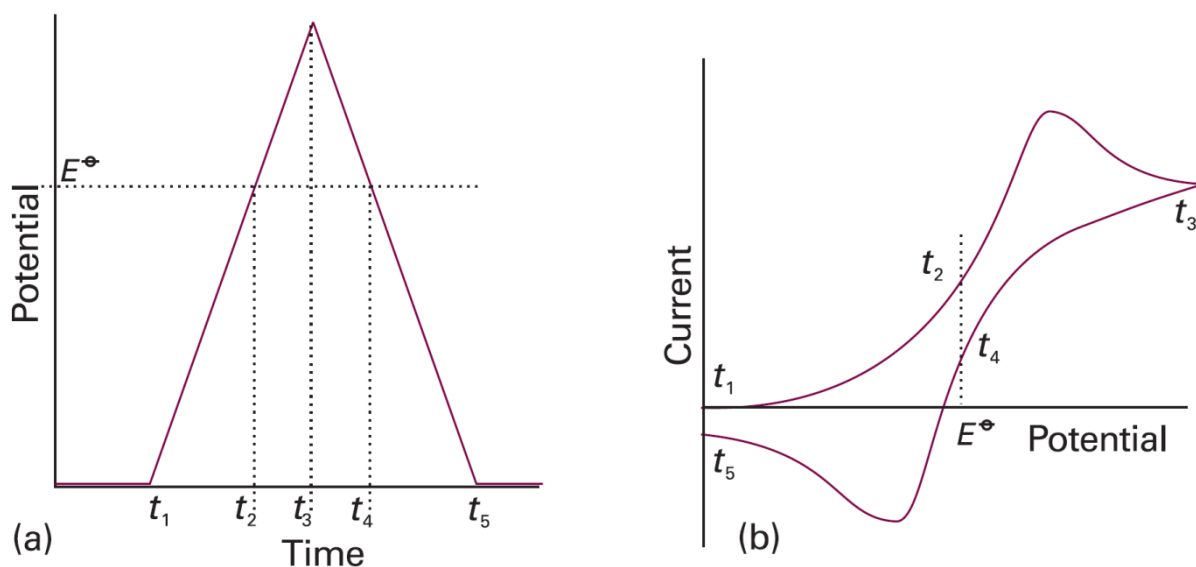
Figure 3-8: Time-dependent trace of the voltage applied between the working and the reference electrode in a CV experiment (a) and potential dependent current flowing between the working and the counter electrode (b).[10]

When first applying a reducing potential (from t_1 to t_3) the cathodic current will increase until all reducible species in the sample are reduced. From this point on, the current will decrease even when higher potentials are applied. After the applied voltage has reached the set-point (t_3) it is reversed (to t_5). At some point during the reverse scan the sample will be re-oxidized (if the reduction is reversible) and an anodic current peak can be monitored. The more reversible the red-ox reaction is, the more symmetric is the reduction and oxidation peak to the standard potential $E^\ominus$. Hence, cyclic voltammetry is a suitable tool to gain insights over the reduction and oxidation potentials of the analyzed samples.

3.10 Literature

[1]   W. H. Bragg, W. L. Bragg, *The Reflection of X-rays by Crystals*, Vol. 88, **1913**.

[2]   M. von Ardenne, *Z. Physik* **1938**, *109*, 553.

[3]   C. G. Barkla, C. A. Sadler, *Lond. Edinb. Dubl. Phil. Mag.* **1909**, *17*, 739.

[4]   G. F. Burkhard, E. T. Hoke, M. D. McGehee, *Adv. Mater.* **2010**, *22*, 3293.

[5]   H. J. Snaith, C. Ducati, *Nano Lett.* **2010**, *10*, 1259.

[6]   B. M. Klahr, A. B. F. Martinson, T. W. Hamann, *Langmuir* **2011**, *27*, 461.

[7]   W. B. Jackson, N. M. Amer, A. C. Boccara, D. Fournier, *Appl. Opt.* **1981**, *20*, 1333.

[8]   M. Wahl, *Technical Note: Time-Correlated Single Photon Counting (TCSPC)*, PicoQuant GmbH, Berlin, **2014**.

[9]   http://rredc.nrel.gov/solar/spectra/am1.5/

[10]   P. Atkins, J. de Paula, *Atkins' Physical Chemistry*, Oxford University Press, Oxford, UK **2006**.

4 Solution Deposition-Conversion for Planar Heterojunction Mixed Halide Perovskite Solar Cells

This chapter is based on the following publication:

Pablo Docampo*, Fabian C. Hanusch*, Samuel D. Stranks, Markus Döblinger, Johann M. Feckl, Martin Ehrensperger, Norma K. Minar, Michael B. Johnston, Henry J. Snaith, Thomas Bein, *Advanced Energy Materials* **2014**, *4*, DOI: 10.1002/aenm.201400355.

*These authors contributed equally to this work

4.1 Introduction

Alkylammonium metal trihalide perovskite absorbers first employed in working photovoltaic devices were based on liquid electrolyte sensitized solar cells. Introduced by Kojima *et al.*, they exhibited a starting point power conversion efficiency of 3.8% with further work quickly extending it to over 6%.[1, 2] It wasn't until a solid-state configuration was employed, however, that high device efficiencies were achieved.[3-5] Initial results were reported at 9% for perovskite sensitized titania-based devices, [4] and further improvements were simultaneously achieved in a "meso-superstructured" configuration by replacing the mesoporous TiO_2 scaffold with an electronically inactive mesoporous Al_2O_3 layer, exhibiting device efficiencies of over 12%.[5-7] Some of the key advantages for this material system over other competing device concepts are that they are compatible with solution-processing techniques and can be fully processed at low temperatures, enabling their use in flexible device applications.[8]

Recently, Burschka *et al.* have demonstrated a method whereby an initial PbI_2 film is deposited over a mesoporous TiO_2 structure, which is then fully converted into the methylammonium lead triiodide ($MAPbI_3$) perovskite via a second step.[9] The lead iodide coated substrates are

4.1. Introduction

immersed in a methylammonium iodide (MAI) solution in isopropanol for a short time (< 1min), resulting in the conversion of PbI_2 into the perovskite phase. The resulting films are coated with the hole transporter 2,2',7,7'-Tetrakis[N,N-di(4-methoxyphenyl)amino]-9,9'-spirobifluorene (Spiro-MeOTAD) and a metal cathode, resulting in solar cells which approach the 15% benchmark.[10] Recently, this fabrication method was extended for planar heterojunction based devices by Liu *et al.* where a planar PbI_2 film was deposited over a ZnO blocking layer, and was then converted into the $MAPbI_3$ perovskite in a second step. [11] This resulted in perovskite crystal sizes ranging from 100 to 1000 nm and an average thickness of ~300 nm. The resulting device performance of 15.7% is currently the highest performance achieved for perovskite solar cells, pointing towards planar heterojunction devices as a promising device architecture for further technological improvements.

The short circuit currents demonstrated for the devices prepared by Liu and coworkers of 20.4 mAcm^{-2},[11] while high, are still short of the maximum current of over 22 mAcm^{-2} reasonably achievable, taking into account other light capture losses for this material.[6] A crucial limitation in this respect is the low diffusion length of the photoexcited species in the $MAPbI_3$ perovskite of around ~100 nm.[12, 13] This parameter can be greatly extended with the inclusion of chloride in the precursor solution to over 1 μm.[12, 14] Furthermore, it has been recently shown that the inclusion of chloride is beneficial for charge transport in the photoactive layer.[15] It is expected that the addition of chloride results in improved short circuit currents and thus overall photovoltaic performance. It is worth noting here that for devices incorporating mesoporous TiO_2 photoanodes, the neat triiodide perovskite functions efficiently without the need for the extended diffusion length of the photoexcited species.[16, 17] This is a result of the interpenetrated nature of the collection photoanode, which exhibits pore sizes in the order of tens of nanometers, which in effect reduces the distance electrons must travel to this magnitude

before being collected. In the case of planar heterojunctions, electrons must travel the whole thickness of the film, which can sometimes exceed hundreds of nanometers and thus extended diffusion lengths are a requirement for efficient operation.

Here we present planar, fully solution-processed heterojunction solar cells based on the solution deposition-conversion technique. We highlight the criticality of chloride in MA lead halide perovskites via a controlled addition of methylammonium chloride (MACl) to the MAI immersion solution. The resulting devices exhibited power conversion efficiencies approaching 15%, and more importantly, showed short circuit currents of over 22 mAcm^{-2}, representing a gain of over 10% over state-of-the-art devices.[11] The parameter most influenced by the presence of chloride is the photoluminescence lifetime of the phot:oexcited species in the device, which reaches values exceeding 300 ns, matching previously reported results for the solution processed mixed halide perovskite films.[12] Additionally, a reduction of series resistance from 14 to 7 Ωcm^2 was also observed.

4.2   Results and Discussion

The solar cells developed in this work are composed of a TiO$_2$/Perovskite/Spiro-MeOTAD planar heterojunction, deposited on an FTO electrode and capped with a gold electrode (Error! eference source not found.).

4.2. Results and Discussion
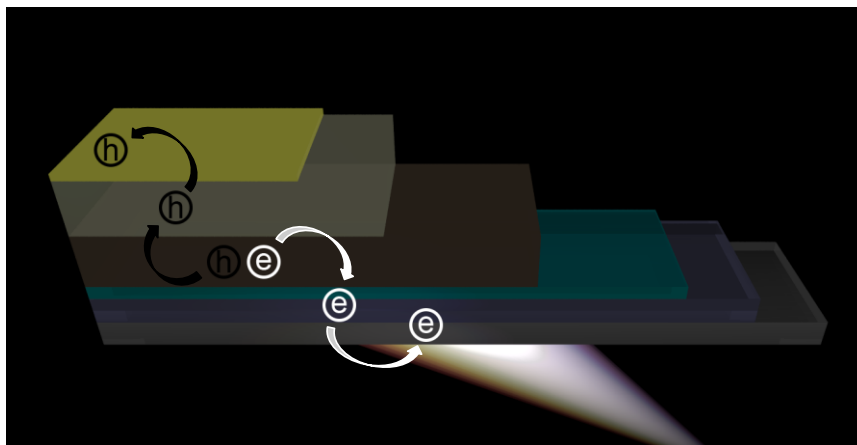
Figure 4-1: Schematic of the device structure. The expected charge transfer process is denoted via arrows.

The perovskite deposition was performed in two steps: firstly, a ~200 nm PbI_2 film was deposited via spincoating, followed by full conversion into the $MAPbI_{3-x}Cl_x$ perovskite via immersion in a heated solution of a mixture of MAI and MACl in isopropanol (IPA). A cross section of the final device structure can be seen in Figure 4-2e. The initial PbI_2 film is shown in the cross sectional image in Figure 4-2a-b, where we can observe distinct PbI_2 sheets, oriented flat over the non-porous TiO_2 layer. The uniformity of the layer can be assessed from Figure 4-2b where we show an extended view of the cross section. Additionally, from the top views shown in Figure 4-2c and d we can see that the layer is smooth and covers 100% of the TiO_2-coated FTO glass substrate. After immersion, we can clearly observe the formation of the perovskite crystals, as shown in Figure 4-2g, with a mixture of crystal sizes ranging from approximately 100 to almost 600 nm in length. As can be seen in the low magnification image in Figure 4-2h, the surface coverage is approximately 100%.
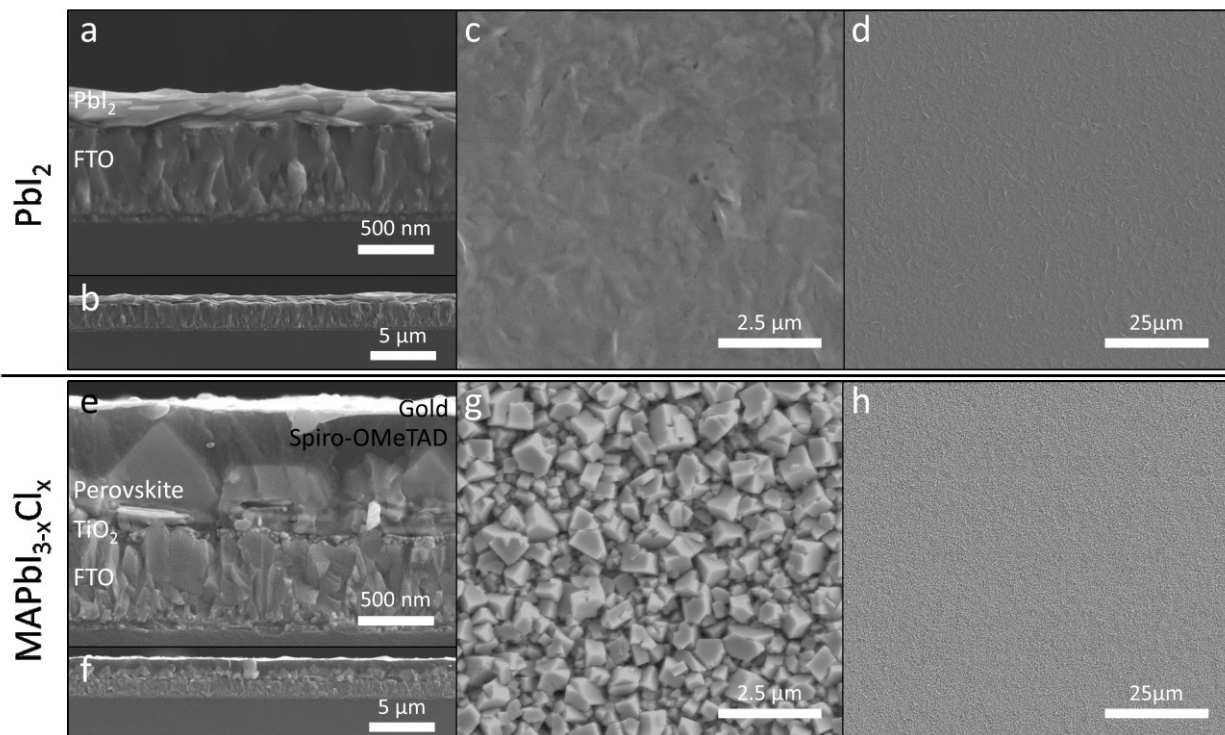
Figure 4-2: a) and b) SEM cross-sectional images of the as-deposited PbI₂ film on TiO₂-coated FTO. SEM top view images of the same PbI₂ films, with high magnification c) and low magnification d). e) and f) SEM cross-sectional images of the fully converted PbI₂ film (from the top row) into MAPbI₃₋ₓClₓ with high magnification g) and low magnification h). All layers are labeled in the image.

To assess the impact of chloride addition on the structure, the films were analyzed via powder XRD after removal from the substrate.
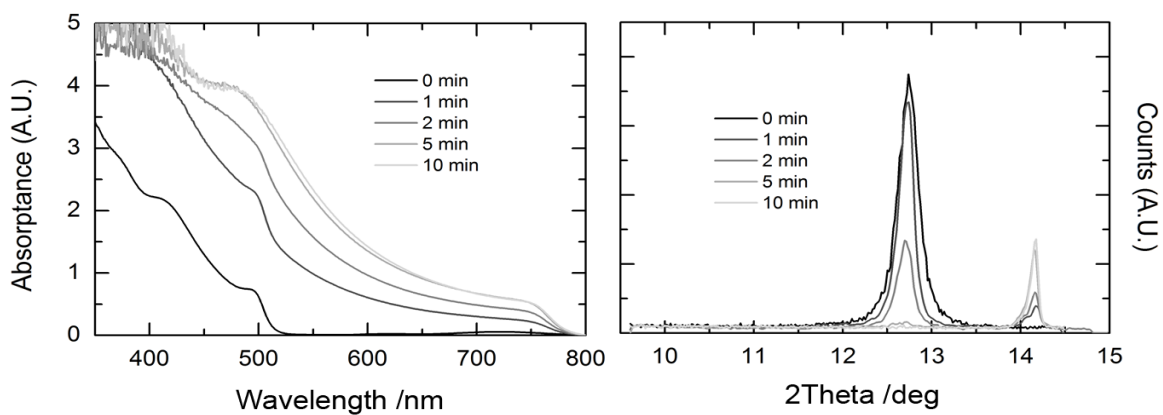
Figure 4-3: (Left): UV-Vis absorption spectrum of the samples immersed in a 10 mgmL⁻¹ MAI solution for different times. The feature at 500 nm corresponds to PbI₂, the absorption onset of the perovskite is at 760 nm. (Right): XRD of the same samples. The feature at 12.6° 2Θ corresponds to the PbI₂ (001) reflection, whereas the features at 14.2° 2 Θ corresponds to the perovskite (110) and (002) reflections.

4.2. Results and Discussion

The perovskite films presented here are phase pure, crystallized in the expected tetragonal I4/mcm space group.[18] No impurities were found, in contrast with other solution-deposition methods that usually exhibit a small fraction of crystalline PbI_2 and $MAPbCl_3$ (Figure 4-3).[5, 15]

However, the change of the lattice parameters, attributed to the presence of chloride, reported for perovskites formed within mesoporous scaffolds was not observed for the system presented here.[15] Moreover, samples of $MAPbI_{3-x}Cl_x$ perovskite prepared according to the established protocol in previous studies (spin-coating from a mixture of $MAI/PbCl_2$) also did not show a significant change of lattice parameters.[15, 19] A similar result was found for films grown within mesoporous Al_2O_3 templates (Figure 4-4).
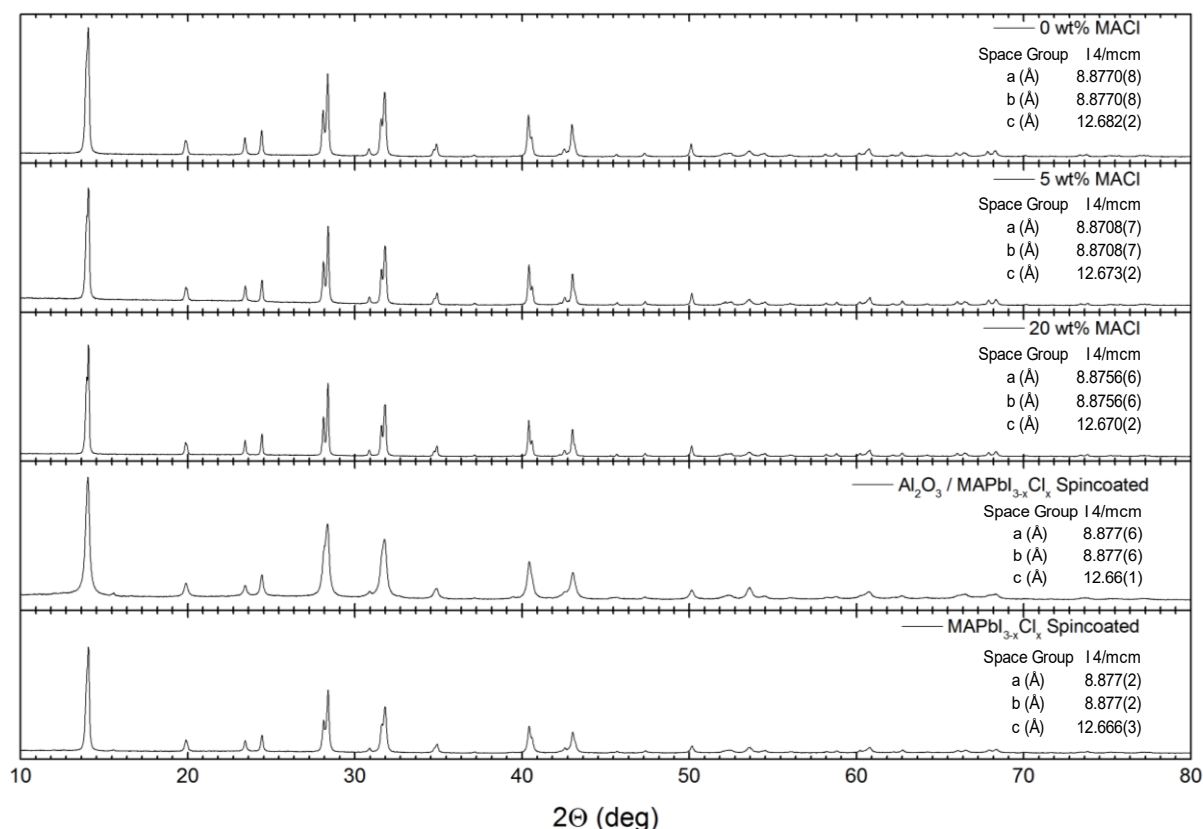
Figure 4-4: Wide angle X-ray diffraction patterns of samples with different Cl⁻-content in the immersion solution and extracted unit cell parameters. All samples crystallize in the I 4/mcm structure with similar lattice parameters. No change in the lattice was observed by adding chloride to the immersion solution. This matches the result obtained for the samples spin-coated from the precursor solution.

This suggests that the vast majority of the chloride ions present in the precursor solution are not incorporated in the final structure. The chloride content in the structure was under the detection limit of both EDX (Figure 4-5) and EELS (Figure 4-6) and could not be quantified.
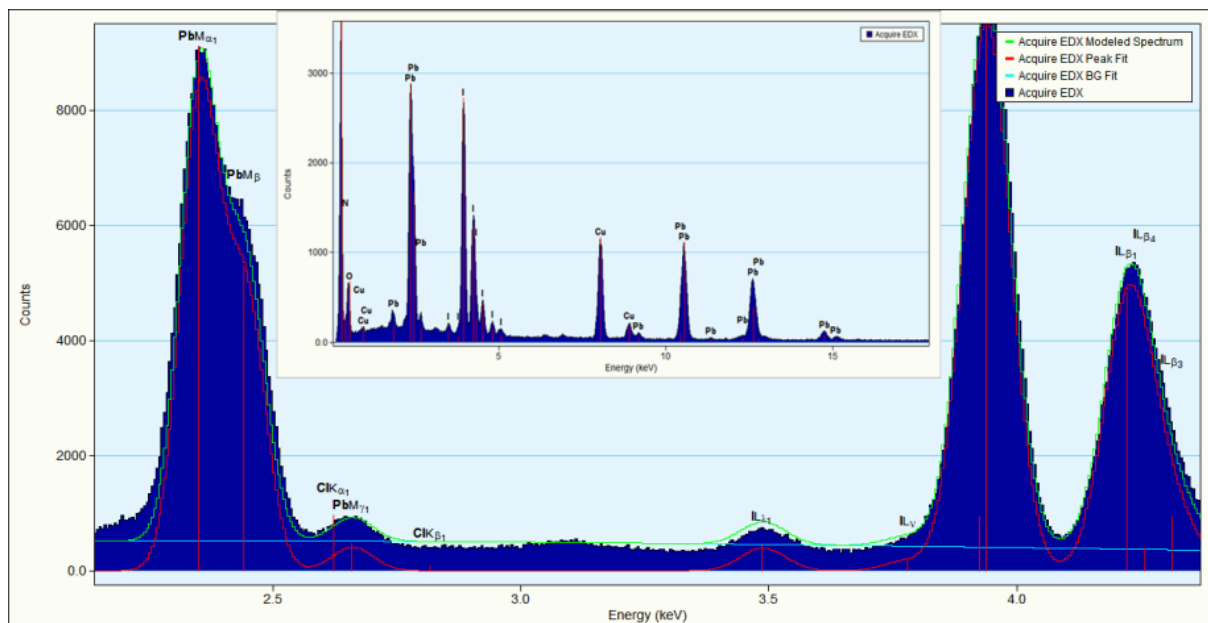
Figure 4-5: **EDX spectrum of MAPbI3-xClx. The spectrum mainly shows Pb, I, C and Cu. The Cu-peaks and a major part of C-signal are due to the sample substrate, a carbon film coated copper grid. A possible Cl signal at 2.6 keV from Cl-K☐ is overlapping with Pb M☐1. The peak fit for the Pb-M lines does not leave any significant intensity to be attributed to the Cl-K line. This means that the Cl concentration is below the detection limit of the setup.**
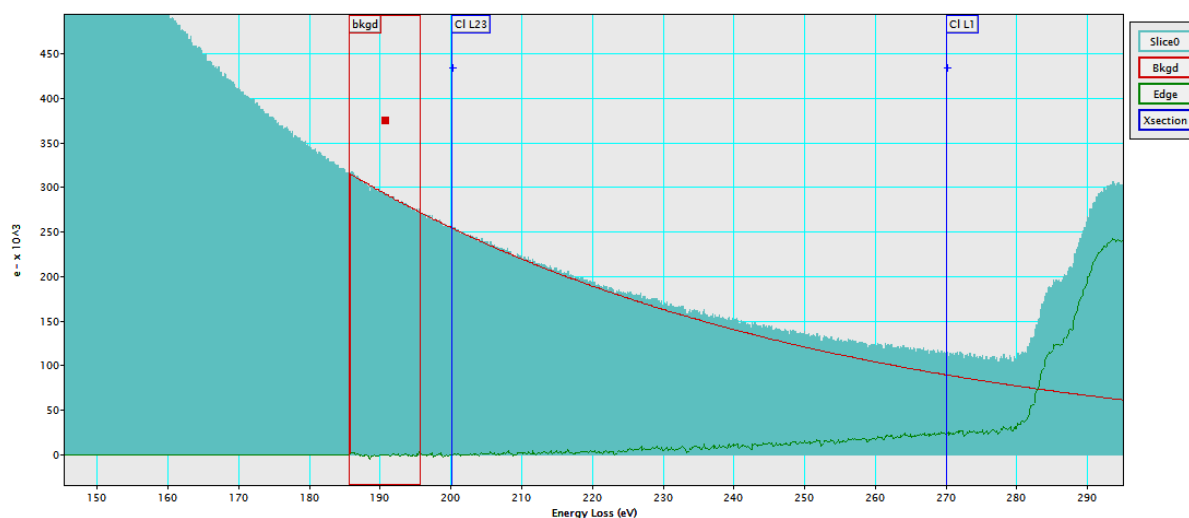
Figure 4-6: EEL spectrum of MAPbI$_{3-x}$Cl$_x$. The relevant edges typical for Cl at 200 eV loss could not be detected.

4.2. Results and Discussion

We have also performed XPS measurements to check whether the chloride sits on the crystal surface as shown in Figure 4-7. Again as was the case for other detection methods, the amount of chloride was below the detection limit of the instrument. Additionally, we have performed coulometric titration with silver ions, colorimetry with mercurythiocyanate and Fe^{3+} ions as well as elemental analysis. However, the iodide signal present in all these measurements heavily interferes with the small chloride signal and therefore the amount of the latter in the structure could not be quantified. For samples incorporating more than 20wt% of MACl in the immersion solution a secondary $MAPbCl_3$ phase was formed and thus this concentration was chosen as the upper limit.
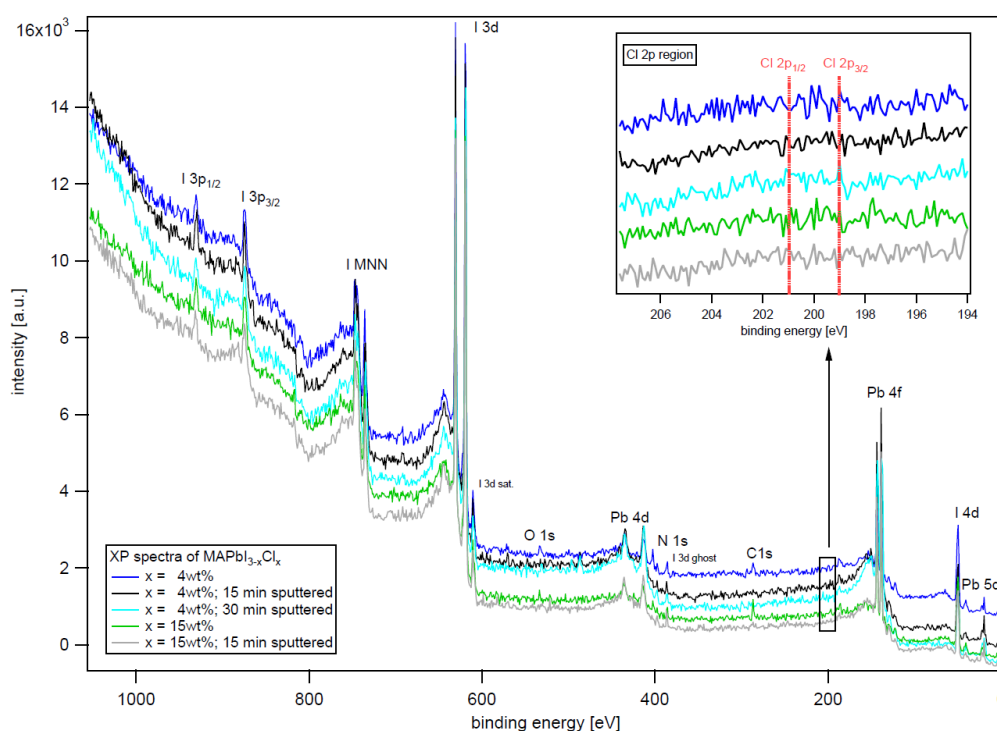
Figure 4-7: Survey XP spectra of samples containing different nominal Cl amounts. The spectra are taken as received and after additional argon ion polishing (1 keV ion energy) denoted 15 and 30 min sputtered respectively. Inset: detailed spectra of the Cl 2p region. The red dotted lines show the expected peak positions for chloride-containing samples.

The photovoltaic performance of devices incorporating perovskite films fabricated with a range of MACl concentrations in the immersion solution is shown in Figure 4-8. We can clearly see major increases in all device parameters, particularly short circuit current and fill factor, even for low MACl concentrations. The maximum performance was obtained for concentrations of 5 wt% MACl, which resulted in a champion device exhibiting almost 15% power conversion efficiency, 22.8 mAcm^{-2} short circuit current and an open circuit voltage approaching 1 V under 104 mWcm^{-2} equivalent AM 1.5 sunlight.

| MACl	J_{sc}	V_{oc}	FF	η	corr. η	R_s
0	19.0	0.85	0.54	8.80	8.46	14.3
1	22.5	0.94	0.59	12.42	11.94	7.3
5	22.9	0.98	0.69	15.41	14.82	6.8
7.5	20.7	0.96	0.68	13.40	12.88	7.2
10	19.8	0.92	0.67	12.31	11.84	7.4
15	19.4	0.92	0.71	12.57	12.09	7.4
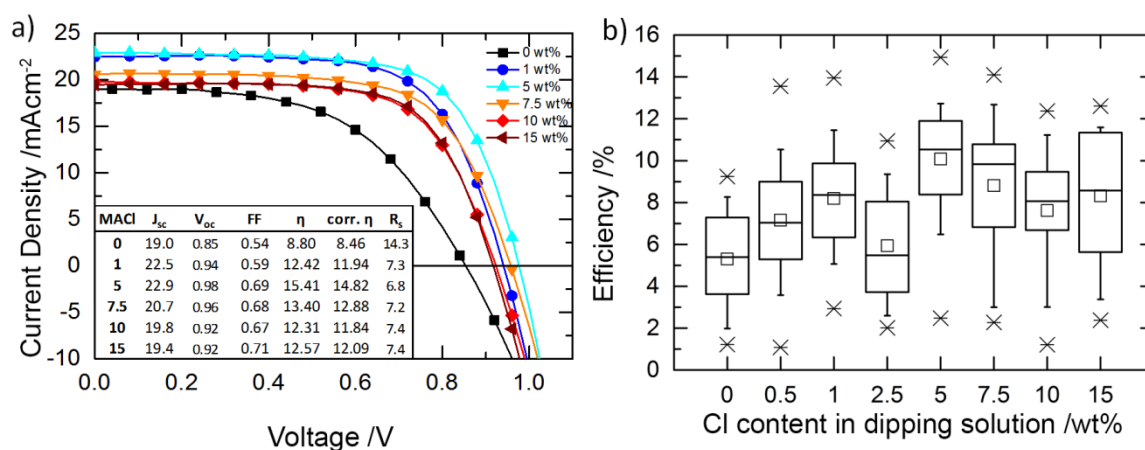
Figure 4-8: a) JV curves measured under AM 1.5 solar irradiance and 104 mWcm^{-2} equivalent light intensity conditions for the best performing MA lead halide perovskite devices for a range of MACl concentrations in the immersion solution. The inset summarizes the photovoltaic parameters: short circuit current (J_{sc}, mA cm^{-2}), open circuit voltage (V_{oc}, V), fill factor (FF, %), power conversion efficiency (η, %), and series resistance (R_s, Ω cm^2). A spectral mismatch factor of 1.02 was calculated for the devices prepared in this study, resulting in an equivalent 104 mWcm^{-2} irradiation intensity.[20] b) The efficiency values are shown as Box plots for efficiency distributions for a range of MACl wt% concentrations in the immersion solution. Whiskers represent the 10/90 percentile while box edges represent the 25/75 percentile. Small square symbol inside the boxes represents the mean, while the line across the boxes represents the median. The X symbols represent the maximum and minimum values. Each box represents the statistical distribution of between 30 and 40 working devices prepared under similar conditions.

The average power conversion efficiency for the optimum fabrication protocol including MACl is 10.5%, as shown on Figure 4-8b, which is much more efficient than the one found for neat triiodide of 5.5%. A histogram of device power conversion efficiencies is shown in Figure 4-9 as well as an Incident Photon to Current Conversion Efficiency (IPCE) spectrum Figure 4-10.

4.2. Results and Discussion
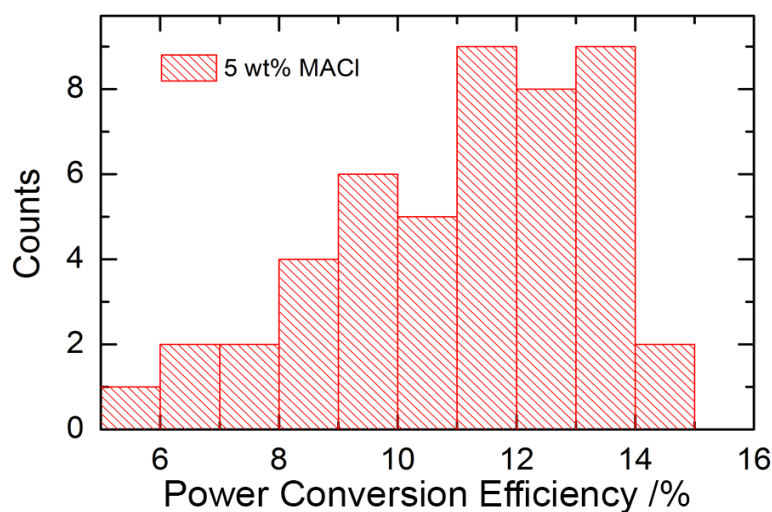
Figure 4-9: Power conversion efficiency histogram for a batch of 40 devices fabricated with 5 wt% MACl in the immersion solution. Most of the devices exhibited a power conversion efficiency between 11 and 14 %.
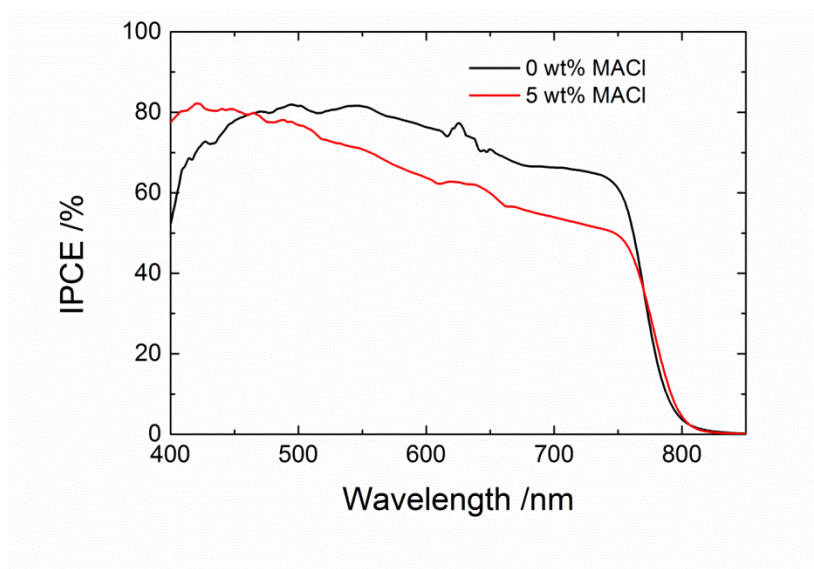
Figure 4-10: IPCE spectrum of the best performing device with 5 wt% MACl in the dipping solution, as well as for a neat triiodide device.

Once this peak MACl concentration is exceeded, the devices start exhibiting both lower short circuit currents and lower voltages. This is very likely due to the observed morphology changes of the films, which exhibit average crystal sizes exceeding those of the neat triiodide by approximately 50% (Figure 4-11), and the appearance of a larger number of gaps between the crystals (Figure 4-12).[12]
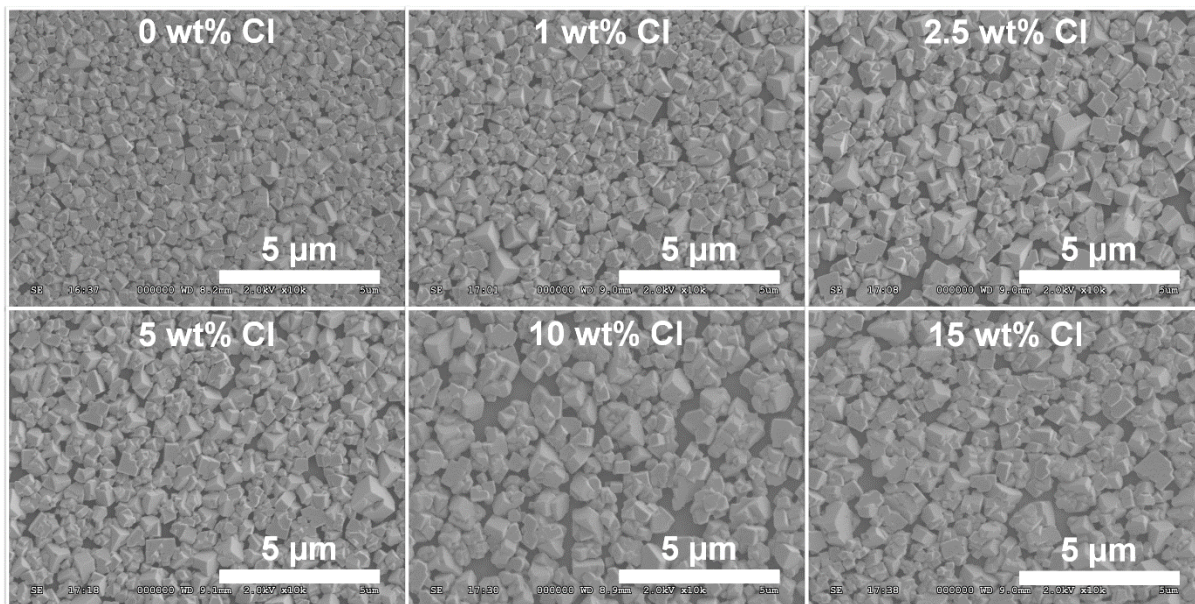
Figure 4-11: Top-view SEM images of perovskite films which were converted with a range of MACl concentrations in the immersion solution.
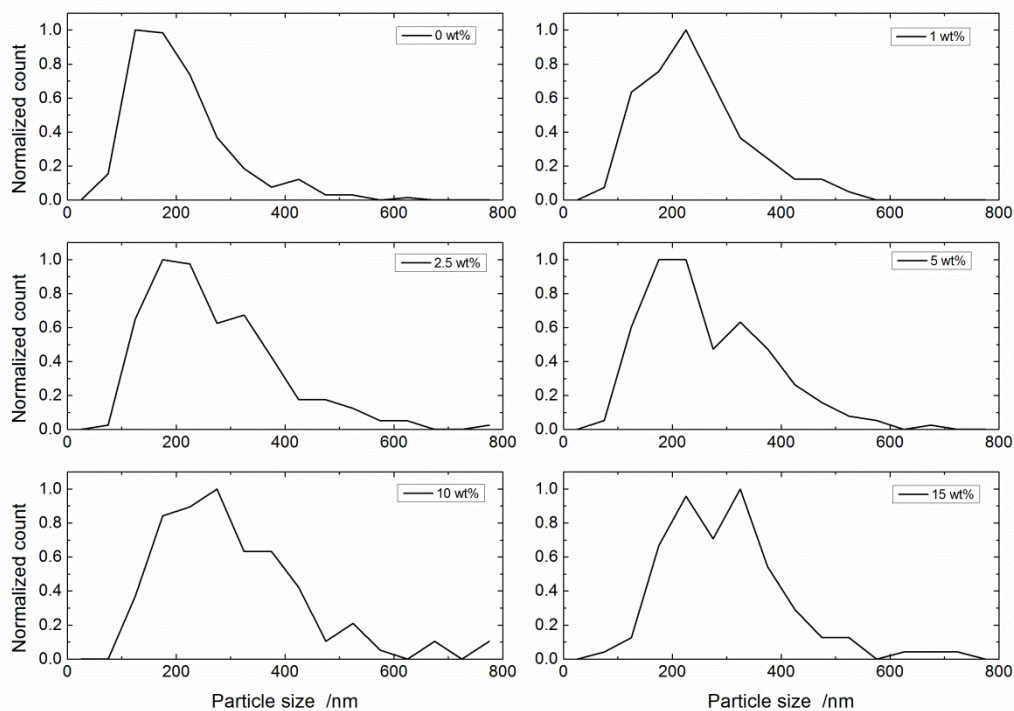
Figure 4-12: Particle size distribution derived from the top-view SEM images presented in Figure S8, obtained through visual analysis.

4.2. Results and Discussion

Additionally, we quantified the series resistance present in the devices (see inset of Figure 4-8a) and observe a decrease from 14 ± 1 to 7 ± 1 Ωcm^2, upon addition of chloride. This clearly accounts for the improvement of the fill factor measured, and is consistent with previous observations of mixed halide perovskites.[15] The neat MAPbI$_3$ solar cells presented here perform significantly worse than state-of-the-art devices presented by Liu and coworkers.[11] This is very likely due to the larger grain size present in our films, as well as the use of a TiO$_2$ blocking layer, which increases series resistance and does not collect charge as efficiently at higher biases. However, the important parameter in terms of this work, short circuit current, is comparable between the two studies and thus represents a valid platform to compare neat and mixed halide perovskite solar cells.

The measured short circuit currents are consistent with those estimated from light absorption measurements inside an integrating sphere (Figure 4-13).

MACl [wt%]	Calculated max J$_{sc}$ [mA/cm²]	Max J$_{sc}$ corrected
0	21.2	22.1
1	21.1	21.9
5	21.5	22.4
10	21.7	22.6
15	22.4	23.3
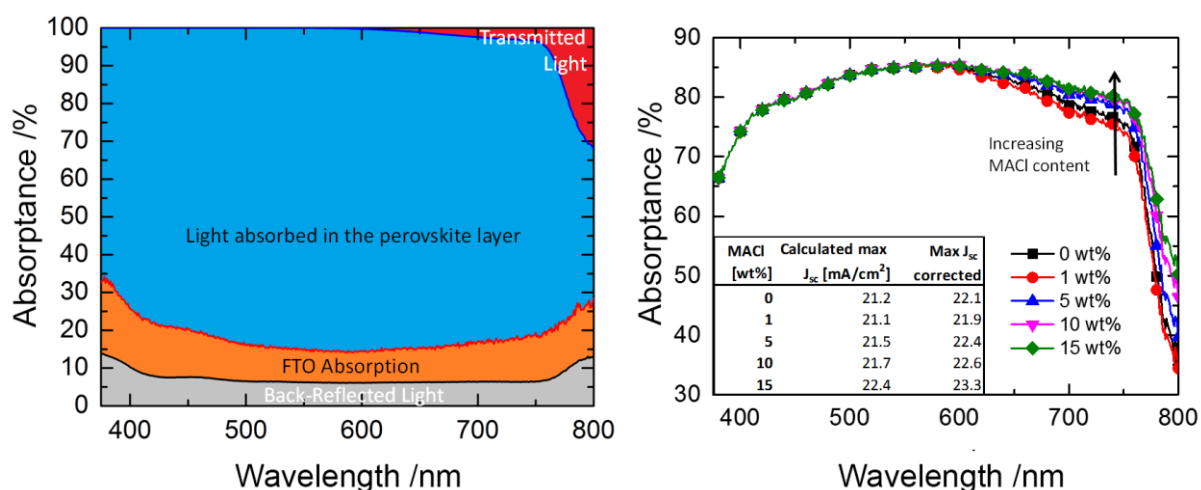
Figure 4-13: (Left): Spectral quantification of the light absorbed in each of the layers of the device, labelled in the figure. (Right): UV-Vis absorption spectrum of perovskite films prepared through the deposition/conversion method with different MACl concentrations in solution. All measurements were taken with an integrating sphere. The optical densities obtained were doubled as a first approximation to account for the 2 passes of light due to the presence of the highly reflective metal electrode. The maximum short circuit current (max _J$_{sc}$_) was estimated by integrating the solar spectrum with the absorptance values after subtracting the device reflectance and contributions from the FTO electrode. The values were corrected for a spectral mismatch of 1.02 and solar simulator lamp power of 102 mWcm^{-2} (denoted as max _J$_{sc}$_ corrected) for direct comparison with the JV curves presented in Figure 3.

We also find that increasing the MACl content in the immersion solution improves light absorption at the bandgap edge due to the marginally higher scattering of these films. However, there is little room for improvement in this regard for the devices prepared here, as only an extra ~5% photocurrent could be gained if 100% of the incoming light were to be absorbed. All the additional losses in overall light harvesting arise from parasitic absorption in the FTO and reflection at the glass/air and glass/FTO interfaces. If no losses were present in the system, a maximum short circuit current of 27.15 mAcm^{-2} could be achieved. Both films fabricated from mixed halide or neat MAI absorb light similarly, however, neat MA lead triiodide films exhibit a 10% lower short circuit photocurrent.

In order to understand this difference, we have performed time-resolved photoluminescence measurements, shown in Figure 4-14and the resulting decay parameters are summarized in Table 4-1.
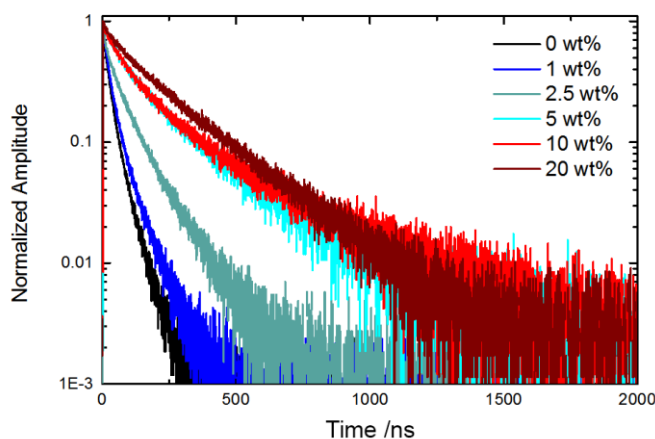

Figure 4-14: Time-resolved PL decay plots of MA lead mixed halide perovskite systems for a range of wt% MACl concentrations in the immersion solutions. The excitation wavelength was chosen at 507 nm, the laser head was pulsed at 500 kHz with an excitation fluence of 0.3 µJcm^{-2}/pulse, and the resulting PL was measured at 778 nm.

4.2. Results and Discussion

This technique yields important information about the lifetime of excited species in photoactive materials and can be used to extract their diffusion length by comparing films with and without a selective charge quencher. [12, 13]. Here, slower decays can be correlated with longer diffusion lengths, indirectly giving a measure of charge collection efficiency for a given film thickness. For the excitation intensity and wavelength used, the PL is expected to arise mostly from recombination of free charges, as the exciton binding strength for this system is relatively low ($E_b \sim 50$ meV).[21-23] For all samples measured, we observe clearly biexponential decay dynamics, which may be a result of the widely varying crystal sizes present in the films, ranging from very small crystals of around 100 nm to some that approach the micron scale. Neat MA lead triiodide films exhibit lifetimes for the fast component of approximately 18 ns and a slow component of ~55 ns (Table 4-1). We note that these decay dynamics are several factors slower than those measured previously for the same triiodide system deposited via spincoating,[12, 13] even for the fast component measured in the devices presented in this work.

Table 4-1: Summary of the biexponential fit decay parameters for the PL decays shown in Figure 4.

MACl content in solution [wt%]	Afast [A.U.]	τfast [± 1 ns]	Aslow [A.U.]	τslow [± 1 ns]
0	1205	18	3494	55
1	2900	22	932	74
2.5	1150	33	1325	112
5	919	91	401	316
10	1018	90	400	364
20	537	80	1016	262

The slower decay dynamics measured here imply that the charge diffusion length is longer than measured previously, allowing efficient charge collection in thicker films so a larger fraction of the solar spectrum can be harvested. Additionally, we note that previous measurements on the PL lifetimes for neat triiodide films were performed on films consisting of very small crystals in the range of tens to a hundred nanometers.[12, 13] We can clearly see that the addition of chloride has a dramatic effect on the dynamics of the photogenerated species, where long

lifetime values of over 300 ns were found for films immersed in a solution mixture exceeding 5 wt% of MACl, consistent with recent results for mixed halide perovskites.[12] Increasing the concentration of MACl beyond this point does not result in longer lifetimes, consistent with previous calculations which predict that only a very small fraction of the chloride ions can in fact be incorporated in the structure.[15]

The differences in PL lifetime may account for the observed losses in short circuit photocurrent. Diffusion lengths could not be calculated for the presented films since the roughness of the perovskite film prevents a reasonable estimation using previously-employed techniques.[12, 13, 24] However, as a first approximation we may use literature values for the diffusion coefficient (D_e) in MA lead triiodide films and scale the diffusion length (L_D) according to our measured PL lifetimes (τ) as $L_D = \sqrt{D_e \tau}$. In this way, we can roughly estimate a 200 nm diffusion length for neat triiodide films and over 800 nm for samples that have been treated with chloride. A diffusion length of 200 nm, while longer than estimated previously,[13] is not sufficiently long for the films presented in this work, where a large fraction of the crystals clearly exceed this thickness (Figure 4-11). Moreover, to achieve close to 100% charge collection, the diffusion length must approach 3 times the film thickness.[25] Thus, we can account for our photocurrent losses in samples that have not been prepared with chloride.

4.3   Conclusion

We have demonstrated that the short circuit current of solution-processed planar heterojunction solar cells can be improved via the addition of chloride in the immersion solution, overtaking those exhibited by current state-of-the-art devices. We have shown that planar PbI_2 films can be fully converted within 5 minutes to the $MAPbI_{3-x}Cl_x$ perovskite structure by immersion in a

4.4. Experimental Section

heated solution mixture of MAI and MACl. We find that the addition of chloride critically impacts the lifetime of photoexcited species in the active material, increases light absorption at the bandgap edge and reduces the device series resistance, enabling almost complete sunlight capture in 400 nm thick films. It is worth noting here that the diffusion length of photoexcited species of the neat triiodide perovskite prepared via the deposition-conversion technique is roughly 200 nm; longer than estimated for films deposited via other methods. For this reason, films prepared in this way perform well in comparison to previous reports of solution processed MAPbI$_3$ planar heterojunction devices.[12, 13, 26, 27] This indicates that the photovoltaic properties of the material are highly sensitive to the method of film formation and crystallization.

4.4   Experimental Section

Preparation of the methylammonium salts: methylammonium iodide was prepared following a recipe published earlier.[5] In short, 24 mL of methylamine solution (33 % in ethanol) was diluted with 100 mL of absolute ethanol. To this solution, a 10 mL aqueous solution of hydriodic acid (57 wt%) was added under constant stirring. After a reaction time of one hour at room temperature, the solvents were removed by rotary evaporation. The obtained white solid was washed with dry diethyl ether and finally recrystallized from ethanol.

To prepare the hydrochloride salt of methylamine, the hydriodic acid solution was replaced by 15 mL of concentrated hydrochloric acid (37 % in water). The purification procedure was the same as described above.

Solar cell preparation: Fluorine doped tin oxide (FTO) coated glass sheets (7 $\Omega/\square$, Pilkington) were etched with zinc powder and HCl (2 M) to obtain the required electrode pattern. The sheets were then washed with soap (2% Hellmanex in water), de-ionized water, acetone, and methanol and finally treated under oxygen plasma for 5 minutes to remove the last traces of organic

residues. The substrates were then coated with a sol-gel derived TiO_2 layer, prepared as previously described and calcined at 500 °C in air to achieve full anatase crystallization.[6]

A 27.2 mM HCl solution in 2-propanol (Sigma Aldrich) (typical quantities of 2.53 mL of 2-propanol and 35 µL of 2 M HCl) was slowly added dropwise under vigorous stirring to a 0.43 M titanium isopropoxide solution in 2-propanol (typically 369 µL titanium isopropoxide in 2.53 mL of 2-propanol). The solution looked clear at all times, and was immediately discarded if cloudy.

A ~200 nm layer of lead iodide was deposited via spincoating from a 1 M PbI_2 solution in *N,N*-Dimethylformamide (DMF) at 3000 rpm for 15 s. To achieve optimum performance, it was critical to ensure that both the substrate and precursor solution temperature when starting the spincoater is between 60 and 65 °C. The spincoating was performed dynamically (i.e. the solution was added while the substrate was spinning) with a total 100 µL of solution, without allowing the substrates or solution to cool.

The stock immersion solutions were prepared by dissolving 10 mg/mL methylammonium iodide or methylammonium chloride in dry isopropanol, the latter with heating to 60 °C. For mixing the desired concentrations, these stock solutions were combined in the desired ratio. Before immersion, 40 mL of the solution and the PbI_2 films were heated to 60 °C on a hotplate. The temperature of the solution was monitored during the whole time with a thermometer. After immersion of the films into the solution in a square petri dish with the substrates face up, the solution was left undisturbed for 5 minutes. Once the conversion was finished, the films were washed with clean, anhydrous isopropanol and dried under a nitrogen stream.

After drying, the films were covered with a 400 nm layer of Spiro-OMeTAD (Borun Chemicals, 99.1% purity) "spiro". 96 mg of spiro were dissolved in 1 mL of chlorobenzene and mixed with

4.4. Experimental Section

10 mL 4-*tert*-Butylpyridine (*t*BP) and 30 μL of a 170 mgmL^{-1} bis(trifluoromethane)sulfonimide lithium salt (LiTFSI) solution in acetonitrile. This solution was spincoated at 1500 rpm for 45 seconds. Before evaporating the gold electrodes, Spiro-OMeTAD was allowed to oxidize in air over night at room temperature and 15-20% rel. humidity.

PL sample preparation: For the preparation of the PL samples glass slides were used instead of FTO substrates. The PbI$_2$ deposition and immersion procedure in the MA salt solutions was the same as described above. We note that exposure of the glass slides to oxygen plasma was essential in order to achieve optically smooth films. After drying of the converted films in a nitrogen stream, they were covered with a poly(methyl methacrylate) (PMMA) layer to prevent degradation by ambient moisture. For this purpose, a solution of PMMA (10 mg/mL) was dissolved in 1 mL of chlorobenzene and spincoated at 1000 rpm for 45 seconds.

Characterization details: Solar simulated AM 1.5 sunlight was generated with an ABET class AAB solar simulator calibrated to give 102 mWcm^{-2} using an NREL calibrated KG5 filtered silicon reference cell. The spectral mismatch factor was calculated to be 2%. The JV curves were recorded with a Keithley 2400. The active area of the solar cells was defined with a metal aperture mask of about 0.08 cm^2.

Steady-state absorption spectra were acquired with a Varian Cary 300 UV/Vis spectrophotometer using an integrating sphere. The films were measured in a one-pass configuration, so in order to account for the highly reflective nature of the metal cathode, the optical densities were doubled as a first approximation. The FTO absorption was quantified as previously,[6] where transmittance and reflectance were measured for the glass/FTO/air system in an integrating sphere.

Incident Photon to Charge Carrier Efficiency (IPCE) spectra were obtained using a Fourier transform photocurrent spectrometer, incorporating a Fourier transform spectrometer (Vertex

80v, Bruker), current preamplifier (SR570, Stanford Research Instruments) and custom-built control electronics and software. The spectrometer was configured with a tungsten-halogen light source and CaF_2 beam splitter. Photocurrent was recorded from short-circuited devices following the application of 2 V forward bias. The spectra were calibrated against measurements taken with the same system on a reference silicon photodiode with a known IPCE spectrum. The solar cells and reference diode were masked with a metal aperture to define the active area of ~0.0625 cm^2.

Time-resolved PL measurements were acquired using a time correlated single photon counting (TCSPC) setup (FluoTime 300, PicoQuant GmbH). The samples were photoexcited using a 507 nm laser head (LDH-P-C-510, PicoQuant GmbH) pulsed at 500 kHz, with a pulse duration of 117 ps and fluence of ~300 nJcm^{-2}/pulse. The samples were exposed to the pulsed light source set at 3 μJcm^{-2}/pulse fluence for ~10 minutes prior to measurement to ensure stable sample emission. The PL was collected using a high resolution monochromator and hybrid photomultiplier detector assembly (PMA Hybrid 40, PicoQuant GmbH).

Scanning electron microscopy (SEM) images were obtained using a Hitachi S-4300 microscope.

Energy dispersive X-ray (EDX) spectra were acquired with an EDAX Si(Li) detector. The spectrum shown in Figure S4 was acquired over 32 min at a dwell time of 102.4 μs and 5 eV/channel.

EEL spectra were recorded with a post column filter (Gatan Tridiem 863 P) at a dispersion of 0.2 eV in diffraction mode (camera length 102 mm).

4.5   Literature

[1]   A. Kojima, K. Teshima, Y. Shirai, T. Miyasaka, *J. Am. Chem. Soc.* **2009**, *131*, 6050.

[2]   J. H. Im, C. R. Lee, J. W. Lee, S. W. Park, N. G. Park, *Nanoscale* **2011**, *3*, 4088.

[3]   L. Etgar, P. Gao, Z. S. Xue, Q. Peng, A. K. Chandiran, B. Liu, M. K. Nazeeruddin, M. Gratzel, *J. Am. Chem. Soc.* **2012**, *134*, 17396.

[4]   H. S. Kim, C. R. Lee, J. H. Im, K. B. Lee, T. Moehl, A. Marchioro, S. J. Moon, R. Humphry-Baker, J. H. Yum, J. E. Moser, M. Gratzel, N. G. Park, *Scientific Reports* **2012**, *2*.

[5]   M. M. Lee, J. Teuscher, T. Miyasaka, T. N. Murakami, H. J. Snaith, *Science* **2012**, *338*, 643.

[6]   J. M. Ball, M. M. Lee, A. Hey, H. J. Snaith, *Energy Environ. Sci.* **2013**, *6*, 1739.

[7]   A. Abate, D. J. Hollman, J. Teuscher, S. Pathak, R. Avolio, G. D'Errico, G. Vitiello, S. Fantacci, H. J. Snaith, *J. Am. Chem. Soc.* **2013**, *135*, 13538.

[8]   P. Docampo, J. M. Ball, M. Darwich, G. E. Eperon, H. J. Snaith, *Nat. Commun.* **2013**, *4*, 2761.

[9]   J. Burschka, N. Pellet, S.-J. Moon, R. Humphry-Baker, P. Gao, M. K. Nazeeruddin, M. Gratzel, *Nature* **2013**, *499*, 316.

[10] M. Liu, M. B. Johnston, H. J. Snaith, *Nature* **2013**, *501*, 395.

[11] D. Liu, T. L. Kelly, *Nat. Photon.* **2014**, *8*, 133.

[12] S. D. Stranks, G. E. Eperon, G. Grancini, C. Menelaou, M. J. P. Alcocer, T. Leijtens, L. M. Herz, A. Petrozza, H. J. Snaith, *Science* **2013**, *342*, 341.

[13] G. Xing, N. Mathews, S. Sun, S. S. Lim, Y. M. Lam, M. Grätzel, S. Mhaisalkar, T. C. Sum, *Science* **2013**, *342*, 344.

[14] C. Wehrenfennig, G. E. Eperon, M. B. Johnston, H. J. Snaith, L. M. Herz, *Adv. Mater.* **2013**, *26*, 1584.

[15] S. Colella, E. Mosconi, P. Fedeli, A. Listorti, F. Gazza, F. Orlandi, P. Ferro, T. Besagni, A. Rizzo, G. Calestani, G. Gigli, F. De Angelis, R. Mosca, *Chem. Mater.* **2013**, *25*, 4613.

[16] E. Edri, S. Kirmayer, A. Henning, S. Mukhopadhyay, K. Gartsman, Y. Rosenwaks, G. Hodes, D. Cahen, *Nano Lett.* **2014**, *14*, 1000.

[17] V. Gonzalez-Pedro, E. J. Juarez-Perez, W.-S. Arsyad, E. M. Barea, F. Fabregat-Santiago, I. Mora-Sero, J. Bisquert, *Nano Lett.* **2014**, *14*, 888.

[18]   T. Baikie, Y. Fang, J. M. Kadro, M. Schreyer, F. Wei, S. G. Mhaisalkar, M. Graetzel, T. J. White, *J. Mater. Chem. A* **2013**, *1*, 5628.

[19]   G. E. Eperon, V. M. Burlakov, P. Docampo, A. Goriely, H. J. Snaith, *Adv. Funct. Mater.* **2014**, *24*, 151.

[20]   H. J. Snaith, *Energy Environ. Sci.* **2012**, *5*, 6513.

[21]   T. Ishihara, *J. Lumin.* **1994**, *60*, 269.

[22]   V. D'Innocenzo, G. Grancini, M. J. P. Alcocer, A. R. S. Kandada, S. D. Stranks, M. M. Lee, G. Lanzani, H. J. Snaith, A. Petrozza, *Nat. Commun.* **2014**, DOI: 10.1038/ncomms4586.

[23]   F. Deschler, M. Price, S. Pathak, L. E. Klintberg, D.-D. Jarausch, R. Higler, S. Hüttner, T. Leijtens, S. D. Stranks, H. J. Snaith, M. Atatüre, R. T. Phillips, R. H. Friend, *The Journal of Physical Chemistry Letters* **2014**, 1421.

[24]   P. E. Shaw, A. Ruseckas, I. D. W. Samuel, *Adv. Mater.* **2008**, *20*, 3516.

[25]   P. Docampo, A. Ivaturi, R. Gunning, S. Diefenbach, J. Kirkpatrick, C. M. Palumbiny, V. Sivaram, H. Geaney, L. Schmidt-Mende, M. E. Welland, H. J. Snaith, *J. Mater. Chem. A* **2013**, *1*, 12088.

[26]   S. Sun, T. Salim, N. Mathews, M. Duchamp, C. Boothroyd, G. Xing, T. C. Sum, Y. M. Lam, *Energy Environ. Sci.* **2014**, *7*, 399.

[27]   J. Y. Jeng, Y. F. Chiang, M. H. Lee, S. R. Peng, T. F. Guo, P. Chen, T. C. Wen, *Adv. Mater.* **2013**, *25*, 3727.

5 Influence of the Orientation of Methylammonium Lead Iodide Perovskite Crystals on Solar Cell Performance

This chapter describes the influence of different preparation parameters in the before mentioned synthesis route and is based on the following publication:

Pablo Docampo*, Fabian C Hanusch*, Nadja Giesbrecht, Philipp Angloher, Alesja Ivanova, Thomas Bein*, *APL Materials* **2014**, *2*, 081508.

*These authors contributed equally to this work

5.1 Introduction

Perovskite solar cells are emerging as promising candidates for thin film photovoltaics with power conversion efficiencies already approaching other established inorganic thin film technologies. These devices can be processed easily from solution, do not require high sintering steps and can be prepared on flexible substrates,[1-3] while already achieving high photovoltaic performance. To date, values of up to 16 % were reached via different fabrication techniques,[4-8] and achieving higher performances of up to 20% could be feasible in the short term.[9]

Methylammonium lead iodide (MAPbI$_3$) perovskites were initially introduced to photovoltaics in iodine/iodide electrolyte based sensitized solar cells by Miyasaka and coworkers, with a starting efficiency of 5%.[10] However, these devices were highly unstable due to the degradation of the perovskite film by the electrolyte. It was not until the introduction of meso-superstructured perovskite solar cells by Snaith and coworkers that performances of over 12 % were achieved with the solid-state hole transporter 2,2',7,7'-tetrakis-(N,N-di-p-methoxyphenylamine)9,9'-spirobifluorene (Spiro-OMeTAD).[7] Hybrid perovskite solar cells

5.1. Introduction

can now achieve high power conversion efficiencies of over 15% when processed as thin film photovoltaic devices and over 16% in a sensitized photoanode configuration.[4, 5, 8, 11] The former architecture is particularly attractive for flexible and tandem applications, as they are compatible with low temperature processing (<150 °C), compared to employing a mesoporous TiO$_2$ photoanode which requires a heating step at 500 °C.

The fabrication protocol for state-of-the-art planar heterojunction devices is based on a sequential deposition/conversion technique, first introduced by Liang and coworkers[12] and later applied to perovskite solar cells by Burschka and coworkers.[4] Firstly, a film of PbI2 is deposited either via evaporation or solution processing onto a metal oxide non-porous layer. The substrate is then immersed in a solution containing an alkyl ammonium salt where the conversion into the perovskite phase takes place. Following this approach, Liu and coworkers obtained perovskite crystals ranging in size from tens to hundreds of nanometers and complete surface area coverage. In all previous work employing this technique, the neat MAPbI$_3$ perovskite has been used. In planar configuration devices, this choice limits the maximum possible short circuit currents, as the charge diffusion lengths have been determined to be around 100 nm.[13, 14] We have recently extended this technique to include chloride in the perovskite film formation,[15] thus achieving higher short circuit photocurrents due to the longer charge diffusion lengths present in this system approaching the micron scale.[13]

Here, we further study the deposition/conversion technique for planar heterojunction solar cells. We show that it is critical to achieve full perovskite conversion in order to achieve maximum performance and high short circuit currents. We also show that the perovskite crystal orientation can be modified by the temperature of the immersion solution, and find that a high degree of oriented crystals is necessary for efficient operation.

5.2 Results and Discussion

The device architecture for planar heterojunction perovskite solar cells used in this study is composed of FTO/TiO$_2$/MAPbI$_3$/Spiro-OMeTAD/Gold, as shown in the schematic in Figure 5-1. The TiO$_2$ layer is non-porous and acts as the electron selective contact, while spiro-OMeTAD is used as the hole collecting contact. The perovskite film was deposited via a two-step deposition/conversion process, where a layer of PbI$_2$ was first deposited via spin-coating, followed by conversion to the perovskite phase in a second step via immersion in a solution of methylammonium iodide and chloride in isopropanol at varying temperatures.[15]
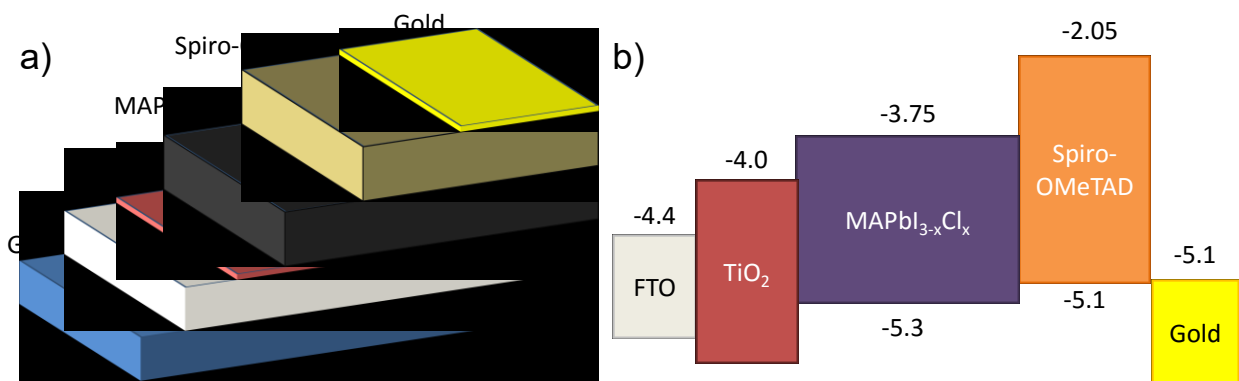

Figure 5-1: a) Schematic of the device architecture. b) Energy level diagram with respect to vacuum for all the layers comprising the solar cell (numbers in eV).

In order to monitor the conversion of the PbI$_2$ phase into the perovskite phase, XRD measurements for increasing immersion times were performed (Figure 5-2). The peak observed at 12.65 degrees 2θ corresponds to the (001) reflection of PbI$_2$ and the peak on 14.2 degrees corresponds to the first reflection of the perovskite phase. By following the evolution of these two peaks we could determine at which point full conversion was achieved, which depended both on temperature and lead iodide film thickness.

5.2. Results and Discussion
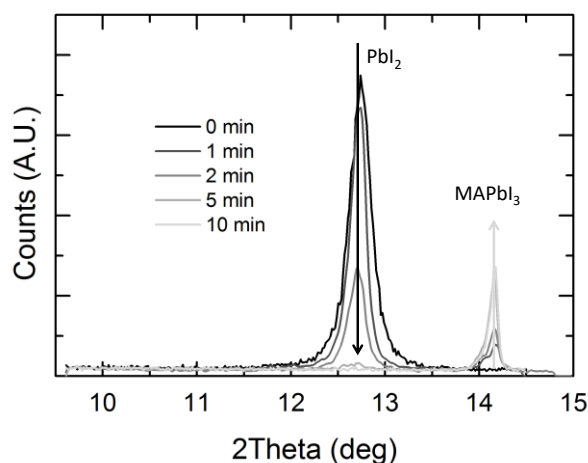
Figure 5-2: XRD measurements for PbI₂ films immersed for a range of times in the perovskite conversion solution.

The evolution of the film with time after this point can be seen in the SEM images of Figure 5-3, showing the increase of the crystal size with longer immersion times. However, gaps start appearing in the films at longer immersion times. Full area coverage is essential for optimum device performance,[1, 16] therefore, the conversion was stopped when no crystalline lead iodide was left in the film. The shortest time with no residual lead iodide peak at approximately 12.65° was chosen for further experiments and is summarized in Table 5-1 for a range of lead iodide thicknesses and immersion temperatures.
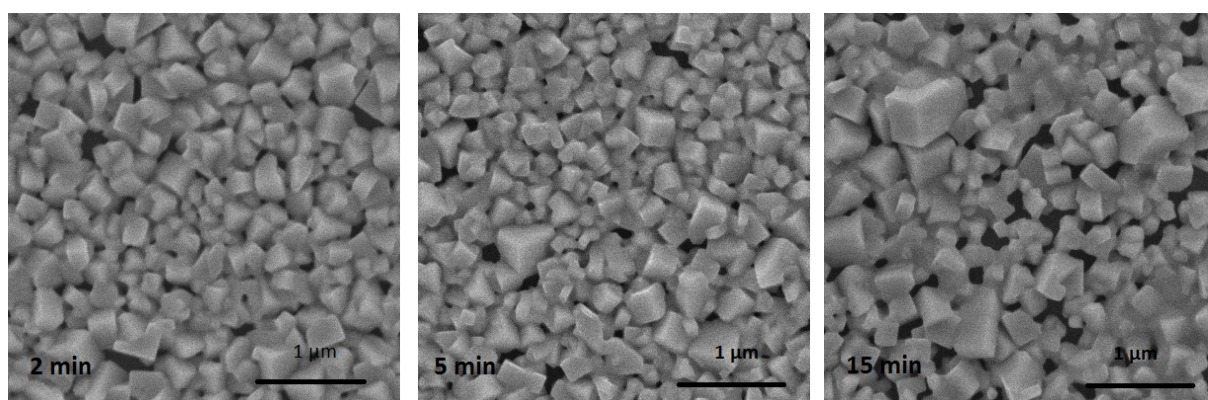

Figure 5-3: SEM image of the top view of MAPbI₃-perovskite films on glass with an initial 90 nm PbI₂ layer thickness and 60 °C immersion temperature for a range of immersion times: a) 2 min, b) 5 min and c) 15min.

Table 5-1: Immersion times at different temperatures for the prepared PbI$_2$ layer thicknesses required to achieve full perovskite conversion.

PbI$_2$-layer thickness	Temperature/Time (min)			
	30 °C	40 °C	50 °C	60 °C
90 nm	30	15	8	5
230 nm	35	20	12	8
280 nm	40	25	15	10
330 nm	43	30	20	12

In Figure 5-4 we show the photovoltaic performance of devices that have been fabricated from lead iodide films immersed for a range of times in the perovskite conversion solution. We find that full conversion of the lead iodide film is essential for good device performance. Films which are not fully converted do not sustain the current at short circuit conditions, even when scanning from open circuit to short circuit. This anomalous behavior has been observed previously for this family of materials and is currently under intensive investigation by several research groups.[17-21] As the conversion occurs from the top of the lead iodide layer downwards, the methylammonium iodide cation requires a certain amount of time at a given temperature to diffuse through the whole structure. It is likely that the residual lead iodide layer in films that are not fully converted inhibits charge transfer from the perovskite to the TiO$_2$ underlayer, as electrons are required to travel upwards in energy to cross this interface.
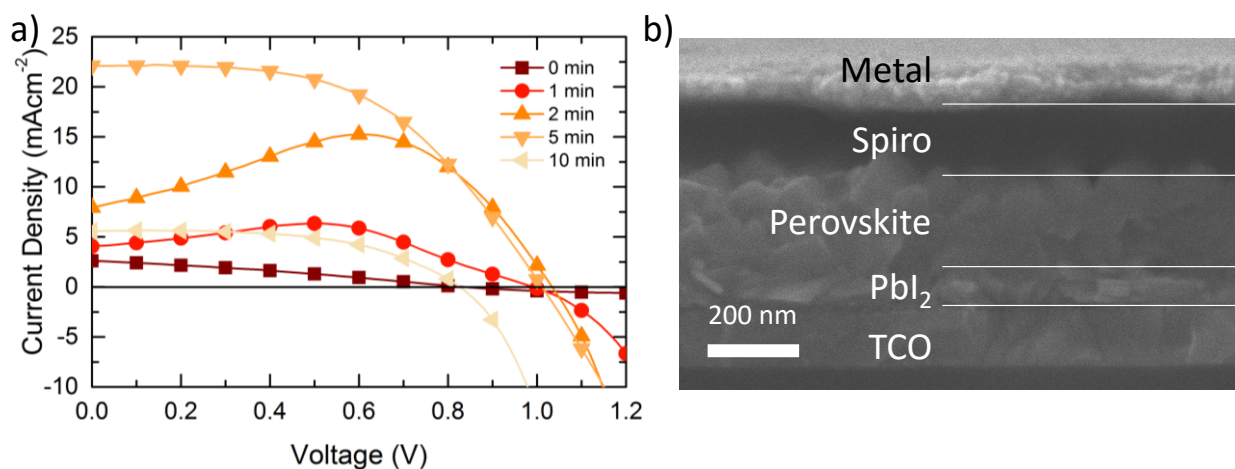

Figure 5-4: a) JV curves measured under AM 1.5 solar irradiance and 100 mWcm^{-2} equivalent light intensity conditions for the best performing MA lead iodide perovskite devices for a range of immersion times. b) SEM cross section of a device which has not been fully converted into the perovskite phase.

5.2. Results and Discussion

We note here that fully converted films, while showing standard JV curve shapes for solar cells when scanned with 50 mV steps and 100 ms delay times, show a different behavior when scanning from past open circuit to short circuit than on the reverse scan. We show these results in Figure 5-5, where "hysteresis" can be observed at these scan rates. When these solar cells are held at short circuit conditions for extended periods of time, the short circuit current drops to less than half its value in under half a minute. Solar cells fabricated from perovskite films that are not fully converted to $MAPbI_3$ are an extreme example of this behavior, where the current drops even while scanning the JV curve as shown in Figure 5-4. This may be due to a residual interfacial lead iodide layer between TiO_2 and the perovskite crystals, which could still be present even when the crystalline lead iodide signal disappears from the XRD measurements. Longer immersion times, however, did not solve this issue, where devices immersed for 10 min still showed hysteretic behavior and far lower photovoltaic performance. It is worth noting here that this anomalous hysteretic effect, to a lesser extent, is also present when the same sequential deposition/conversion technique is applied to lead iodide layers within a mesoporous TiO_2 film.[18]
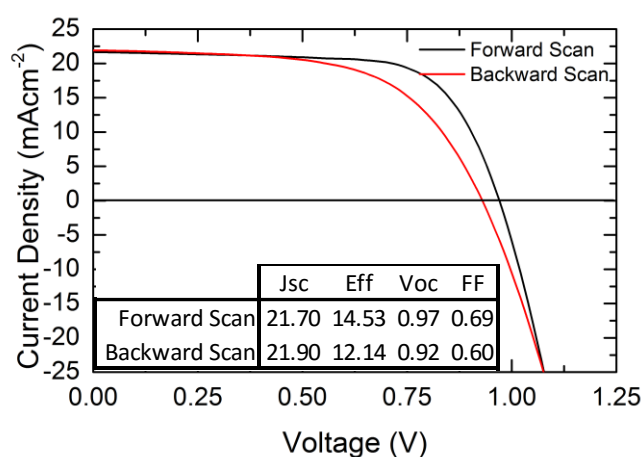

Figure 5-5: JV curves measured under AM 1.5 solar irradiance. Backward scan refers to the device being measured from short circuit to past open circuit, while forward scan refers to the device measured from past open circuit to short circuit. The inset summarizes the photovoltaic performance parameters. The JV curves were scanned with a 50 mV step and 100 ms delay.

Other parameters which affect film formation, both initial PbI_2 layer thickness and conversion solution temperature, were also studied. The highest power conversion efficiencies of up to 14.3% were achieved with lead iodide layer thicknesses between 230 and 280 nm and an immersion temperature of 60 °C, see Table 5-2 for details.

Table 5-2: Summary of the lead iodide layer thicknesses achieved by spincoating from solutions and device substrates heated to different temperatures and spin-coating speeds.

Temperature	Spin-coating speed	
	2000 rpm	3000 rpm
	1 M PbI_2 solution in DMF	
50 °C	~330 nm	~230 nm
60 °C		~280 nm
	0.75 M PbI_2 solution in DMF	
50°C		~90 nm

A summary of photovoltaic parameters for the best performing devices can be found in Table 5-3. Interestingly, it was found that the immersion temperature did not significantly influence the average perovskite crystal size when the conversion was stopped at the minimum time possible after full conversion of the lead iodide layer (See Figure 5-6).
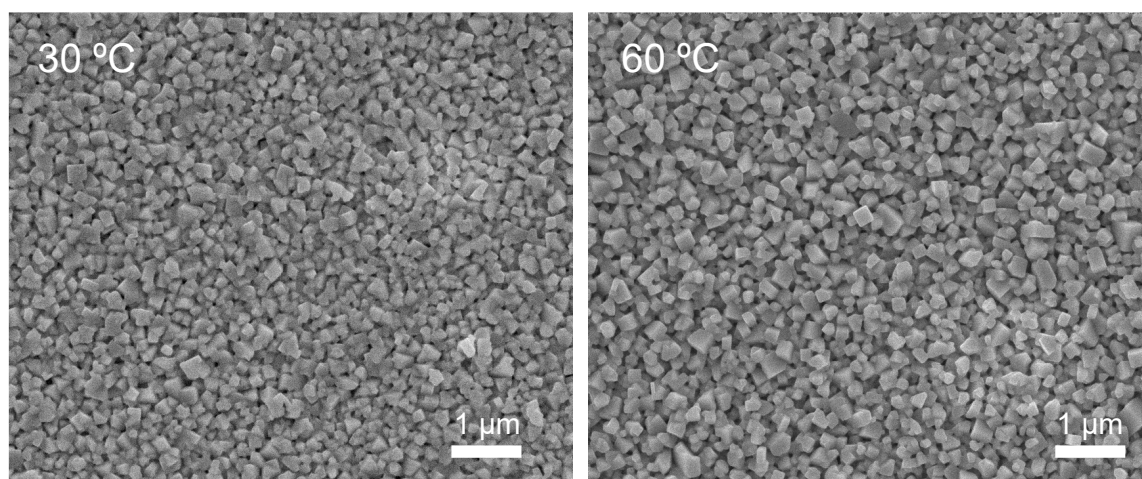

Figure 5-6: SEM top view images of perovskite films converted at 30 °C (left) and 60 °C (right).

This may be due to the perovskite/TiO_2 layer interface interaction. In a previous study, Eperon *et al.* have shown that the interaction between the TiO_2 layer and the perovskite film determines

5.2. Results and Discussion

the film formation properties, i.e. surface coverage and crystal size.[16] As the films in this work all employed the same TiO_2 layer, this may be the reason why perovskite crystal size is independent of the immersion temperature. We note here that when the samples are prepared on plain glass, big differences between samples converted at 30 °C and at 60 °C appear, where the crystal size more than doubles at the higher temperature.

Table 5-3: Summary of the photovoltaic parameters for the best cells at each PbI₂ thickness/conversion bath temperature.

PbI₂-layer thickness	J_{SC} (mAcm^{-2})	V_{OC} (mV)	Fill factor	PCE (%)
30 °C				
90 nm	0.9	858	0.72	0.5
230 nm	9.0	905	0.60	4.9
280 nm	7.4	906	0.60	4.0
330 nm	11.7	897	0.56	5.8
50 °C				
90 nm	4.3	679	0.28	0.8
230 nm	8.5	732	0.19	1.2
280 nm	17.0	1030	0.60	10.5
330 nm	2.4	866	0.50	1.0
60 °C				
90 nm	13.6	925	0.48	6.1
230 nm	19.9	1050	0.59	12.3
280 nm	19.9	990	0.70	13.9
330 nm	11.7	897	0.56	5.8

The photovoltaic performance of the best devices prepared from perovskite films converted at 30 ºC and 60 ºC is shown in Figure 5-7. Both devices exhibited similar fill factors of around 65%, and similar open circuit voltages. However, devices fabricated at lower temperatures exhibit much lower short circuit currents than those fabricated at higher temperatures: at 30 °C, the short circuit current approaches 19 mAcm^{-2} while at 60 °C, this value exceeds 22 mAcm^{-2}. Correspondingly, the device efficiency for 60 °C is the highest for this set of experiments, standing at 14.3%.

|	J_{sc}	V_{oc}	FF	η	R_s
30 °C	18.8	0.98	0.67	12.4	7.5
60 °C	22.3	0.96	0.67	14.3	6.7
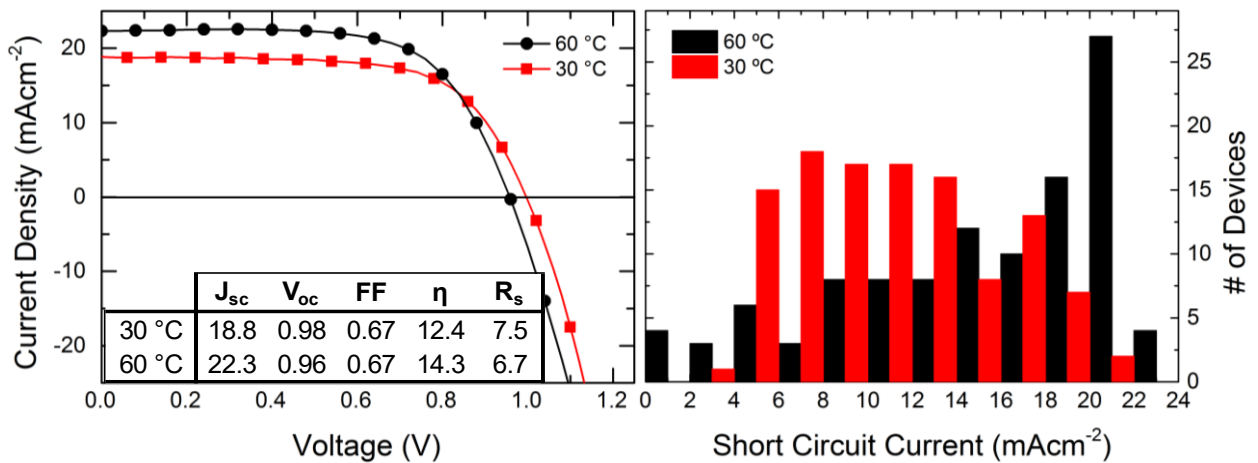
Figure 5-7: (left) JV curves measured under AM 1.5 solar irradiance and 100 mWcm^{-2} equivalent light intensity conditions for the best performing MA lead halide perovskite devices for 30 ºC (red squares) and 60 ºC (black circles) immersion bath temperatures. The inset summarizes the photovoltaic parameters: short circuit current (J_{sc}, mA cm^{-2}), open circuit voltage (V_{oc}, V), fill factor (*FF*, %), power conversion efficiency (η, %), and series resistance (R_s, Ω cm^2). (right) Histogram showing the short circuit current distribution of a series of over 100 devices fabricated from perovskite films converted at 30 ºC (red) and at 60 ºC (black). The devices were fabricated in three separate batches prepared several days apart.

Additionally we show a histogram depicting the distribution of short circuit currents for a set of over 100 devices on the right of Figure 5-7. We can clearly observe that devices fabricated at lower temperatures have a much larger spread in the final short circuit current, with a mean value of 11-12 mAcm^{-2}. When the perovskite films are converted at 60 ºC, however, the short circuit currents are far more reproducible, where more than a third of the fabricated devices exhibit values of over 18 mAcm^{-2}. To further examine the differences in short circuit current, the light absorption characteristics of the films were quantified as shown in Figure 5-8.
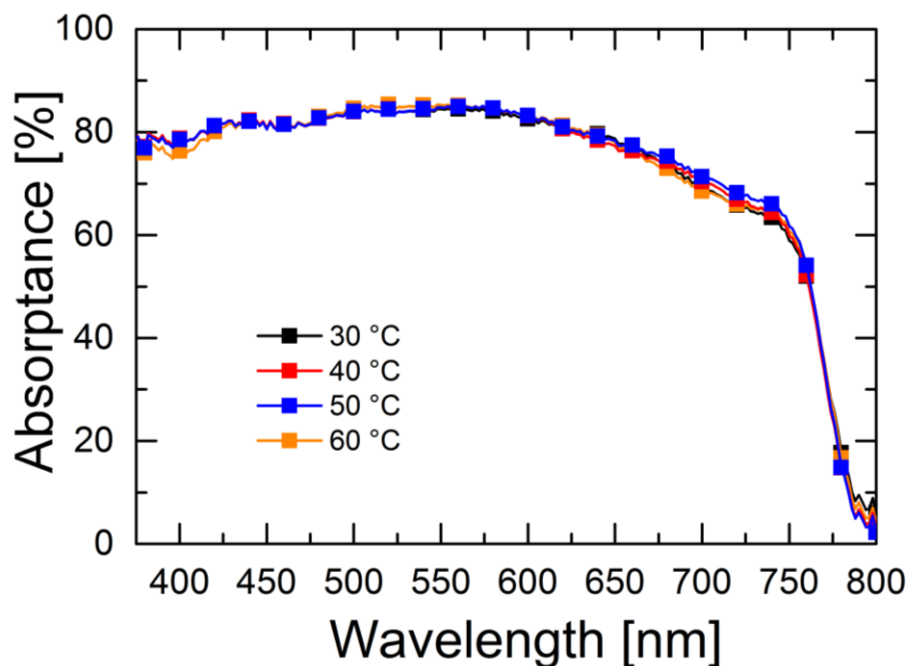
Figure 5-8: UV-Vis absorption spectrum in an integrating sphere of the perovskite films prior to deposition of the hole transporter and gold cathode.

We observed no difference in the absorption for any of the fabricated perovskite films. This should be expected as the films are fabricated from the same thickness of PbI_2, and neither the crystal size nor the surface coverage changes with different immersion temperatures.

To obtain a better understanding of the influence of different immersion temperatures on the perovskite film growth, XRD measurements were performed as shown in Figure 5-9. In all cases the perovskite structure is tetragonal in the I4/mcm space group, with no apparent difference in crystal size or crystallinity.
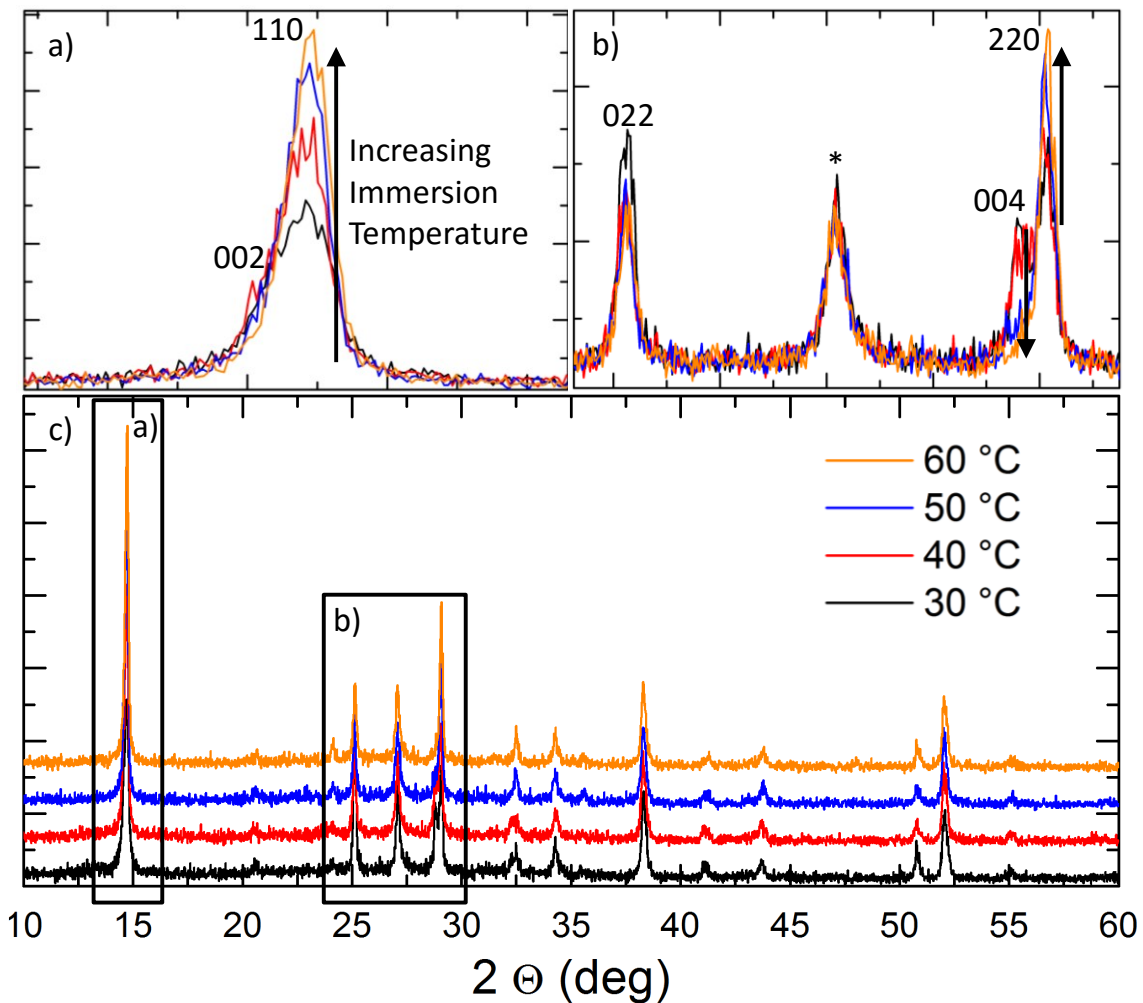
Figure 5-9: XRD characterization of the perovskite films obtained from a range of immersion solution temperatures, where a) is a zoomed-in image of the (002) and (110) reflections at around 15 º2θ, b) is the zoomed-in image of the (202), (004), and (220) reflections between 25 and 30 º and c) is the whole pattern. The symbol * in b) denotes the first FTO peak.

However, with increasing immersion solution temperature, a higher proportion of oriented crystals was found: the intensity of the (110) and (220) reflections increases with increasing temperature, while the (004) reflection completely disappears at higher temperatures and the other intensities remain the same. This leads us to conclude that at higher immersion solution temperatures, the crystals are preferentially oriented with the long axis parallel to the substrate. It is curious to note here that high performing perovskite solar cells prepared from spincoating a precursor mixture of MAI and PbCl$_2$ with a subsequent heat treatment also result in highly oriented crystals with the long axis preferentially oriented parallel to the substrate, where

usually only the (110), (220), (330), etc. reflections are visible.[7] Anisotropic electronic properties of the perovskite crystals may thus be the reason for the observed difference in photovoltaic performance.

Further evidence to support this hypothesis is provided in a recent study by Saliba *et al.*, where flash annealing at 130 ºC of spin-coated perovskite precursor mixtures was employed.[22] The resulting perovskite films exhibited larger and more oriented domains than films processed at 100ºC for longer periods of time, and ~10% higher short circuit currents than the standard counterparts, while maintaining similar fill factors and open circuit voltages. While in Saliba *et al*'s study the increase in short circuit current was correlated to the formation of larger crystal domain sizes, this is not the case in the study presented here. The fact that we have obtained such a similar result in this very different system points towards crystal orientation as a key parameter determining the device short circuit current. Whether this is the result of anisotropic transport or specific interactions between the different charge extraction layers and the perovskite crystal planes is not clear at this point and is currently under investigation. Regardless of the specific mechanism, however, it is clear that controlling the deposition parameters to achieve highly oriented crystal domains is an important route towards the further development of this family of materials.

5.3   Conclusions

In conclusion, the performance of planar heterojunction perovskite solar cells prepared by a deposition/conversion technique was studied by varying the conversion conditions. Our results show that the final perovskite crystal size is invariant with immersion temperature when the films are prepared on similar device substrates. We postulate here that the morphology of the perovskite film is determined to a large extent by the substrate/perovskite interaction. This is

similar to findings for precursor mixture perovskite deposition.[16] In the case of lead iodide films that have not been fully converted into the methylammonium lead iodide phase, the resulting devices do not sustain high currents at short circuit conditions, even when scanned from open circuit to short circuit. Additionally, we have found that the temperature for the conversion process is an important factor for device performance. With increasing immersion temperatures for the perovskite conversion, we observe higher short circuit currents in the resulting solar cells as well as a much narrower performance spread when a large batch of devices is considered. The highest power conversion efficiency of 14.3 % is found for devices prepared from perovskite films immersed at 60 °C. The temperature of the conversion bath greatly influences the orientation of the resulting perovskite crystals, which results in the alignment of the long crystalline axis with the TiO_2-covered FTO substrate, thus orienting the (110) planes perpendicular to the substrate. Our results illustrate the great importance of the solution deposition parameters during the formation of methylammonium lead iodide thin films. We suggest that achieving highly oriented crystal domains is a key factor for the further development of this promising family of materials for photovoltaic applications.

5.4 Experimental Section

Substrate preparation

Fluorine-doped tin oxide (FTO) coated glass (Pilkington, 7 Ω $\square^{-1}$) was patterned by etching with Zn metal powder and 3 M HCl. Substrates were then cleaned sequentially in deionized water, 2% hallmanex detergent in water, acetone and ethanol, dried with clean dry air between solvents and finally treated for 5 minutes under an oxygen plasma. A TiO_x layer was deposited over the substrates by spincoating the precursor solution (described below) at 2000 rpm for 45 s. After spin-coating, the substrates were dried at 150 °C for 5 minutes on a hotplate and

then sintered at 500 °C for 60 minutes in a furnace to achieve full crystallization into the anatase phase. The lead iodide (99 %, Sigma-Aldrich) layer was deposited via spincoating from a range of solution concentrations in anhydrous N,N-dimethylformamide (DMF) at different solution and substrate temperatures, at a final spinning speed to achieve thicknesses between ~90 nm and ~330 nm. The deposition parameters and associated thicknesses are summarized in **Table 1**. For all variations, 100 µL of the PbI_2 solution in DMF was first dispersed on the substrate and spin-coated for 10 s, and then placed immediately on a hotplate at the appropriate temperature without allowing the films to fully dry. Heating of the substrates to 50-60 ºC on a hotplate immediately before spincoating was found essential to achieve visually smooth films.

Electron extraction layer solution

A 0.013 M HCl solution in 2-propanol (IPA) (2.53 mL of IPA (Sigma-Aldrich) and 35 µL of 2 M HCl (Sigma-Aldrich)) was slowly added dropwise under rigorous stirring to a 0.23 M titanium isopropoxide solution in IPA (369 µL titanium isopropoxide in 2.53 mL IPA). The solution looked clear at all times, and was immediately discarded if cloudy.

Conversion procedure

To fully convert the lead iodide films into the perovskite phase, immersion solutions including methylammonium halide precursors in anhydrous IPA were used at different temperatures. Typically 40 mL of a 9.5 mg/mL of MAI and 0.5 mg/mL methylammonium chloride (MACl) mixture in IPA was used for a batch of 64 devices. The reaction vessel was a square petri dish with a lid that was not completely closed to allow monitoring of the solution temperature via a thermometer. The solution was never allowed to overheat and was maintained within 2 °C of the intended temperature. To fully convert the lead iodide films into the perovskite phase, the immersion time was tuned according to the solution temperature. After immersion, the samples were rinsed in IPA and dried quickly and evenly with a strong blast of dry air or nitrogen.

Hole-transporting layer

The hole-transporting layer was deposited by spin-coating 75 µL of a 75 mg/mL 2,2`,7,7`-tetrakis-(N,N-di-p-methoxyphenylamine)9,9`-spirobiflourene (spiro-OMeTAD) solution in chlorobenzene (anhydrous, Sigma-Aldrich), with 30 µL per 1 mL of the spiro solution of a 170 mg/mL solution of lithium bis(triflouromethanesulfonyl)imide in acetonitrile, and additionally 10 µL per 1 mL of the spiro solution of 4-tertbutylpyridine. The solution was dynamically spin-coated at 1000 rpm for 45 s with a second step at 2000 rpm for 3 s to remove the excess solution from the corners of the substrate. The substrates were left overnight in a desiccator in air to allow the oxidation of spiro-OMeTAD.[23] To complete the devices, 25 nm thick gold electrodes were thermally evaporated under high vacuum conditions ($<10^{-6}$ mbar) through a metal aperture. The final device area was 0.0825 cm^2.

X-Ray Diffraction

To obtain the XRD patterns, a Bruker D8 discover X-ray diffractometer was used. The perovskite films were deposited as described above with a lead iodide layer thickness of 230 nm on a non-porous TiO_2- and FTO-coated glass. After immersion of the PbI_2 films in the conversion solution, the films were coated with a 10 mg/mL solution of PMMA in anhydrous chlorobenzene via spin-coating at 1000 rpm for 45 s and a second step at 2000 rpm for 3 s.

UV-Vis-Spectroscopy

The samples used for X-ray diffraction were also characterized with UV-vis-spectroscopy using a Perkin Elmer UV Vis/NIR Lambda 1050 spectrophotometer in an integrating sphere.

SEM Images

5.4. Experimental Section

A scanning electron microscope (JSM-6500F) was used to acquire SEM images. Standard device substrates, i.e. TiO_2- and FTO-coated glass, were coated with the perovskite layer as described above, and then fixed with silver paint on an aluminum holder. The silver paint was allowed to dry for 3 hours in the desiccator. The samples were prepared 3 to 18 hours before the measurement and were always stored in a desiccator with <20 rel% humidity to avoid decomposition of the moisture sensitive material.

Device Characterization

Photovoltaic device performance was measured in ambient air under illumination from a AM1.5G solar simulator, which was calibrated to 100 mW/cm² with a Fraunhofer ISE certified silicon cell. JV curves were measured at a 0.5 Vs^{-1} scan rate from past open circuit to short circuit at least 24 h after device fabrication to allow oxygen doping of the hole transporter.[23]

5.5 Literature

[1] P. Docampo, J. M. Ball, M. Darwich, G. E. Eperon, H. J. Snaith, *Nat. Commun.* **2013**, *4*, 2761.

[2] J. You, Z. Hong, Y. Yang, Q. Chen, M. Cai, T.-B. Song, C.-C. Chen, S. Lu, Y. Liu, H. Zhou, Y. Yang, *ACS Nano* **2014**, *8*, 1674.

[3] Y.-F. Chiang, J.-Y. Jeng, M.-H. Lee, S.-R. Peng, P. Chen, T.-F. Guo, T.-C. Wen, Y.-J. Hsu, C.-M. Hsu, *Phys. Chem. Chem. Phys.* **2014**, *16*, 6033.

[4] J. Burschka, N. Pellet, S.-J. Moon, R. Humphry-Baker, P. Gao, M. K. Nazeeruddin, M. Gratzel, *Nature* **2013**, *499*, 316.

[5] M. Liu, M. B. Johnston, H. J. Snaith, *Nature* **2013**, *501*, 395.

[6] J. M. Ball, M. M. Lee, A. Hey, H. J. Snaith, *Energy Environ. Sci.* **2013**, *6*, 1739.

[7] H. S. Kim, C. R. Lee, J. H. Im, K. B. Lee, T. Moehl, A. Marchioro, S. J. Moon, R. Humphry-Baker, J. H. Yum, J. E. Moser, M. Gratzel, N. G. Park, *Scientific Reports* **2012**, *2*.

[8] G. Xing, N. Mathews, S. S. Lim, N. Yantara, X. Liu, D. Sabba, M. Grätzel, S. Mhaisalkar, T. C. Sum, *Nat. Mater.* **2014**, *13*, 476.

[9] N.-G. Park, *J. Phys. Chem. Lett.* **2013**, *4*, 2423.

[10] A. Kojima, K. Teshima, Y. Shirai, T. Miyasaka, *J. Am. Chem. Soc.* **2009**, *131*, 6050.

[11] N. J. Jeon, J. Lee, J. H. Noh, M. K. Nazeeruddin, M. Grätzel, S. I. Seok, *J. Am. Chem. Soc.* **2013**, *135*, 19087.

[12] K. Liang, D. B. Mitzi, M. T. Prikas, *Chem. Mater.* **1998**, *10*, 403.

[13] S. D. Stranks, G. E. Eperon, G. Grancini, C. Menelaou, M. J. P. Alcocer, T. Leijtens, L. M. Herz, A. Petrozza, H. J. Snaith, *Science* **2013**, *342*, 341.

[14] G. Xing, N. Mathews, S. Sun, S. S. Lim, Y. M. Lam, M. Grätzel, S. Mhaisalkar, T. C. Sum, *Science* **2013**, *342*, 344.

[15] P. Docampo, F. Hanusch, S. D. Stranks, M. Döblinger, J. M. Feckl, M. Ehrensperger, N. Minar, M. B. Johnston, H. J. Snaith, T. Bein, *Adv. Energy Mater.* **2014**, aenm.201400355.

[16] G. E. Eperon, V. M. Burlakov, P. Docampo, A. Goriely, H. J. Snaith, *Adv. Funct. Mater.* **2014**, *24*, 151.

[17] H. J. Snaith, A. Abate, J. M. Ball, G. E. Eperon, T. Leijtens, N. K. Noel, S. D. Stranks, J. T.-W. Wang, K. Wojciechowski, W. Zhang, *J. Phys. Chem. Lett.* **2014**, 1511.

[18]   A. Dualeh, T. Moehl, N. Tétreault, J. Teuscher, P. Gao, M. K. Nazeeruddin, M. Grätzel, *ACS Nano* **2013**, *8*, 362.

[19]   J. M. Frost, K. T. Butler, F. Brivio, C. H. Hendon, M. van Schilfgaarde, A. Walsh, *Nano Lett.* **2014**, *14*, 2584.

[20]   Y. Zhao, K. Zhu, *J. Phys. Chem. C* **2014**, *118*, 9412.

[21]   A. Yella, L.-P. Heiniger, P. Gao, M. K. Nazeeruddin, M. Grätzel, *Nano Lett.* **2014**, *14*, 2591.

[22]   M. Saliba, K. W. Tan, H. Sai, D. T. Moore, T. Scott, W. Zhang, L. A. Estroff, U. Wiesner, H. J. Snaith, *J. Phys. Chem. C* **2014**.

[23]   A. Abate, T. Leijtens, S. Pathak, J. Teuscher, R. Avolio, M. E. Errico, J. Kirkpatrik, J. M. Ball, P. Docampo, I. McPherson, H. J. Snaith, *Phys. Chem. Chem. Phys.* **2013**, *15*, 2572.

6 Photopolymerized Fullerene C_{60} as Electron Selective Contact for Perovskite Solar Cells

6.1 Introduction

Ever since the discovery of the spherical C_{60} molecule fullerene by Kroto and even more after the discovery of a multi-gram synthesis route, it has drawn much attention to its unique chemical and electrical properties.[1, 2] It was early noticed that the electronic band structure of this molecule resembles that of a semiconductor and that it is therefore a suitable material for electronic applications, such as transistors and solar cells.[3] For example, fullerenes are of great interest in solar cell research, and the fullerene chemistry has been intensively studied to optimize its solubility and conductivity properties to work well in organic photovoltaics. [4]

Apart from organic solar cells, fullerene chemistry has inspired polymer chemists to prepare cross-linked structures that exhibit the typical fullerene properties. A most interesting class among these polymers is that of all-C_{60} polymers, since they consist exclusively of fullerene and do not need any linking molecules.[5, 6]

All-fullerene polymers have been prepared with different synthetic approaches. Regardless of where the activation energy for the reaction comes from – be it high temperature, pressure or direct activation with light – the reaction always follows the same 2+2 cyclo-addition pathway.[5, 7-10]

Lately, the fascinating properties of C_{60} and its derivatives have been combined with another type of material that has inspired a burst of interesting research – the class of organic-inorganic metal halide perovskites. The most widely used methylammonium lead triiodide ($MAPbI_3$) and its close relative formamidinium lead triiodide ($FAPbI_3$) have recently achieved power

6.1. Introduction

conversion efficiencies of around 20 %, [11, 12] and are therefore becoming strong competitors for already established thin film solar technologies like polycrystalline silicon or GaAs.

Although the perovskite solar cells themselves are already very efficient, the solar energy utilization could be even higher by teaming them up with conventional thin film solar cell technologies in a tandem configuration.[13, 14] To be employed in this type of solar cell, however, the processing temperatures of the perovskite cell need to be below the degradation temperature of the bottom cell. This renders unusable crystalline TiO_2 blocking layers, which have to be sintered at 500 °C. Instead, an n-type material processible at low temperatures and ideally from solution is desirable to prepare perovskite solar cells in a tandem configuration.

Recently it has been demonstrated that a layer of fullerene C_{60} molecules can work as efficient n-type blocking layer for perovskite solar cells.[15] To achieve the high efficiencies reported, it was necessary to apply a two-step vapor deposition method, which is quite demanding in both time and energy consumption. This route was necessary to avoid dissolution of the fullerene layer upon solvent-based deposition of the sequential solar cell layers.

Here we present the utilization of a photochemical crosslinking reaction to stabilize the fullerene layer for the preparation of the photoactive perovskite layer via sequential solution deposition. Furthermore, we investigate the influence of the photopolymerization on the HOMO and LUMO energy levels of the material with in-situ measurements. These energy levels have a strong influence on the obtainable open-circuit voltage and therefore the efficiency of the solar cells. We prepared cells employing both polymerized and unpolymerized fullerene contact layers and compare the photovoltaic properties for the different samples.

We managed to prepare solution processed TiO_2-free perovskite solar cells employing a fullerene C_{60} n-type contact layer with high power conversion efficiencies approaching 10 %.

6.2   Results and discussion

To achieve highly efficient solar cells, the energy levels of the active material and the electron and hole selective layer need to be well matched to ensure facile charge transport through the whole solar cell stack.[16-18] It is known that the polymerization of fullerene molecules affects the electronic structure and is thus a means to adjust and fine-tune the energy levels according to the used photoactive material.[19]

To study the effect of photo-polymerization on the electronic structure of fullerene, thin films of C$_{60}$ were prepared on glassy carbon electrodes. These films were characterized according to their energy levels by means of cyclic voltammetry. For the measurement they were immersed in a 0.1 M solution of Bu$_4$NBF$_4$ in acetonitrile serving as electrolyte[20] and in-situ polymerized by illumination with a 365 nm high power LED. The schematic setup is depicted in Figure 1 a. The polymerization follows a 2+2 cyclo addition depicted in Figure 6-1 b.
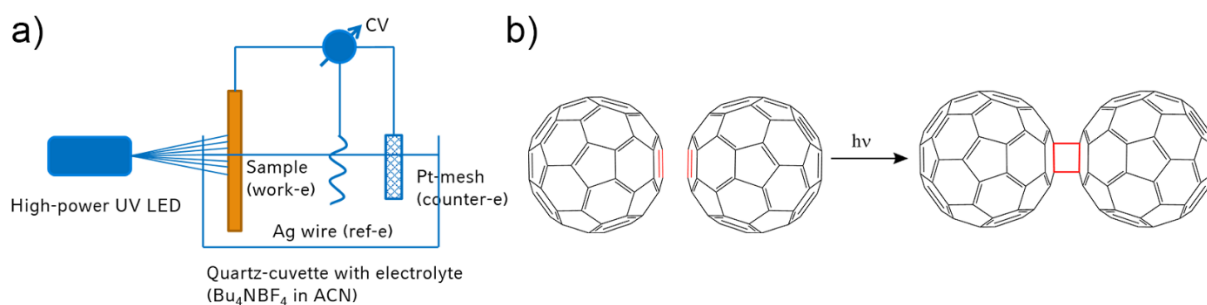

Figure 6-1: Schematic set-up for the in-situ polymerization and CV measurements (a) and fullerene dimerization mechanism via 2+2 cyclo-addition (b)

The sample was illuminated for 2 minutes and then a CV measurement between -1.5 and 0.75 V vs. Ag/AgCl was performed. This procedure was repeated for 8 hours. The resulting curves for certain times of polymerization are depicted in Figure 6-2. It is apparent that the energy of the lowest unoccupied molecular orbital (LUMO) is strongly influenced by the illumination time, i.e. the degree of polymerization. For fullerene C$_{60}$ the polymerization is finished after 120

minutes, as judged from the constant reduction potential of about -0.9 V. This corresponds to a decrease in the reduction potential of about 250 mV compared to the initial value of -0.65 V. The obtained LUMO potentials were determined as the mid-peak potential, i.e. the average of the reduction and re-oxidation potential.[21] It is worth noting that the LUMO energy measured here differs by about 0.1 V from other reported values. This is most likely due to effects caused by the solvent and the supporting electrolyte.[22]
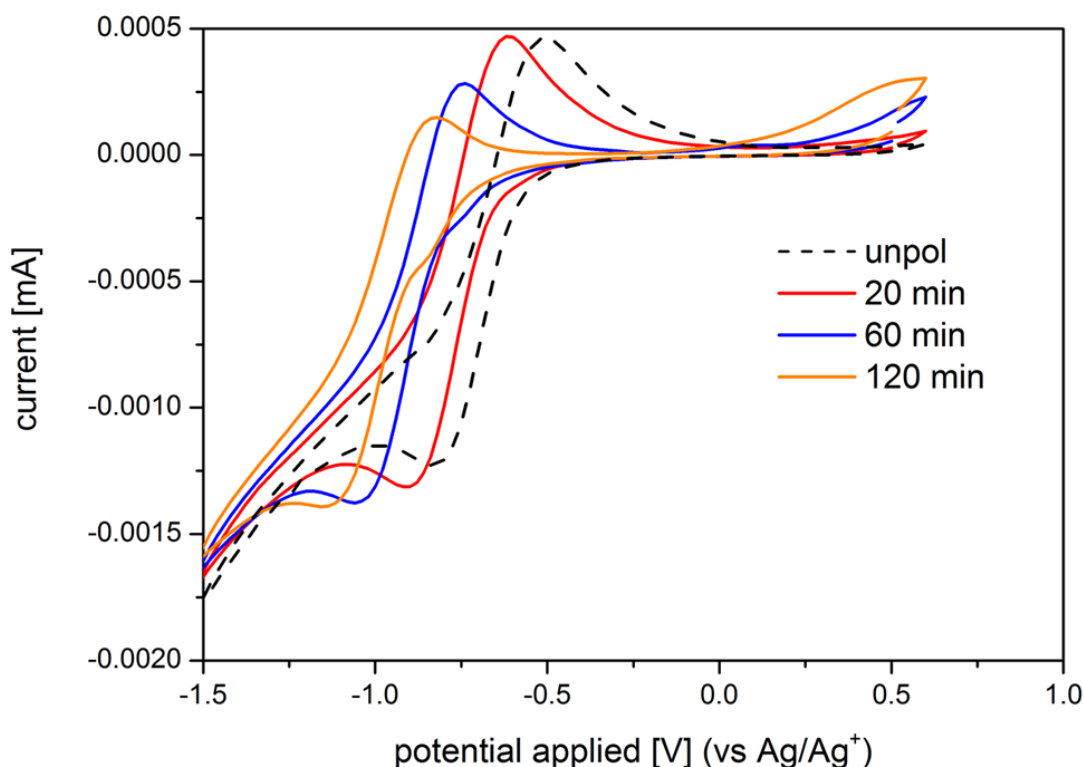

Figure 6-2: Cyclic voltammogram of in-situ polymerized fullerene C_{60}.

In addition to the LUMO levels of the polymerized compounds, UV-Vis measurements were performed to determine the optically active transitions of the material (Figure 6-3). The band-gap transition from the LUMO to the HOMO level is symmetry forbidden for C_{60} molecules. Only transitions starting from the second highest occupied orbital (HOMO-1) or ending in the second lowest unoccupied orbital (LUMO+1) are allowed.[23] The transitions in the UV-Visible

spectrum in Figure 6-3 can be attributed to the HOMO -> LUMO+1, the HOMO-1 -> LUMO

(both 2.7 eV) and the HOMO-1 -> LUMO+1 (3.7 eV) transition.
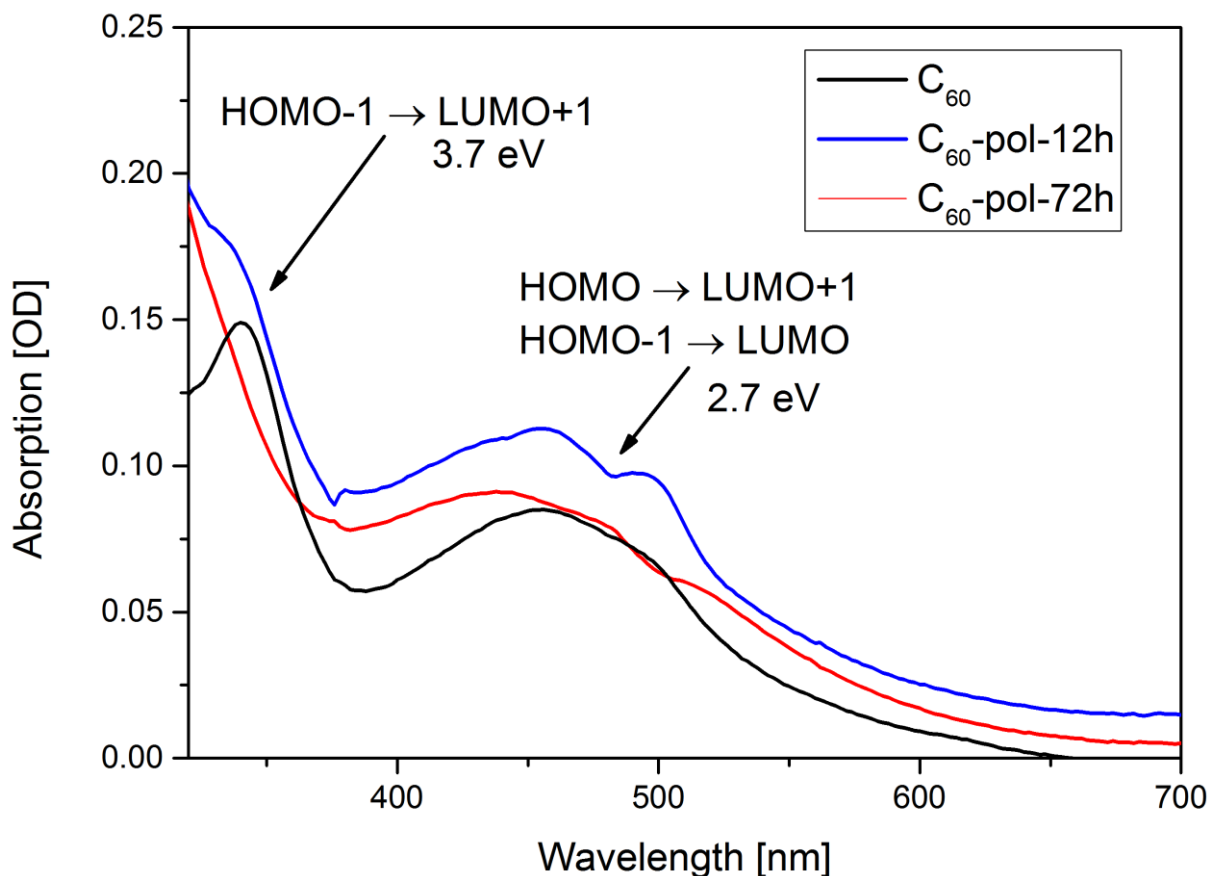
**Figure 6-3: UV-Visible absorption spectrum of pristine and photo-polymerized C$_{60}$ films. The
polymerization can be observed in the broadening of the peak at 3.7 eV or 340 nm.**

Upon polymerization, the energy levels of the individual orbitals change and due to a random

and unsymmetrical polymerization reaction, the energy levels broaden inhomogeneously,

which can be seen in the UV-Vis spectrum by the less defined transition at about 3.7 eV (or

340 nm). A similar behavior and change in energy levels has been reported before.[19] In

combination with photoluminescence measurements, the transition shifts have been attributed

to an increase in bandgap energy of about 100 meV.[19] The absolute value for the band-gap

energy has been estimated to be approximately 1.8 eV by a Tauc-plot of the absorption

spectrum, which is in good agreement with values reported in the literature.[24] In combination

6.2. Results and discussion

with our results from the electrochemical measurements, we can propose a schematic energy diagram for pristine and photo-polymerized C_{60} as depicted in Figure 6-4.
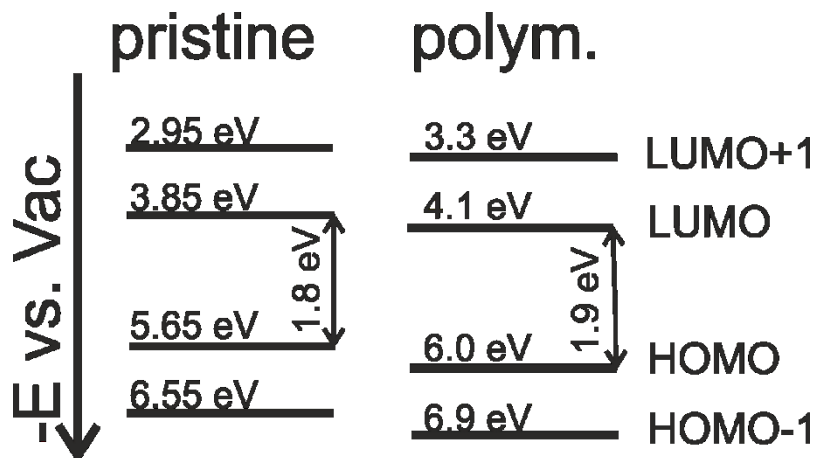
Figure 6-4: Proposed energy diagram for pristine and photopolymerized fullerene C_{60}.

The diagram shows all energy levels from HOMO-1 to LUMO+1 for pristine and photo-polymerized C_{60} films. The LUMO energy of C_{60} is lowered by 0.25 eV as determined via cyclic voltammetry, while the HOMO energy is lowered by 0.35 eV, leading to the observed increase in band-gap energy of 0.1 eV.

Apart from influencing the electronic structure of the molecules, photopolymerization also leads to a reduced solubility and increased stability of the C_{60} fullerene films. Although dimethylformamide is a relatively poor solvent for C_{60},[25] it can still dissolve parts of the layer during spincoating of the perovskite precursors and thus cause an increase of shunting paths between the perovskite and the FTO substrate and therefore a decrease in efficiency. This can be avoided by photo-polymerizing the C_{60} layer before deposition of the consecutive layers. Figure 6-5 shows the UV-Vis absorption spectra of DMF solutions that were incubated with either a polymerized or an unpolymerized C_{60} film of the same size and thickness for 5 minutes. As can be seen in the lower absorbance for the polymerized sample, less of the fullerene material is dissolved by the DMF as compared to the unpolymerized film. This enables the

fabrication of fully solution processed solar cells and renders the 2-step processing including an evaporation step unnecessary.[15]
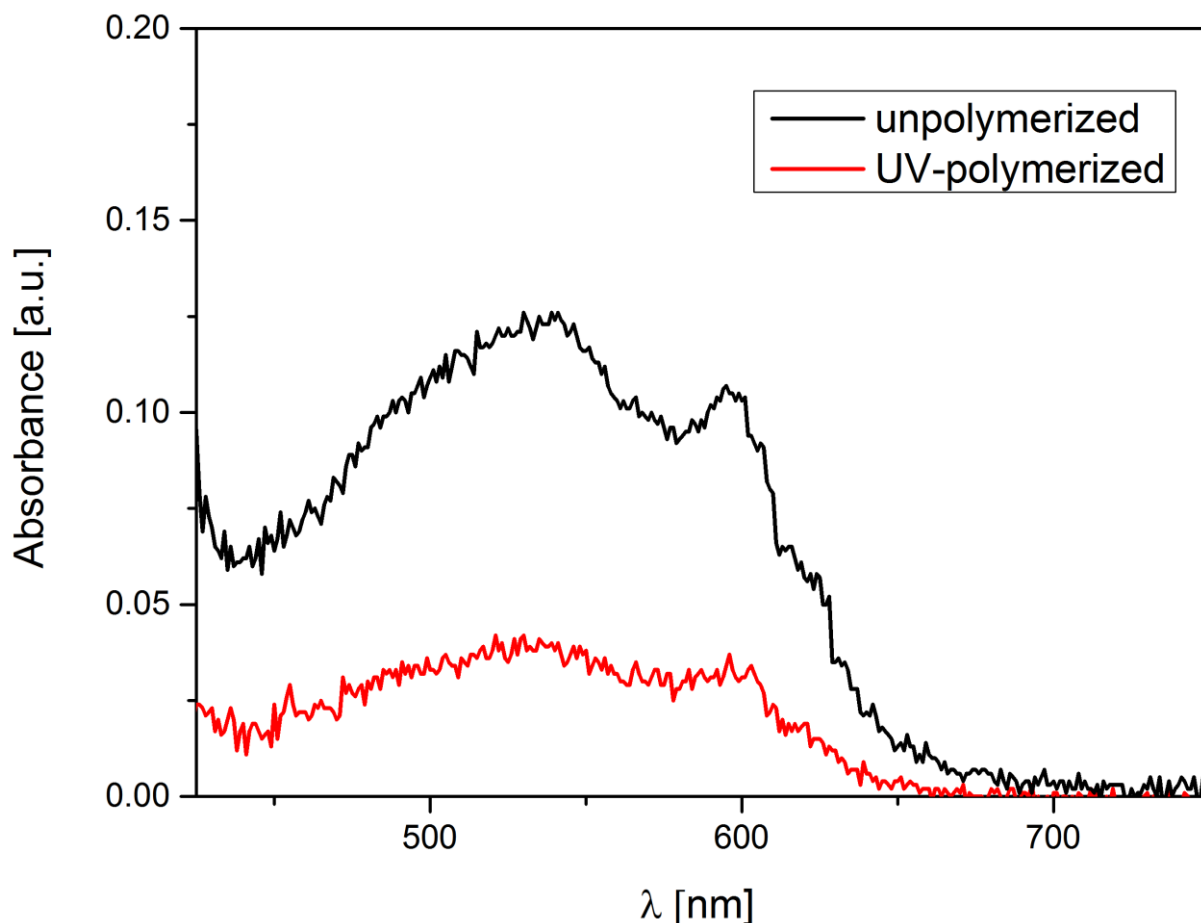
**Figure 6-5: UV-Vis absorption spectra of DMF solutions incubated with a polymerized or an unpolymerized C$_{60}$ film.**

To investigate the suitability of C$_{60}$ as n-type compact layer for perovskite solar cells and the influence of the photo-polymerization on the efficiency of complete solar cells were assembled. An approximately 20 nm thin layer of fullerene C$_{60}$ was deposited on the conductive FTO substrate via spincoating and, if applicable, polymerized. The perovskite MAPbI$_3$ was consecutively deposited via a sequential solution deposition.[26] The cell was completed by spincoating the hole transport layer spiro-OMETAD and evaporating a gold electrode. Detailed information about the preparation is provided in the experimental section. Figure 6-6 shows the

6.2. Results and discussion

general setup of the cells, where the perovskite layer is sandwiched between the n-type C_{60} layer and the p-type hole conductor Spiro-OMeTAD.

Figure 6-6: Standard solar cell layout, where the perovskite light absorber is sandwiched between a spiro hole conductor layer and a C_{60} electron selective contact.

The JV curves of the best performing solar cells employing pristine C_{60} or a photo-polymerized film are shown in Figure 6-7. The inset summarizes the photovoltaic parameters.


	J_{SC}	Efficiency	V_{OC}	Fill Factor
pristine C_{60}	13.8 mA/cm²	8.66%	1.02 V	0.62
polymerized	14.03 mA/cm²	7.98%	1.0 V	0.56
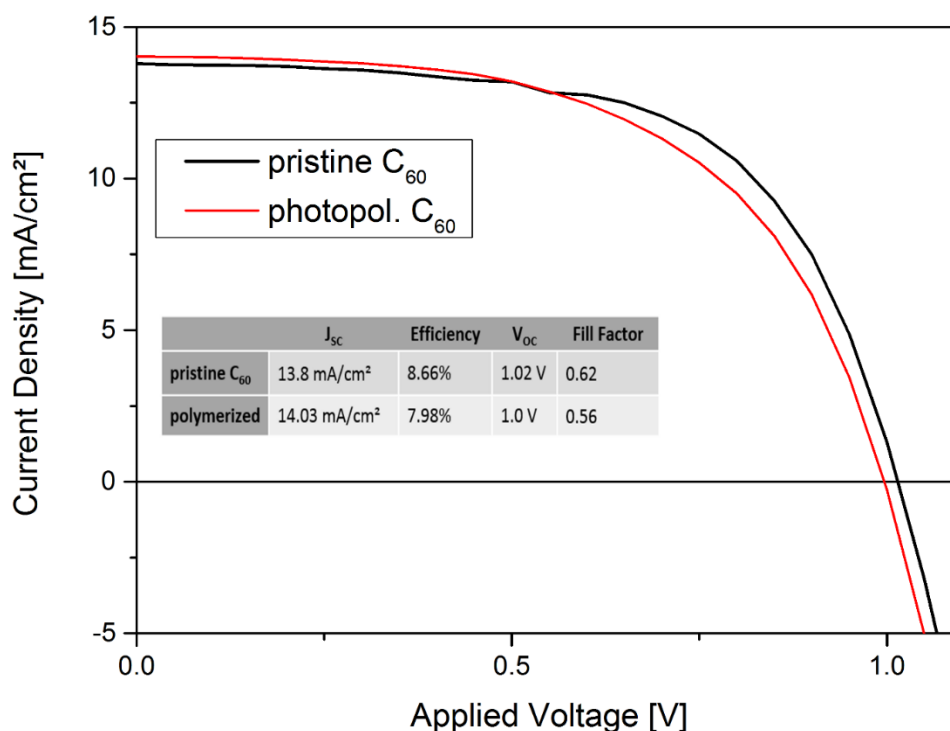
Figure 6-7: JV curves of the best performing solar cells employing a pristine or photo-polymerized C_{60} electron selective contact. The inset shows the measured values for the short circuit current (J_{SC}), the efficiency η, the open circuit voltage (V_{OC}) and the fill factor.

The LUMO level of pristine C_{60} (-3.85 eV) is well-aligned with the conduction band of the perovskite (-3.9 eV) so that no unnecessary loss in voltage is expected to occur here. The change

in the LUMO energy to -4.1 eV induced by the photopolymerization should improve the electron injection efficiency from the perovskite to the n-type layer since the offset between the respective LUMO levels is increased. Although this could have an unfavorable influence on the resulting open circuit voltage, the measured value remains constant upon polymerization.

Not only the open-circuit voltage, but all measured solar cell characteristics are almost identical for both samples. The small differences may well be attributed to sample-to-sample variations. It is, however, possible to find a difference between the two types of solar cells when looking at all measured samples and not just the best ones. It was apparent that about 85 % of the photo-polymerized samples achieved photovoltaic efficiencies above 5 %, while only about half of the samples with pristine C_{60} layers were even working cells. This can be attributed to the increased robustness of the photo-polymerized layers towards the solvents used during the solar cell fabrication. In particular DMF, although it is a relatively poor solvent for C_{60}, can dissolve small parts of the pristine films resulting in a damaged solar cell.

Apart from applying this photopolymerized electron selective contact in $MAPbI_3$-based solar cells, it may be suitable for other perovskite materials as well. The low lying LUMO energy of the polymerized C_{60} layer can be beneficial for the preparation of solar cells with smaller bandgaps than $MAPbI_3$. Devices employing, for example, $FAPbI_3$ (E_{LUMO} = -4.2 eV)[27] or $MASnI_3$ (E_{LUMO}=-4.17 eV)[28] should not be working efficiently with a pure fullerene contact layer because the electron transfer to the fullerene layer is inhibited. This behavior has been demonstrated for $FAPbI_3$/PCBM bilayers where the PCBM does not quench the photoluminescence of the $FAPbI_3$ completely.[27] The energy levels of possible perovskite materials and electron and hole conductors are depicted in Figure 6-8. By utilizing the polymerized fullerene layer these materials could be incorporated in efficient solar cells without the need for high temperature treated TiO_2 contact layers.
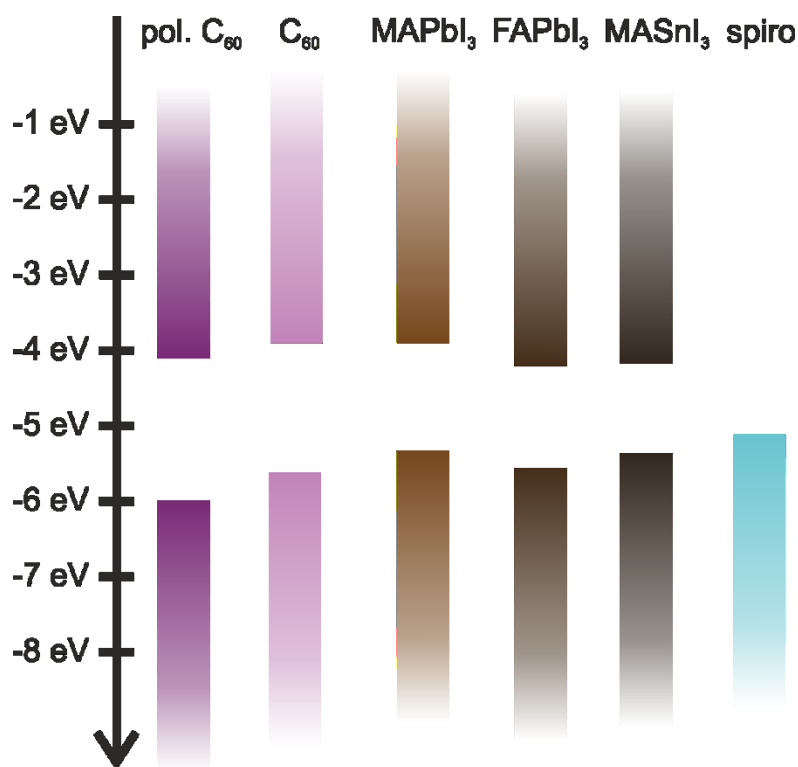
Figure 6-8: Comparison of the energy levels of various n-type, perovskite and p-type layers.

6.3 Conclusion

We have investigated the effect of photo-induced 2+2-cyclo addition of fullerene C_{60} films on solar cell behavior. Not only does the polymerization increase the resistivity of the fullerene layer to solvents used in the solar cell fabrication process, it also enables the tuning of the energy levels of C_{60} in a certain range. We have proposed energy diagrams for pristine and polymerized fullerene samples derived from in-situ cyclic voltammetry and UV/Vis absorption spectroscopy. We observed a stronger decrease for the HOMO energy level than for the LUMO level, leading to a widening of the band-gap by 0.1 eV. The prepared solar cells showed the same maximum efficiency for pristine and polymerized samples. When evaluating the percentage of cells yielding high power conversion efficiencies in each batch, 85 % of the polymerized cells work, while only 50 % of the pristine samples achieve reasonable efficiencies. Concluding, we illustrated the applicability of photo-polymerized fullerene as n-

type electron collecting layer for perovskite materials with lower lying LUMO energy levels than the conventionally used MAPbI$_3$, like FAPbI$_3$ or MASnI$_3$.

6.4   Experimental Section

Preparation of the methylammonium salts: methylammonium iodide was prepared following a recipe published earlier.[29] In short, 24 mL of methylamine solution (33 % in ethanol) was diluted with 100 mL of absolute ethanol. To this solution, a 10 mL aqueous solution of hydriodic acid (57 wt%) was added under constant stirring. After a reaction time of one hour at room temperature, the solvents were removed by rotary evaporation. The obtained white solid was washed with dry diethyl ether and finally recrystallized from ethanol.

To prepare the hydrochloride salt of methylamine, the hydriodic acid solution was replaced by 15 mL of concentrated hydrochloric acid (37 % in water). The purification procedure was the same as described above.

Solar cell preparation: Fluorine doped tin oxide (FTO) coated glass sheets (7 Ω/□, Pilkington) were etched with zinc powder and HCl (2 M) to obtain the required electrode pattern. The sheets were then washed with soap (2% Hellmanex in water), de-ionized water, acetone, and methanol and finally treated under oxygen plasma for 5 minutes to remove the last traces of organic residues.

A 20 nm thin layer of fullerene C$_{60}$ was deposited by spincoating a 20 mg/mL solution in 1,2-dichlorobenzene at 2000 RPM for 45 seconds. If applicable, the polymerization was performed by illuminating the samples with a handheld UV-lamp (Herolab GmbH, 365 nm, 50µW/cm²) in a nitrogen filled glove-box over night.

6.4. Experimental Section

A ~200 nm layer of lead iodide was deposited via spincoating from a 1 M PbI$_2$ solution in *N,N*-dimethylformamide (DMF) at 3000 rpm for 15 s. The films were immersed in a bath of 40 mL of MAI/MACl (9.5 mg/mL and 0.5 mg/mL, respectively) and heated to 60 °C for 5 minutes. Once the conversion was finished, the films were washed with clean, anhydrous isopropanol and dried under a nitrogen stream.

After drying, the films were covered with a 400 nm layer of Spiro-OMeTAD (Borun Chemicals, 99.1% purity) "spiro". 96 mg of spiro were dissolved in 1 mL of chlorobenzene and mixed with 10 mL 4-*tert*-butylpyridine (*t*BP) and 30 µL of a 170 mgmL^{-1} bis(trifluoromethane)sulfonimide lithium salt (LiTFSI) solution in acetonitrile. This solution was spincoated at 1500 rpm for 45 seconds. Before evaporating the gold electrodes, Spiro-OMeTAD was allowed to oxidize in air over night at room temperature and 15-20% rel. humidity.

Characterization details:

Cyclic voltammetry was performed with a µ-Autolab 3. A thin film of fullerene C$_{60}$ was deposited on a glassy carbon substrate and immersed in a 0.1 M solution of Bu$_4$NBF$_4$ in acetonitrile as working electrode. The electrochemical cell was also equipped with a platinum mesh acting as counter electrode and an Ag/AgCl reference electrode. CV was performed in the range of -1.5 to 0.7 V at a scan rate of 50 mV/s. The samples were in situ polymerized by illumination with a 365 nm high power LED (Thorlabs, 365 nm, 150 µW/cm²). Illumination for 2 minutes and subsequent CV measurements were alternated for 8 hours.

J-V curves were recorded with a Keithley 2400 sourcemeter under simulated AM 1.5 sunlight, calibrated to 100 mW cm^{-2} with a Fraunhofer ISE certified silicon cell. The active area of the solar cells was defined with a square metal aperture mask of 0.0831 cm^2.

Steady-state absorption spectra were acquired with a Lambda 1050 UV/Vis spectrophotometer (Perkin Elmer) using an integrating sphere.

6.5 Literature

[1]   H. W. Kroto, J. R. Heath, S. C. O'Brien, R. F. Curl, R. E. Smalley, *Nature* **1985**, *318*, 162.

[2]   W. Krätschmer, L. D. Lamb, K. Fostiropoulos, D. R. Huffman, *Nature* **1990**, *347*, 354.

[3]   D. Jerome, *Science* **1991**, *252*, 1509.

[4]   J. C. Hummelen, B. W. Knight, F. LePeq, F. Wudl, J. Yao, C. L. Wilkins, *J. Org. Chem.* **1995**, *60*, 532.

[5]   A. M. Rao, P. Zhou, K.-A. Wang, G. T. Hager, J. M. Holden, Y. Wang, W.-T. Lee, X.-X. Bi, P. C. Eklund, D. S. Cornett, M. A. Duncan, I. J. Amster, *Science* **1993**, *259*, 955.

[6]   B. Sundqvist, *Adv. Phys.* **1999**, *48*, 1.

[7]   V. D. Blank, S. G. Buga, G. A. Dubitsky, N. R. Serebryanaya, M. Y. Popov, B. Sundqvist, *Carbon* **1998**, *36*, 319.

[8]   Y. Iwasa, T. Arima, R. M. Fleming, T. Siegrist, O. Zhou, R. C. Haddon, L. J. Rothberg, K. B. Lyons, H. L. Carter, A. F. Hebard, R. Tycko, G. Dabbagh, J. J. Krajewski, G. A. Thomas, T. Yagi, *Science* **1994**, *264*, 1570.

[9]   N. Takahashi, H. Dock, N. Matsuzawa, M. Ata, *J. Appl. Phys.* **1993**, *74*, 5790.

[10]   M. Núñez-Regueiro, L. Marques, J. L. Hodeau, O. Béthoux, M. Perroux, *Phys. Rev. Lett.* **1995**, *74*, 278.

[11]   N. J. Jeon, J. H. Noh, W. S. Yang, Y. C. Kim, S. Ryu, J. Seo, S. I. Seok, *Nature* **2015**, *517*, 476.

[12]   W. S. Yang, J. H. Noh, N. J. Jeon, Y. C. Kim, S. Ryu, J. Seo, S. I. Seok, *Science* **2015**, *348*, 1234.

[13]   J. P. Mailoa, C. D. Bailie, E. C. Johlin, E. T. Hoke, A. J. Akey, W. H. Nguyen, M. D. McGehee, T. Buonassisi, *Appl. Phys. Lett.* **2015**, *106*, 121105.

[14]   C. D. Bailie, M. G. Christoforo, J. P. Mailoa, A. R. Bowring, E. L. Unger, W. H. Nguyen, J. Burschka, N. Pellet, J. Z. Lee, M. Gratzel, R. Noufi, T. Buonassisi, A. Salleo, M. D. McGehee, *Energy Environ. Sci.* **2015**, *8*, 956.

[15]   K. Wojciechowski, T. Leijtens, S. Spirova, C. Schlueter, M. Hoerantner, J. T.-W. Wang, C.-Z. Li, A. K. Y. Jen, T.-L. Lee, H. J. Snaith, *J. Phys. Chem. Lett.* **2015**, *6*, 2399.

[16]   K. T. Butler, J. M. Frost, A. Walsh, *Mater. Horiz.* **2015**, *2*, 228.

[17]   P. Schulz, L. L. Whittaker-Brooks, B. A. MacLeod, D. C. Olson, Y.-L. Loo, A. Kahn, *Adv. Mater. Interfaces* **2015**, *2*, n/a.

[18] H. Zhou, Q. Chen, G. Li, S. Luo, T.-b. Song, H.-S. Duan, Z. Hong, J. You, Y. Liu, Y. Yang, *Science* **2014**, *345*, 542.

[19] Y. Wang, J. M. Holden, A. M. Rao, P. C. Eklund, U. D. Venkateswaran, D. Eastwood, R. L. Lidberg, G. Dresselhaus, M. S. Dresselhaus, *Phys. Rev. B* **1995**, *51*, 4547.

[20] C. Jehoulet, A. J. Bard, F. Wudl, *J. Am. Chem. Soc.* **1991**, *113*, 5456.

[21] P. Allemand, A. Koch, F. Wudl, Y. Rubin, F. Diederich, M. Alvarez, S. Anz, R. Whetten, *J. Am. Chem. Soc.* **1991**, *113*, 1050.

[22] D. Dubois, G. Moninot, W. Kutner, M. T. Jones, K. M. Kadish, *J. Phys. Chem.* **1992**, *96*, 7137.

[23] A. Skumanich, *Chem. Phys. Lett.* **1991**, *182*, 486.

[24] T. Rabenau, A. Simon, R. K. Kremer, E. Sohmen, *Z. Physik B - Condensed Matter* **1993**, *90*, 69.

[25] K. N. Semenov, N. A. Charykov, V. A. Keskinov, A. K. Piartman, A. A. Blokhin, A. A. Kopyrin, *J. Chem. Eng. Data* **2010**, *55*, 13.

[26] Z.-K. Tan, R. S. Moghaddam, M. L. Lai, P. Docampo, R. Higler, F. Deschler, M. Price, A. Sadhanala, L. M. Pazos, D. Credgington, *Nature nanotechnology* **2014**.

[27] G. E. Eperon, S. D. Stranks, C. Menelaou, M. B. Johnston, L. M. Herz, H. J. Snaith, *Energy Environ. Sci.* **2014**, *7*, 982.

[28] K. P. Marshall, R. I. Walton, R. A. Hatton, *J. Mater. Chem. A* **2015**, *3*, 11631.

[29] M. M. Lee, J. Teuscher, T. Miyasaka, T. N. Murakami, H. J. Snaith, *Science* **2012**, *338*, 643.

7 Preparation of Single-Phase Films of $CH_3NH_3Pb(I_{1-x}Br_x)_3$ with Sharp Optical Band Edges

This chapter is based on the following publication:

Initial experiments, sample preparation and basic material characterization have been performed by P. Docampo and F. Hanusch. PDS measurements have been performed by A. Sadhanala. TA measurements have been performed by F. Deschler

7.1 Introduction

Solution processable optoelectronic devices offer costeffective, large-scale manufacturing capability. Hybrid organic−inorganic perovskite $(CH_3NH_3PbI_{3-x}Cl_x)$ solar cells[1-4] now show photovoltaic (PV) performance approaching 18%,[5] and high charge-carrier mobilities.[6] Perovskite films have also shown promising photoluminescence quantum efficiencies (PLQEs) of more than 70% and lasing, making them a promising candidate for cost-effective and efficient LEDs and lasing applications.[7, 8] Despite the rapid progress in the past few years, relatively little is known about the properties required for efficient perovskite PV systems or why perovskite works so well in PVs while simultaneously demonstrating high PLQE. It has recently been demonstrated by Noh et al. that the bandgap of the perovskite can be tuned by varying the halide (i.e., bromide, iodide) composition of the perovskite precursor solution.[9, 10] High open-circuit voltages have been demonstrated by using the higher bandgap tribromide-based perovskite.[11, 12]

7.2. Results and Discussion

The control of bandgap with mixed halide systems is attractive, but it is important to establish whether these form solid solutions, with monotonic variation of lattice constants and bandgap, or if there is compositional inhomogeneity, which may introduce a range of local bandgaps and reduce PV performance. To address this question, we use photothermal deflection spectroscopy (PDS) and photoluminescence measurements that are able to detect low levels of subgap states in the system $CH_3NH_3Pb(I_{1-x}Br_x)_3$ ($0 \leq x \leq 1$). We correlate our findings with the structural information obtained by X-ray diffraction (XRD) measurements. We find that films of mixed trihalide perovskites initially form a system with two absorption and luminescence features. Following our fabrication protocol, these convert to a homogeneous intermixed system with only one species within the detection limits of the techniques used in this work. The ability to engineer a single bandgap in these mixed compositions is important for the development of solar cells. We demonstrate a bromide−iodide lead perovskite film ($CH_3NH_3PbI_{1.2}Br_{1.8}$) with an optical bandgap of 1.94 eV, which is optimal for tandem cell applications with c-Si cells. Our findings also show that pure trihalide perovskites have a remarkably low energetic disorder, which is, to our knowledge, by far the lowest reported for any low temperature solution-processable material.[13, 14]

7.2   Results and Discussion

PDS is an ultrasensitive absorption measurement technique that detects heating of the sample due to the nonradiative relaxation of absorbed light and is insensitive to reflection and scattering. PDS can be used to characterize energetic disorder as the exponential decay of the absorption below the bandgap with a characteristic energy, the Urbach energy (E_u), and has been used to study the perovskite materials system.[14] The Urbach energy is given by $A(E) \propto e^{E/(E_u)}$, where A is the absorbance and E is the excitation energy in electronvolts. In Figure 7-1,

the linear fit to the Urbach tail in the PDS data for the pure triiodide perovskite is shown, which

yields an Urbach energy of ~15 meV that is similar to that obtained by De Wolf et al.[14] This

value is about twice the typical value for single-crystal GaAs and half that of polycrystalline

CIGS.[13, 15]
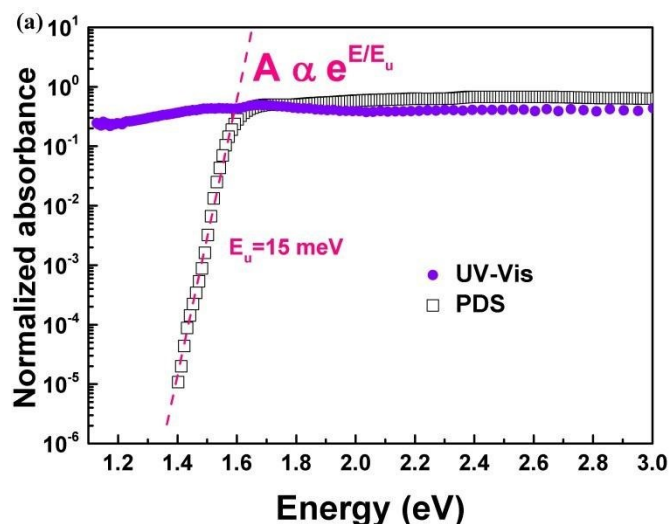
Figure 7-1: Normalized absorption spectra of CH₃NH₃PbI₃ obtained by UV-Vis and PDS techniques along-with the linear fit (dotted line) of the Urbach tail (in the PDS spectra) to obtain the Urbach energy (~15 meV). Absorbance was normalized at the band edge ~ 1.7 eV.

We prepared perovskite thin films by spin-coating from a precursor solution composed of 1:1

organic to inorganic ratios (CH₃NH₃I to PbI₂ and CH₃NH₃Br to PbBr₂) under a N₂ atmosphere

in a glovebox. Solutions with varying iodide to bromide concentration were prepared by mixing

the respective pure triiodide (CH₃NH₃PbI₃) and tribromide (CH₃NH₃PbBr₃) precursor solution

in the respective ratios. Energy-dispersive X-ray spectroscopy (EDX) measurements show that

the ratios of bromide to iodide in the film are the same as those in the solution (see Figure 7-2

and Table 7-1)
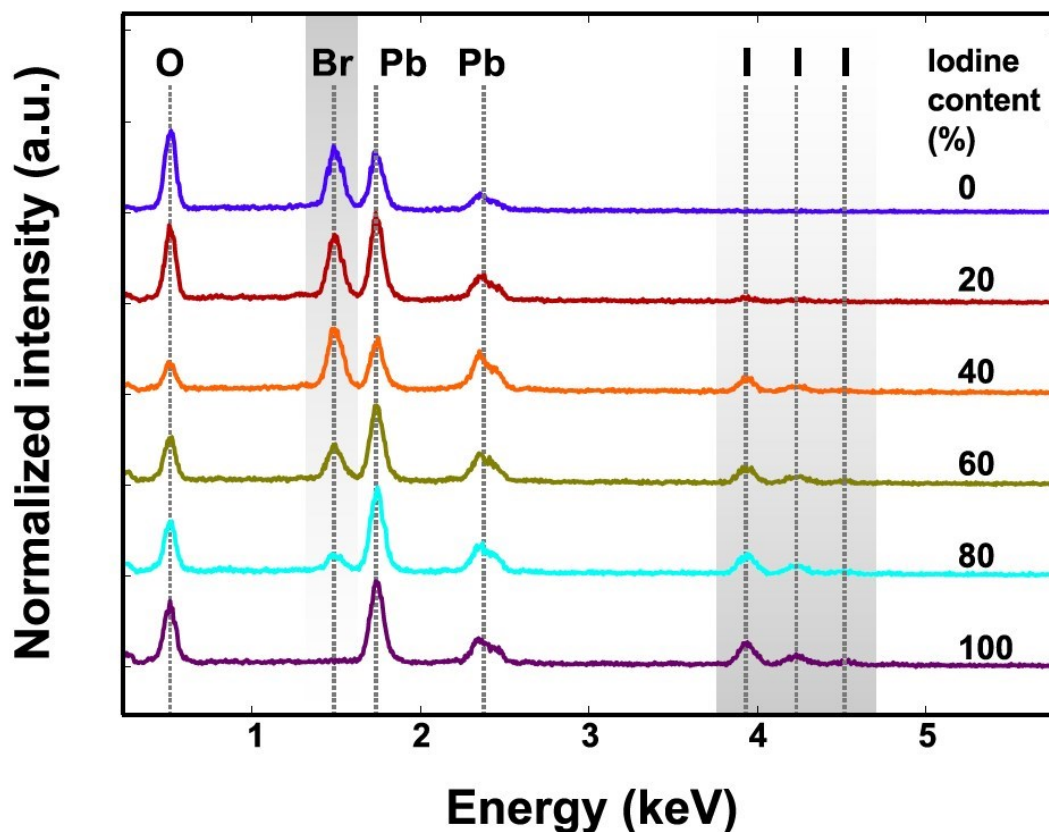
Figure 7-2: EDX measurements of 1:1 molar methylammonium halide-lead halide films of various Iodide-bromide ratios as indicated in iodide%

Table 7-1: Elemental composition of 1:1 molar methylammonium halide-lead halide films of various Iodide-bromide ratios as indicated in iodide%

% I in solution	20	40	60	80
% Br in solution	80	60	40	20
%I in film	17	36	53	71
%Br in film	83	64	47	29

By increasing the concentration of the pure triiodide perovskite in the tribromide perovskite in solution from 0 to 100%, we tune the bandgap of the resulting perovskite between the extremes of pure triiodide and tribromide perovskites from 2.23 to 1.57 eV (Figure 7-3a,c). We detect the absorption edge of the pure triiodide lead perovskite $CH_3NH_3PbI_3$ down to the detection limit of the PDS setup without observing a leveling off, which indicates a very clean bandgap

and sharp band edge. This very clean gap is preserved as bromide is added up to 20% bromide (80% iodide) content.
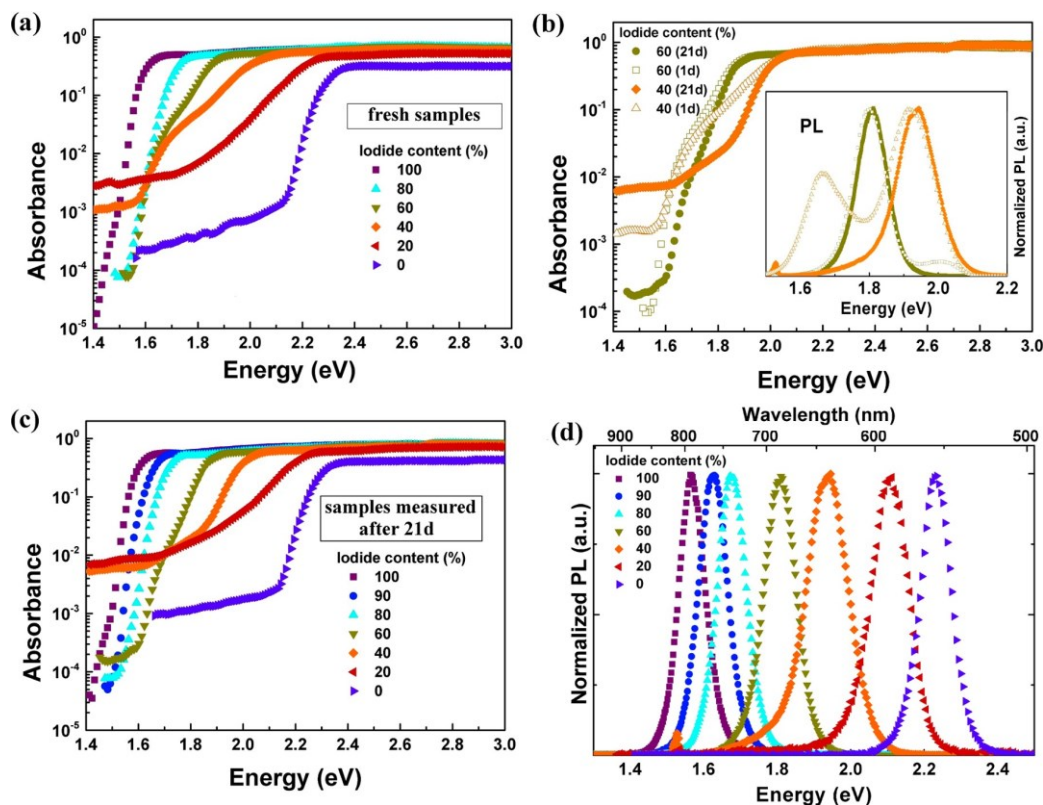

Figure 7-3: (a,c) PDS measurements for 1:1 molar methylammonium lead-halide thin films with different iodide−bromide ratios, as indicated, measured directly after fabrication (a) and 21 days later (c). **(b)** Change in PDS spectrum for films measured on the same day after annealing and after 21 days. Inset shows the corresponding change in the PL spectra. **(d)** PL spectra of 1:1 molar methylammonium lead-halide thin films with different iodide−bromide ratios, as indicated, measured after 21 days. Excitation for PL was performed with a pulsed laser system at 3.1 eV photon energy with fluence ~1 μJ/cm² and 100 fs pulse length. PL spectra have been normalized to the peak emission.

For the pure tribromide perovskite, CH₃NH₃PbBr₃, a sharp band edge with additional levels of sub-bandgap absorption is found, which indicates a population of sub-bandgap states. The absorption edge for films with 20% iodide shows a broad absorption tail below the band edge and significant sub-bandgap absorption below ~1.8 eV. We interpret this as increased disorder in these films and a significant population of sub-bandgap states. Notably, for iodide−bromide mixtures with 40 and 60% iodide content, the films show a clear shoulder in the subgap absorption (Figure 7-3b). We interpret this as the initial formation of two species in these films.

7.2. Results and Discussion

Photoluminescence (PL) measurements of the bromide−iodide lead perovskite films with 40 and 60% iodide content show two emission peaks Figure 7-3b inset). Time-resolved PL measurements (Figure 7-4a,b) show that the higher energy emission band decays more rapidly than the lower energy band. These findings suggest that the initially formed mixed-halide perovskite films, having 40 and 60% iodide content, comprise two species. We note, in particular, that for the 40% iodide films the second phase emits around 1.68 eV from a significantly lower energy than the 1.94 eV emissive feature, and this represents a potential loss mechanism for PV devices.
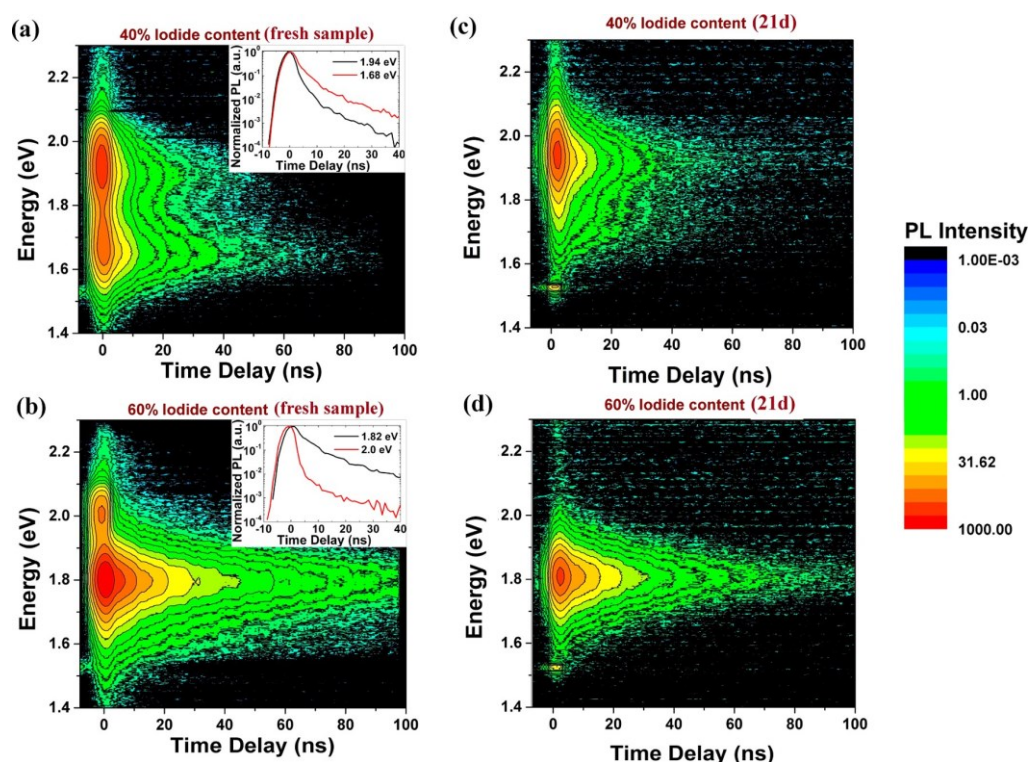

Figure 7-4: Plot of PL intensity versus time and emission wavelength for 1:1 molar methylammonium halide−lead-halide films with an iodide content of 40 (a,c) and 60% (b,d) fresh samples and remeasured after 21 days. Inset in panels a and b shows the kinetics of the respective PL peaks at the stated energies. Excitation for PL was performed with a pulsed laser system at 3.1 eV photon energy with fluence ~1 μJ/cm² and 100 fs pulse length.

Surprisingly, we found that the PDS absorption and PL spectra changed after the films were stored under an inert nitrogen atmosphere at room temperature (these changes were complete within 3 weeks and showed no significant further evolution at 13 weeks) (Figure 7-3b). A

similar effect was observed in fresh films prepared from solutions that had been kept at room temperature for several days (see Figure 7-5). The most striking changes in the PDS spectra in these aged films, which we term here "single-phase" films, is the sharpening of the band edges and the loss of the extra absorption shoulder in the subgap.
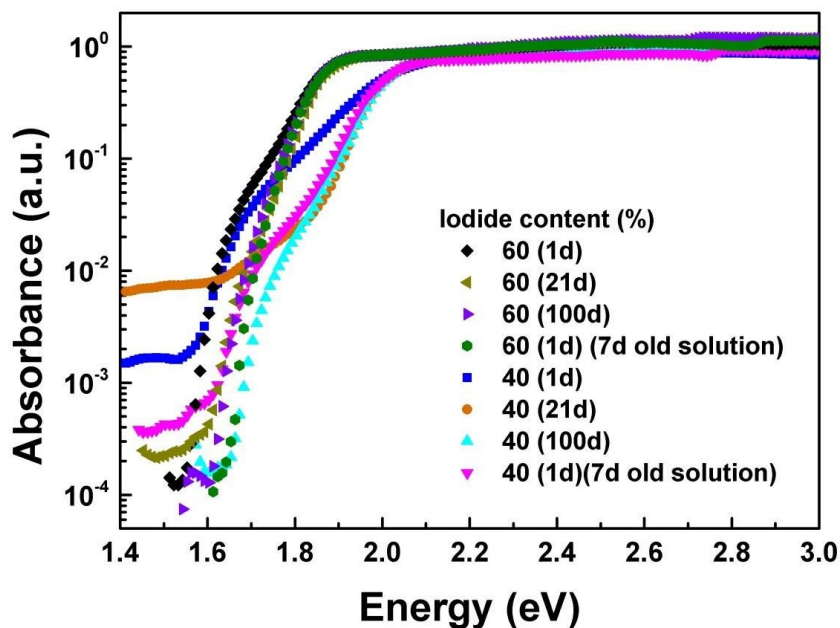

Figure 7-5: PDS spectra of samples on glass prepared from 1:1 molar methylammonium halide-lead halide fresh solution with different iodine-bromine ratios as indicated by the iodide content in the films, with different aging of films and the fresh films prepared from 7 day old solution.

In detail, in the as-formed films with low iodide contents (20 and 40%), made from fresh solutions, we find additional subbandgap absorption and broadened band edges. However, there is no longer a second phase detectable within the resolution of the PDS setup if the films are allowed to age or are made from aged solutions. For all other iodide contents (0, 80, 90, and 100%), the PDS absorption spectra show sharp band edges and little differences compared with the films measured directly after preparation. The steady-state PL spectra of the "single phase" films (Figure 7-3d) show single transitions with a monotonic shift in peak position with increasing iodide content from pure tribromide perovskite (2.23 eV) to pure triiodide perovskite

7.2. Results and Discussion

(1.57 eV). This finding supports our observation of a clean bandgap in these films. The photoluminescence kinetics (Figure 7-6d) show single bimolecular decays for the pure iodide and bromide films and also for iodide-rich films down to 60% iodide, as reported previously for the iodide material.[8] Films with 20 and 40% iodide content both show fast kinetics. These findings also point toward one photoactive species from which emission arises in the bromide−iodide lead perovskite films.
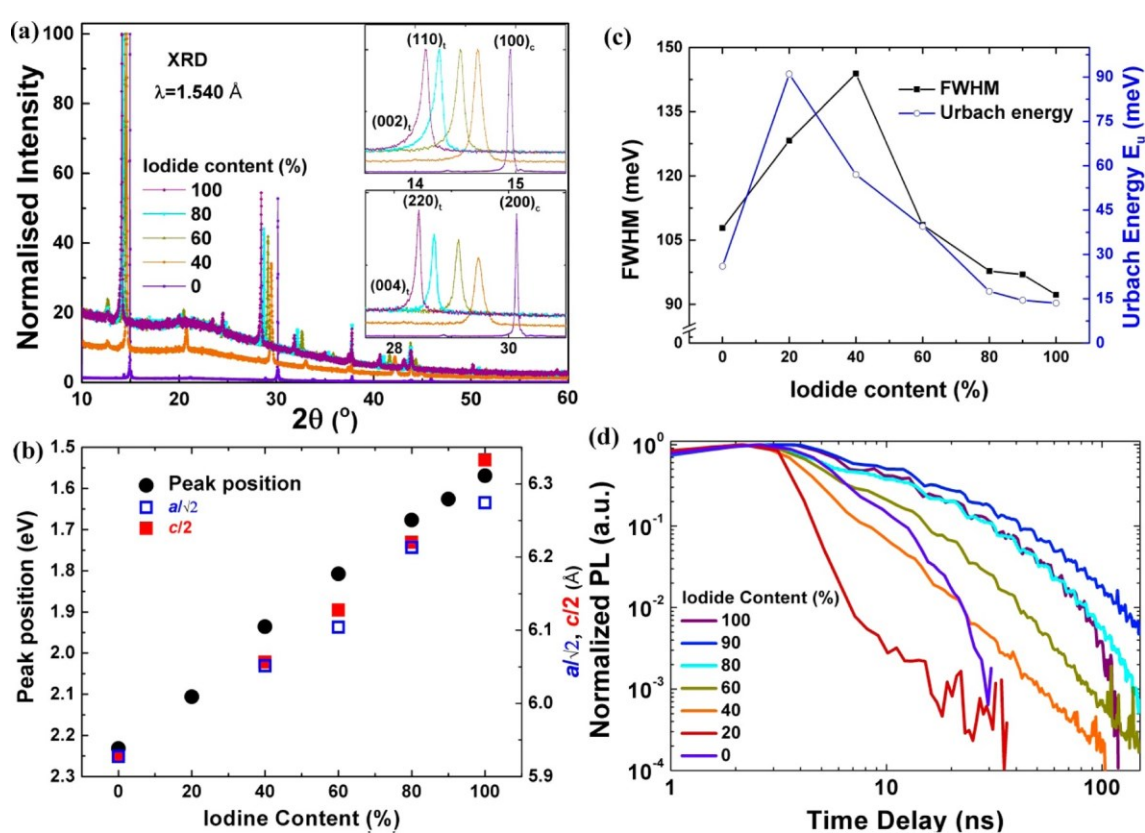

Figure 7-6: (a) Intensity-normalized X-ray diffraction patterns of 1:1 molar methylammonium lead-halide thin films with different iodide-bromide ratios, as indicated. The evolution of the position of the (002)$_t$ and (110)$_t$ [(100)$_c$] and the (004)$_t$ and (220)$_t$ [(200)$_c$] peaks as a function of composition are shown in the upper and lower insets, respectively. (b) Variation of PL peak positions (closed circles) and normalized lattice parameters a/√2 (open squares) and c/2 (closed squares) determined from XRD measurements for films with different iodide content. (c) Comparison of the change in fwhm of the PL emission peak and the Urbach energy calculated from PDS measurements for the same films measured after 21 days. (d) Plot of normalized PL intensity versus time for same films. Excitation for PL was performed with a pulsed laser system at 3.1 eV photon energy with fluence ~1 μJ/cm² and 100 fs pulse length.

Time-resolved PL spectra of "single-phase" films also show one emissive species Figure 7-4c,d).

Figure 7-6c shows the full width at half-maximum (fwhm) of the PL peaks together with the

Urbach energy calculated from PDS measurements. Both parameters follow similar trends,

peaking below 50% iodide content. We take this observation as an indication that absorption

and emission arise from similar states. We find that the pure tribromide perovskite films and

films with 100 to 80% of iodide content show the lowest fwhm and the lowest Urbach energies.

This indicates very low disorder and sharp band edges in the films with higher iodide content

compared with the ones with lower iodide content. Also, the larger fwhm and Urbach energies

for films with 20 and 40% than for those with higher iodide content correlate with shorter

lifetimes observed in transient PL (Figure 7-6d). However, when we compare the PL peak

positions with the PDS absorption data, we find that the emission peaks for all films lie at the

energy where the absorption has dropped to ~15% of its maximum band edge value. (See Figure

7-7)
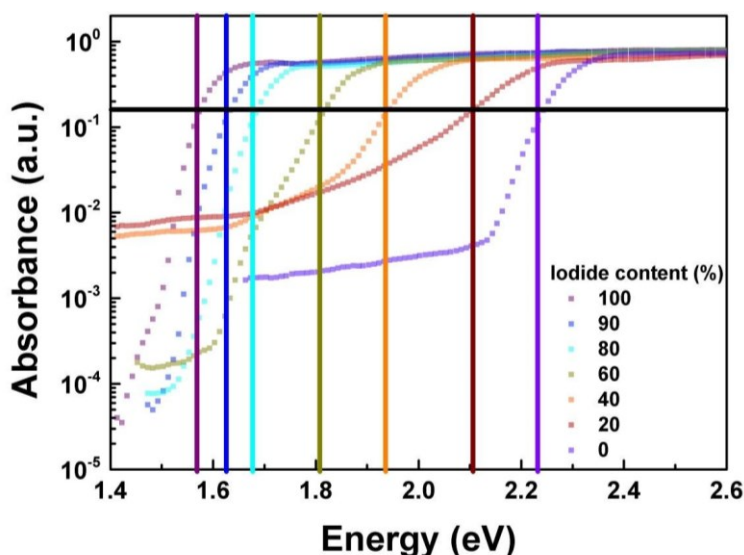
Figure 7-7: PDS measurements for film samples on glass prepared from 1:1 organic-inorganic films with different iodide-bromide ratios as indicated, measured 21d after fabrication. The vertical lines indicate the PL emission peaks for the respective iodide contents.

First, this indicates that impurity levels at lower energy do not play a significant role in the

radiative recombination of excited states. Therefore, they do not represent a major radiative

form of energetic loss channel due to energy relaxation down to the lower lying states within the subgap. Moreover, the lower subgap absorption detected for "single-phase" films suggests a lower density of states that recombine through nonradiative relaxation, which again indicates a cleaner material system.

Powder X-ray diffraction measurements were carried out on "single phase" films over the entire composition range (Figure 7-6a). A systematic shift in the patterns to lower scattering angles is observed as the concentration of iodide increases, indicating an expansion of the unit cell with increasing iodide fraction. Because of preferential alignment in the films, a complete structural analysis was not possible. The symmetry and lattice parameters were modeled using a Le Bail analysis[16] in the Fullprof suite of programmes (see Figure 7-8).[17]
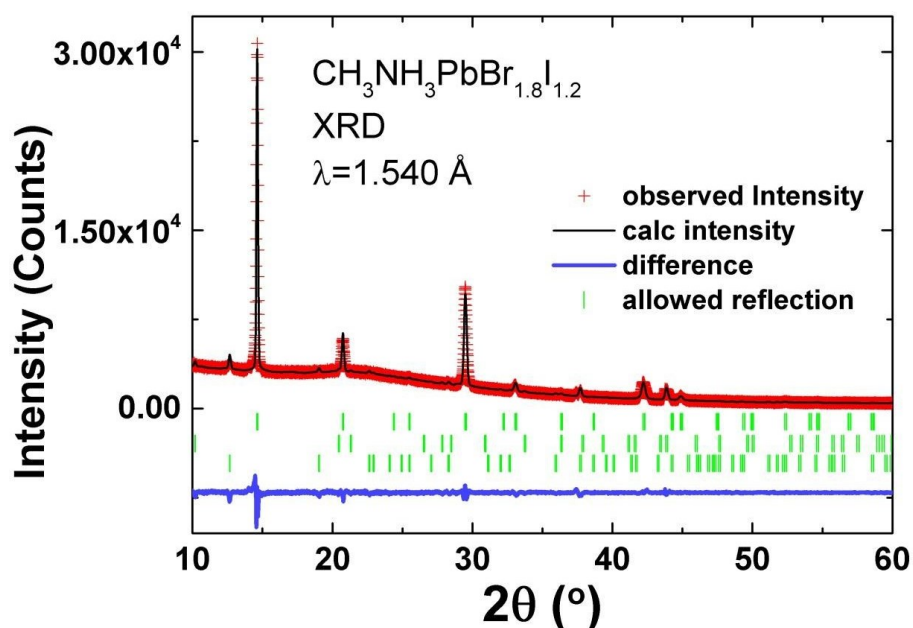

Figure 7-8: Observed X-ray diffraction pattern (red crosses) and calculated Le Bail intensity (black line) for CH$_3$NH$_3$PbBr$_{1.8}$I$_{1.2}$ at room temperature. The difference (blue line) is below, tick marks indicating the reflection positions for CH$_3$NH$_3$PbBr$_{1.8}$I$_{1.2}$ perovskite (upper) and the CH$_3$NH$_3$X (middle) and PbX$_2$ (lower) [X=I,Br] impurity phases are also shown.

The characteristic perovskite peak at $2\theta = 30°$ (Figure 7-6a, inset) shows a significant broadening of the $(200)_c$ reflection in all films containing iodide. We ascribe this to a tetragonal distortion and the emergence of two unique reflections, $(002)_t$ and $(110)_t$; a similar although less pronounced splitting is also observed in the $(100)_c$ reflection with iodide present (Figure 7-6a, inset). Therefore, with the exception of the pure bromide film, all films were modeled using a tetragonal unit cell with I4cm symmetry, as has previously been reported for $CH_3NH_3PbI_3$.[18] The pure bromide film was modeled using a higher symmetry $Pm\bar{3}m$ cubic structure.[18] In all films, unreacted starting materials of CH_3NH_3X and PbX_2 were detected in addition to the main perovskite phase. The unit cell of the tetragonal phase, a_t and c_t, can be related to that of the cubic cell, a_c, by $a_t = \sqrt{2}a_c$ and $c_t = 2a_c$. When the cell parameters of the tetragonal cell are normalized, $a_t/\sqrt{2}$, $c_t/2$, to allow for direct comparison to the cubic perovskite structure, a linear increase in the size of the normalized unit cell with increasing iodide fraction is observed (Figure 7-6b). This is consistent with both the larger ionic radii of iodide ($r = 2.2$ Å) with respect to bromide ($r = 1.96$ Å) and Vegard's law for a continuous solid solution. The degree of tetragonal distortion, $((c_t - \sqrt{2}a_t)/((a_t/\sqrt{2}) + (c_t/2)))$, also increases with iodide concentration reaching a maximum value of 0.9% in $CH_3NH_3PbI_3$. An additional broadening of reflections in the mixed halide films is observed (Figure 7-6a, inset), which cannot be described as resulting only from changes in the symmetry. We attribute this to strain broadening. Strain of this type could be due to quenching of a higher temperature (cubic) symmetry phase or could arise from an inhomogeneous halide distribution beyond random site occupancy.

In Figure 7-6b, we compare the extracted normalized lattice parameters with the optically determined PL peak positions. Both lattice parameters and PL peak energies follow a linear trend with iodide fraction. These observations support our finding that there is a single solid solution across the full composition range that can be obtained using a straightforward

fabrication protocol. This protocol requires "aging" of either the starting solution or the as-prepared films. The underlying reason for the observed effect is currently under investigation.

7.3 Conclusion

Our demonstration of remarkably clean bromide/iodide solid solutions in this organometallic halide PV system brings this remarkable family of materials in line with classic semiconductor systems such as MBE-grown III-Vs including AlGaAs.

7.4 Experimental Section

Details of film preparation

Detailed information about the perovskite synthesis and solution preparation can be found elsewhere [9]. All the perovskite films were spun on quartz glass substrates at 2000 RPM for 45 s and then annealed at 100°C for 45 min. All the samples were coated with PMMA using a 10 mg/ml chlorobenzene solution spun at 1500 RPM for 60 s. This was done to prevent degradation of the films in air.

Details of XRD measurements

X-ray diffraction measurements were made on thin film samples of $CH_3NH_3Pb(I_{1-x}Br_x)_3$, $0 \leq x \leq 3$, on a Bruker D8 discover diffractometer with Cu K radiation, $\lambda = 1.5403$ Å. Samples were measured using a Bragg-Brentano geometry over $10 \leq 2\Theta \leq 60°$ with a step size of $2\Theta = 0.01°$. Due to preferential alignment in the films a complete structural analysis was not possible. Instead, the symmetry and lattice parameters were modelled using a Le Bail analysis in the Fullprof suite of programmes. Backgrounds fit were performed using a refined interpolation of points and the peak shape modelled using a pseudo-Voigt function.

Details of PDS measurements

PDS is a scatter-free surface sensitive absorption measurement capable of measuring 5-6 orders of magnitude weaker absorbance than the band edge absorption. For the measurements, a monochromatic pump light beam is shined on the sample (film on Quartz substrate), which on absorption produces a thermal gradient near the sample surface via nonradiative relaxation induced heating. This results in a refractive index gradient in the area surrounding the sample surface. This refractive index gradient is further enhanced by immersing the sample in an inert liquid FC-72 Fluorinert® (3M Company) which has a high refractive index change per unit change in temperature. A fixed wavelength CW laser probe beam is passed through this refractive index gradient producing a deflection proportional to the absorbed light at that particular wavelength, which is detected by a photo-diode and lock-in amplifier combination. Scanning through different wavelengths gives us the complete absorption spectra. Because this technique makes use of the non-radiative relaxation processes in the sample, it is immune to optical effects like interference and scattering. Figure 7-9shows a schematic of the PDS setup.
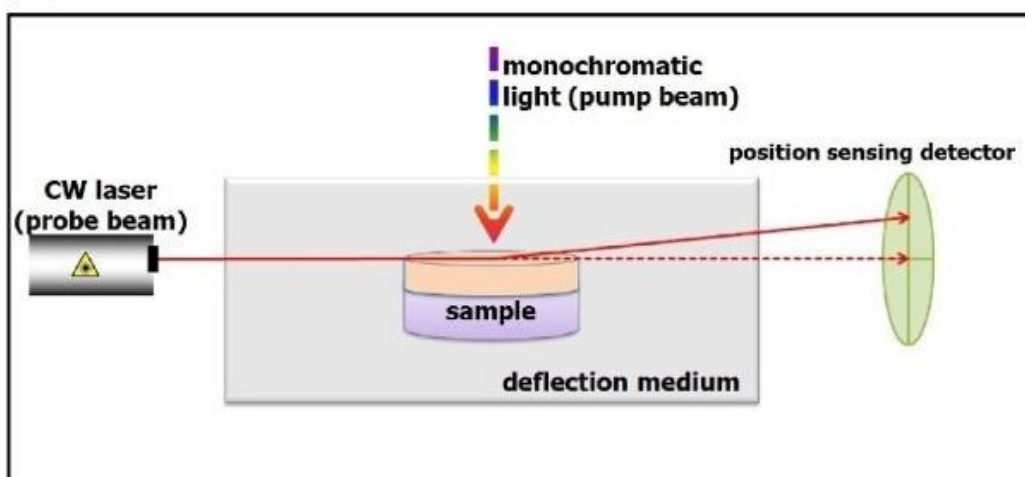

Figure 7-9: Schematic of PDS set-up.

Details of photoluminescence and lifetime measurements

7.4. Experimental Section

Time-resolved photoluminescence measurements were taken with a gated intensified CCD camera system (Andor iStar DH740 CCI-010) connected to a grating spectrometer (Andor SR303i). Excitation was performed with femtosecond laser pulses which were generated by a homebuilt setup by second order generation (SHG) in a BBO crystal from the fundamental output (pulse energy 1.55 eV, pulse length 50 fs) of a Ti:Sapphire laser system (Spectra Physics Soltstice). The laser pulses generated from the SHG had a photon energy of 3.1 eV, pulse length ~100 fs and fluence 2 $\mu J/cm^2$. Temporal resolution of the PL emission was obtained by measuring the PL from the sample by stepping the iCCD gate delay for different delays with respect to the excitation. The typical gate width was 1.5 ns. Time integrated steady state spectra were obtained by temporally averaging the emission in the detection software (exposure time 0.2 s, 5 μs gate width).

7.5   Literature

[1]   J. M. Ball, M. M. Lee, A. Hey, H. J. Snaith, *Energy Environ. Sci.* **2013**, *6*, 1739.

[2]   H. S. Kim, C. R. Lee, J. H. Im, K. B. Lee, T. Moehl, A. Marchioro, S. J. Moon, R. Humphry-Baker, J. H. Yum, J. E. Moser, *Sci. Rep.* **2012**, *2*, 591.

[3]   M. Liu, M. B. Johnston, H. J. Snaith, *Nature* **2013**, *501*, 395.

[4]   H. J. Snaith, *J. Phys. Chem. Lett.* **2013**, *4*, 3623.

[5]   M. A. Green, A. Ho-Baillie, H. J. Snaith, *Nat. Photonics* **2014**, *8*, 506.

[6]   C. Wehrenfennig, G. E. Eperon, M. B. Johnston, H. J. Snaith, L. M. Herz, *Adv. Mater.* **2014**, *26*, 1584.

[7]   G. Xing, N. Mathews, S. S. Lim, N. Yantara, X. Liu, D. Sabba, M. Grätzel, S. Mhaisalkar, T. C. Sum, *Nat. Mater.* **2014**, *13*, 476.

[8]   F. Deschler, M. Price, S. Pathak, L. E. Klintberg, D. D. Jarausch, R. Higler, S. Hüttner, T. Leijtens, S. D. Stranks, H. J. Snaith, *J. Phys. Chem. Lett.* **2014**, *5*, 1421.

[9]   J. H. Noh, S. H. Im, J. H. Heo, T. N. Mandal, S. I. Seok, *Nano Lett.* **2013**, *13*, 1764.

[10] G. E. Eperon, S. D. Stranks, C. Menelaou, M. B. Johnston, L. M. Herz, H. J. Snaith, *Energy Environ. Sci.* **2014**, *7*, 982.

[11] E. Edri, S. Kirmayer, D. Cahen, G. Hodes, *J. Phys. Chem. Lett.* **2013**, *4*, 897.

[12] E. Edri, S. Kirmayer, M. Kulbak, G. Hodes, D. Cahen, *J. Phys. Chem. Lett.* **2014**, *5*, 429.

[13] J. T. Heath, J. D. Cohen, W. N. Shafarman, D. X. Liao, A. A. Rockett, *Appl. Phys. Lett.* **2002**, *80*, 4540.

[14] S. De Wolf, J. Holovsky, S.-J. Moon, P. Löper, B. Niesen, M. Ledinsky, F.-J. Haug, J.-H. Yum, C. Ballif, *J. Phys. Chem. Lett.* **2014**, *5*, 1035.

[15] O. D. Miller, E. Yablonovitch, S. R. Kurtz, *IEEE J. Photovoltaics* **2012**, *2*, 303.

[16] A. Le Bail, H. Duroy, J. L. Fourquet, *Mater. Res. Bull.* **1988**, *23*, 447.

[17] J. Rodriguez-Carvajal, M. T. Fernandez-Diaz, J. L. Martinez, *J. Phys.: Condens. Matter* **1991**, *3*, 3215.

[18] A. Poglitsch, D. Weber, *J. Chem. Phys.* **1987**, *87*, 6373.

8 Efficient Planar Heterojunction Perovskite Solar Cells Based on Formamidinium Lead Bromide

This chapter is based on the following publication:

8.1 Introduction

Solar cells based on alkylammonium lead halide perovskites have recently garnered a large amount of interest in the photovoltaics community.[1] This class of materials exhibits a very high absorption coefficient of more than $10^4 \, \text{cm}^{-2}$ above their bandgap energy range and extremely long lifetimes of the charge carriers,[2-5] making them comparable to established inorganic solar cell materials. One possible application of these materials is in tandem solar cells with a conventional Si or CIGS bottom cell, where the latter established technologies could be improved by as much as 30 % in this configuration at almost no extra cost.[6] Moreover, building-integrated photovoltaics can also benefit from absorber materials displaying different colors, i.e. band gaps.

Recently, Eperon et al. reported on the substitution of iodide with bromide for a formamidinium-based system.[7] They observed a band gap of 2.23 eV for the resulting $FAPbBr_3$ material, which makes it a more suitable candidate for tandem applications than either $MAPbBr_3$ or $MAPbI_3$.[6] Although high efficiency $MAPbBr_3$-based solar cells have been reported by Ryu et al.,[8] their device architecture includes a high-temperature sintered titania layer, which makes them unsuitable for tandem and flexible applications. As our results show, a striking advantage of the $FAPbBr_3$ system is that it can be processed in a planar heterojunction

8.2. Results and Discussion

configuration, without a mesoporous scaffold for charge extraction. In this material, the lifetime of photoexcited species, measured via TCSPC, is long enough to enable diffusion to the charge selective contacts and therefore efficient charge separation. The fabricated devices exhibit over 6.5 mA short circuit currents (J_{sc}), a 1.35 V open circuit voltage (V_{OC}) and an overall efficiency approaching 7 %. This comparably high efficiency, in combination with its facile, low temperature processability makes FAPbBr$_3$ an ideal candidate for wide bandgap photovoltaics.

The structure of alkylammonium lead halide perovskites can be readily adjusted to tune the material's absorption and electronic properties. For example, elemental substitution of the halide can vary the material's bandgap in a range of 1.55 to 2.35 eV,[9] extend the photoexcited species lifetime[2, 10] and enhance charge transport through the layer.[10, 11] The choice of the organic cation can also strongly impact the structural parameters and therefore the performance in photovoltaic devices.[7, 12]

8.2 Results and Discussion

Here we focus on the cation exchange of methylammonium by formamidinium in lead bromide systems, resulting in the FAPbBr$_3$ perovskite structure. This material is very similar to MAPbBr$_3$, which has been widely investigated over the last years, as both compounds crystalize in the pseudocubic perovskite structure *Pm*-3*m*.[9, 11, 13]

Figure 8-1 shows the wide angle powder X-ray diffraction patterns for both materials. We have performed Rietveld analysis on these powder diffraction patterns and obtained the crystal structures shown in

Figure 8-1b. As previously reported for the MAPbBr$_3$ structure, the lead atoms are coordinated octahedrally by bromide with the organic cation sitting in the voids between the octahedra. However, due to its larger size, the FA cation spaces the PbBr$_6$ octahedra further. This increases

the lattice constant from 5.92 Å for MAPbBr$_3$ to 5.99 Å for FAPbBr$_3$. The PbBr$_6$ octahedra share one corner with their nearest neighbor, where the Pb-Br-Pb bond angle deviates from the ideal value of 180° by about 15°. This displacement is visible in the crystal structure, where for each bromide ion two of the four possible positions are shown. The tilting of the rigid PbBr$_6$ building blocks leads to a higher degree of space filling and therefore to a higher stability of the whole structure.[14, 15]
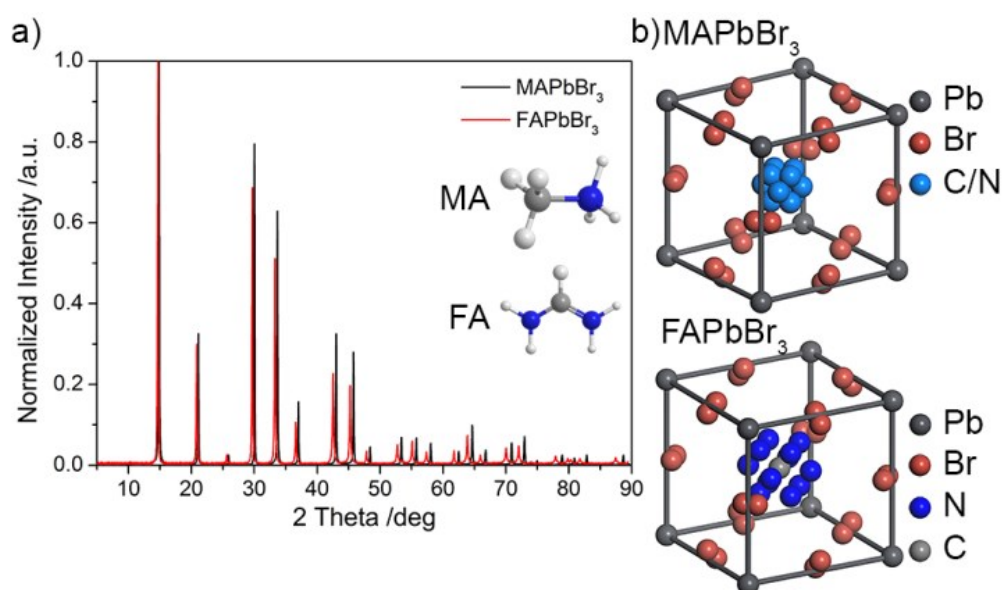

Figure 8-1: Wide angle XRD pattern of MAPbBr$_3$ and FAPbBr$_3$ (a) and refined crystal structures obtained from the XRD patterns (b). The rotation of the organic cations in the center of the unit cell is illustrated by 12 different positions for the nitrogen atoms.

While the lead and bromide ions form the stable backbone of the structure, the MA or FA ions can rotate in the center of the unit cell.[16] The position of the carbon and nitrogen atoms cannot be precisely determined, since the cation is rotating freely along and perpendicular to the C-N axis.[13] For the FAPbBr$_3$ the rotation center lies in the carbon atom, which is fixed in the center of the unit cell. The nitrogen atoms are distributed around the center in a distance of about 117 pm. The results of the Rietveld refinement, including the refined atom positions and fit parameters, are summarized in Table 8-1 and Table 8-2.

8.2. Results and Discussion

Table 8-1: Results of the Rietveld refinement of MAPbBr$_3$.

MAPbBr$_3$					
space group			*Pm*-3*m* (No.221)		
Z			1		
lattice parameter [Å]			5.923 (1)		
volume [Å^3]			207.8 (1)		
atomic parameters		*x*	*y*	*z*	*occ*
Pb	*1a*	0	0	0	1
Br	*12h*	0	0.0724 (2)	0.5	0.25
C	*12j*	0.4143 (4)	0.4143 (4)	0.5	0.0833
N	*12j*	0.5857 (4)	0.5857 (4)	0.5	0.0833
U_{iso} [pm^2]		**Pb**		301 (2)	
		Br		241 (4)	
			C/N not refined		
R_{wp} / R_p			2.747/2.036		
χ^2 / R_{Bragg}			1.930/2.916		

Table 8-2: Results of the Rietveld refinement of FAPbBr$_3$.

FAPbBr$_3$					
space group			*Pm*-3*m* (No.221)		
Z			1		
lattice parameter [Å]			5.992 (1)		
volume [Å^3]			215.2 (1)		
atomic parameters		*x*	*y*	*z*	*occ*
Pb	*1a*	0	0	0	1
Br	*12h*	0	0.0617 (3)	0.5	0.25
C	*1b*	0.5	0.5	0.5	1
N	*12j*	0.3633 (5)	0.3633 (5)	0.5	
U_{iso} [pm^2]		**Pb**		403 (3)	
		Br		286 (6)	
			C/N not refined		
R_{wp} / R_p			3.198/2.287		
χ^2 / R_{Bragg}			2.115/2.342		

The SEM micrographs in Figure 8-2a and b show the high surface coverage of the prepared perovskite layers. The top-view images show a dense layer with no gaps and occasional larger crystals, which appear lighter in the micrograph. The same can be seen from the cross section images in Figure 8-2c, where the perovskite layer uniformly coats the FTO substrate, without any dips or pinholes. It has been shown previously that a high degree of film coverage is beneficial for light absorption of the perovskite layers and is a requirement for efficiently working solar cells.[17, 18] We have recently demonstrated that in the case of the methylammonium lead iodide perovskite, a high surface coverage can be achieved with a solution deposition-conversion technique.[10] Here, the prepared $MAPbBr_3$ and $FAPbBr_3$ films consist of crystallites ranging from several tens to hundreds of nanometers in size. After the conversion, the film thickness is approximately 400 nm, as can be estimated from the cross section images in Figure 2c, and complete surface coverage is achieved.
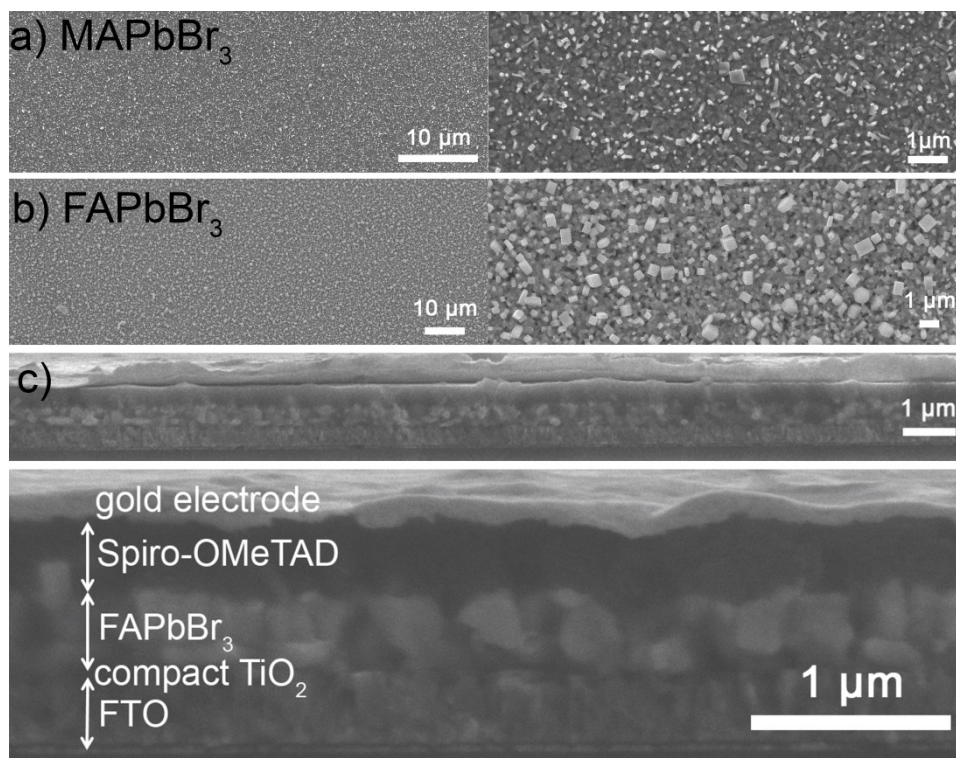

Figure 8-2: SEM top view micrographs of MAPbBr₃ (a) and FAPbBr₃ (b) films. Below: cross section of a FAPbBr₃ film on a compact TiO₂ blocking layer, covered with Spiro-OMeTAD and a gold electrode(c).

8.2. Results and Discussion

We have prepared solar cells based on these materials according to a previously reported layout.[19] In short, FTO-coated glass slides were covered with a non-porous TiO_2 layer as the electron selective contact. Over this layer, the $MAPbBr_3$ or $FAPbBr_3$ layer was deposited via a deposition/conversion approach.[10, 20] Firstly, a $PbBr_2$ film was deposited via spin-coating and was then immersed in MABr or FABr solutions in 2-propanol, respectively. The state-of-the-art p-type hole transporter spiro-OMeTAD was then deposited by spin-coating from chlorobenzene and the whole device was contacted with thermally evaporated gold electrodes under high vacuum. A scheme of the solar cell layout and the energy levels of the used materials are displayed in Figure 8-3a and b. The energy levels of $FAPbBr_3$ were obtained through ultraviolet photoelectron spectroscopy (UPS). The obtained spectra are depicted in Figure 8-4. The current voltage curves obtained for both types of materials are displayed in Figure 8-3c.
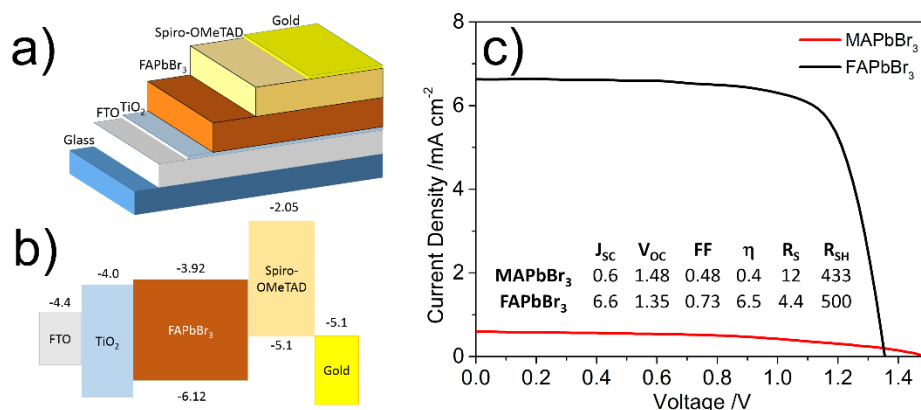

Figure 8-3: Schematic display of the prepared solar cell layout (a) and energy levels for all layers (b). The HOMO and LUMO levels for $FAPbBr_3$ were determined by ultraviolet photoelectron spectroscopy (UPS). J-V curves under AM 1.5 solar irradiation conditions for both $MAPbBr_3$ (red) and $FAPbBr_3$ (black) -based solar cells (c). The inset table summarizes the photovoltaic parameters (short circuit current, J_{SC} (mAcm^{-2}); open circuit voltage, V_{OC} (V); fill factor, FF; power conversion efficiency, η, series resistance, R_S (Ohm cm^2) and shunt resistance, R_{SH} (Ohm cm^2)).

The $MAPbBr_3$ solar cells show a very high open circuit voltage of 1.5 V, matching previously reported record values. Both, the short circuit current and fill factor, however, are low, compared to the theoretical maximum, resulting in a power conversion efficiency of only 0.4 %. The $FAPbBr_3$ devices, on the other hand, exhibit high short circuit currents of over 6.5 mA and

a fill factor exceeding 70 %. Additionally the $FAPbBr_3$ devices exhibit lower series resistance compared to the $MAPbBr_3$ devices and also highly efficient $MAPbI_3$ prepared in a similar way in our laboratory.[10] This compensates for the slightly lower voltage of 1.35 V and results in an overall power conversion efficiency of 6.5 %. Statistics on a batch of 36 solar cells are depicted in Figure S4. We can attribute the lower voltage to the narrower band gap of the $FAPbBr_3$ of 2.26 eV compared to 2.34 eV for the MA compound. We note here that the open circuit voltage of the devices is limited to a large extent by the use of spiro-OMeTAD, which exhibits a HOMO level of 5.1 eV. This energy level is optimum for the $MAPbI_3$ perovskite, but in the systems presented here, this results in a rather large voltage loss. Hence, before high voltage perovskite solar cells can be achieved, new hole transporting materials need to be developed. A step in this direction was presented in recent work by Ryu et al., where high performance devices based on the $MAPbBr_3$ perovskite were prepared by employing various triarylamine polymers.[8] However, the voltages in that study were still low and further progress is required.
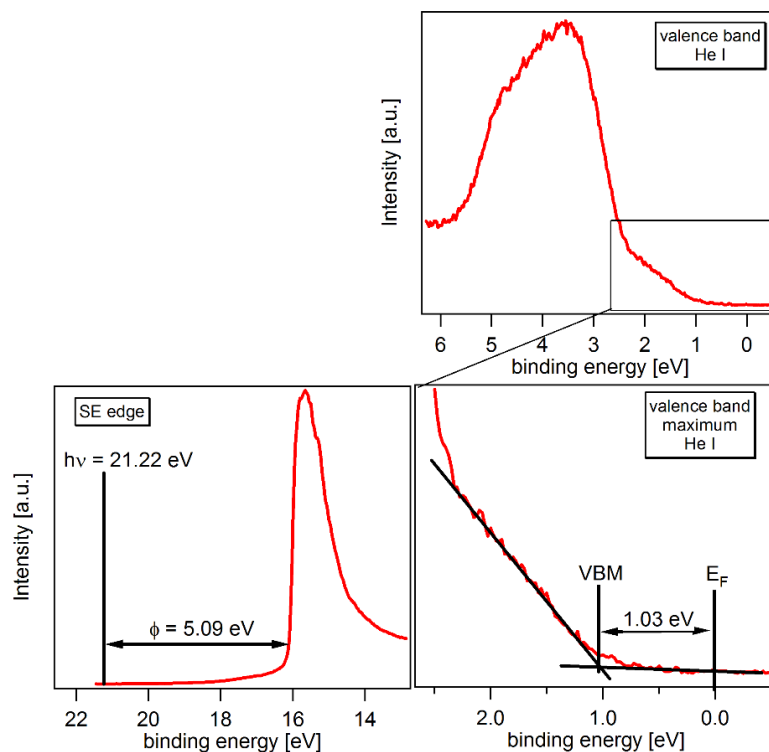
Figure 8-4: XPS spectra obtained for FAPbBr₃. The graph on the left describes the Fermi level E_F relative to vacuum. The images on the right show the energetic position of the valence band relative to the Fermi level E_F.

In order to understand the differences in short circuit current, the light absorption of both materials was studied. The UV-Vis absorbance spectrum for FAPbBr$_3$ in Figure 8-5a shows a very steep increase of absorbance at the band edge and an excitonic feature centered on 532 nm. The absorption band onset and the photoluminescence signal at 550 nm are overlapping, indicating that there is no significant vibronic relaxation and therefore no sub-band gap states in the material.[2] The optical band gap of the prepared structure is estimated to be 2.26 eV by a Tauc plot (Figure 8-6). For the MAPbBr$_3$ system the absorption onset and PL are shifted 10 nm to shorter wavelengths as compared with the MA system. Both materials show comparable absorption coefficients for energies higher than the band gap, and both prepared films absorb over 90 % of the incident light. We calculated the maximum achievable short circuit current for solar cells prepared from both materials by integrating the absorption spectra with the AM1.5G solar spectrum to be 9.0 mA cm^{-2} for FA based films and 7.5 mA cm^{-2} for

the MA system. Therefore, the substantial differences in short circuit current in the devices cannot be explained by light absorption differences.
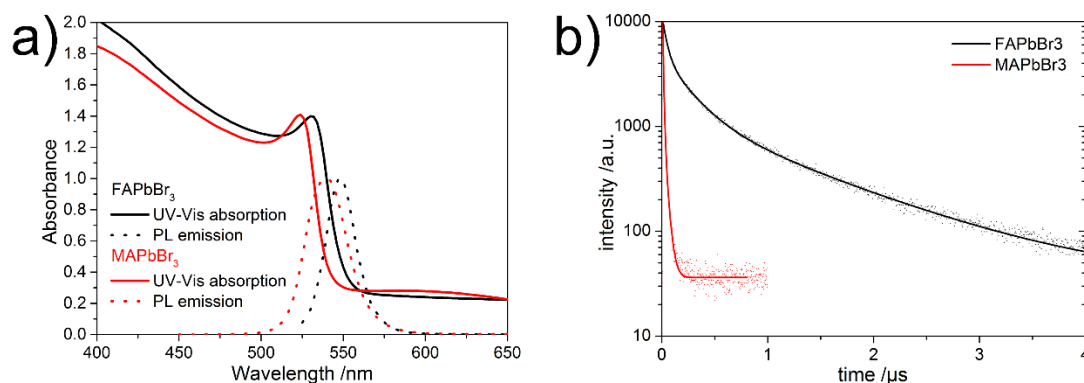

Figure 8-5: (a) UV-Vis absorption in transmission and PL emission spectra for 400 nm thick FAPbBr$_3$ (black) and MAPbBr$_3$ (red) films. (b) Photoluminescence (PL) decay curves for FAPbBr$_3$ and MAPbBr$_3$. The samples were illuminated at 510 nm with a pump fluence of ~0.3 μJcm^{-2}; the emission was monitored at the maximum of the PL emission at 548 nm for FAPbBr$_3$ and at 540 nm for MAPbBr$_3$.

It is possible that the device photocurrent in MAPbBr$_3$ is limited by insufficient charge collection. It has recently been shown that measurements of photoluminescence (PL) dynamics yield important information about the diffusion length of the photoexcited species in the devices, with longer PL lifetimes indirectly indicating longer charge diffusion lengths.[2, 3] We show such data in Figure 8-5b. The FAPbBr$_3$ films show an unusually long decay lifetime τ_e of about 200 ns, much slower than the lifetime exhibited by MAPbBr$_3$ films (17 ns). Stranks et al. attribute a comparable lifetime for the MAPbI$_{3-x}$Cl$_x$ perovskite to a free diffusion length of electrons and holes of more than 1 μm.[2] In contrast, the MAPbBr$_3$ variant exhibits a similar lifetime to that of the non-Cl treated MAPbI$_3$ perovskite, and therefore diffusion lengths closer to ~100 nm.[2, 3] It is not clear at this point why the FA-based perovskite exhibits longer diffusion lengths than the MA variant, as both crystallize in the same crystal phase and only minor differences in the size of the unit cell exist. While differences in the nature and behavior of the cations, be it limited cation rotation or a smaller dipole moment,[21] could certainly play a role. It has also been shown recently that processing conditions,[10] crystal quality and orientation

8.2. Results and Discussion

can significantly influence the electronic properties of the final devices.[22] More experiments to clarify this aspect are currently under way.
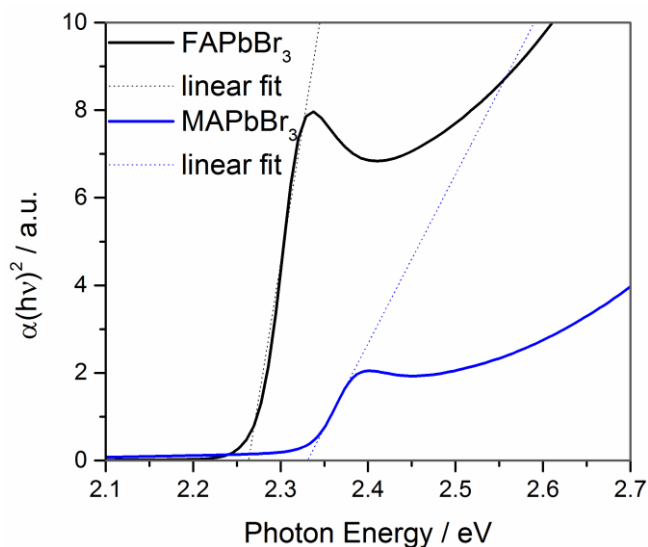

Figure 8-6: Tauc plot for FAPbBr₃ and MAPbBr₃. The estimated band gaps are 2.26 eV and 2.34 eV, respectively.

Our results are consistent with the recent report by Ryu et al., who showed high short circuit currents for devices based on the MAPbBr₃ material.[8] In their study, the short diffusion length of the MA-based perovskite was overcome by the use of a mesoporous TiO_2 scaffold. In this case, due to the interpenetrating nature of the titania framework and the perovskite material, efficient charge collection was possible as charges only need to travel the pore diameter (typically under 30 nm) in order to be collected.[2-4] In our study, however, the MAPbBr₃ perovskite was deposited in a planar configuration and therefore the photoexcited species must travel the whole thickness of the film (>400 nm) in order to be collected. Since the diffusion length is shorter than the thickness of the film, we can conclude that poor charge collection limits the photocurrent in this system. This is not the case for the FA-based perovskite, which works efficiently even without a high temperature sintered titania scaffold. This is particularly important in order to integrate the perovskite technology into tandem devices with inorganic

bottom cells or flexible applications, neither of which can sustain heating processes above 150 C. Additionally, the FA-based perovskites show favorable chemical stability, where the photovoltaic performance of the devices improved by over 50% after storage in the dark in a desiccator for over 72 hours. Additionally, we have performed thermogravimetric measurements on both MA- and FA-based perovskites as shown in Figure 8-7. We can clearly observe a shift of +50 degrees for the decomposition onset, clearly indicating that the FA perovskite is more thermally stable than both $MAPbBr_3$ and $MAPbI_3$. Since solar cells under real working conditions will usually heat up to over 60 degrees during the course of the day,[23] high thermal stability is likely to extend the long-term stability of perovskite solar cells fabricated from formamidinium variants.
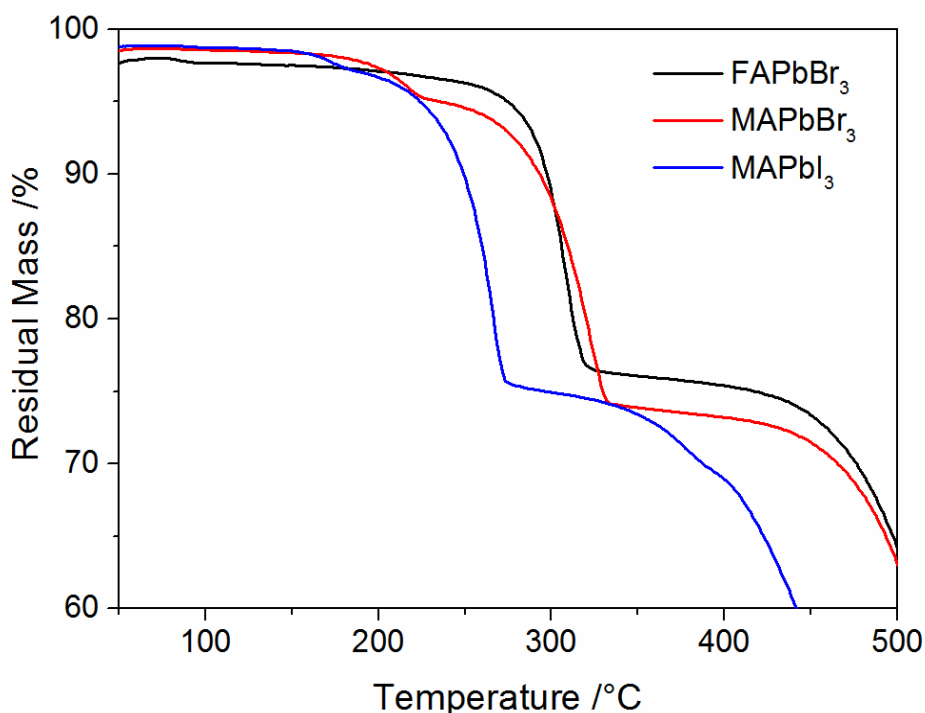

Figure 8-7: Thermogravimetric analysis (TGA) of MA and FAPbBr₃. For comparison we include the TGA for the literature known methylammonium lead iodide perovskite.

8.3   Conclusion

We have studied the novel wide bandgap perovskite material FAPbBr$_3$ and fully characterized its crystal structure as well as optical and electronic properties. We have shown that FAPbBr$_3$ can achieve for the first time high power conversion efficiencies of up to 7 % in a planar heterojunction architecture, without the need for a mesoporous scaffold. Our results show that devices fabricated from MAPbBr$_3$ in the same configuration are charge collection limited, while the formamidinium variant exhibits diffusion lengths that are orders of magnitude longer, and therefore is able to achieve a high charge collection efficiency. Additionally, we have performed thermogravimetric analysis and find that the FA variant exhibits a shift of +50 degrees in the decomposition onset, showcasing the higher stability of this system. This renders the FAPbBr$_3$ system suitable as the absorber for flexible photovoltaic applications as well as the top cell in a tandem configuration with a commercially available silicon or CIGS bottom cell.

8.4   Experimental Section

Preparation of the precursors

Methylammonium bromide was prepared by adapting a recipe published earlier.[24] In short, 24 mL of methylamine solution (33 % in ethanol) was diluted with 100 mL of absolute ethanol in a 250 mL roundbottom flask. To this solution, 8 mL of an aqueous solution of hydrobromic acid (48 wt%) was added under constant stirring. After a reaction time of one hour at room temperature, the solvents were removed by rotary evaporation. The obtained white solid was washed with dry diethyl ether and finally recrystallized from ethanol.

Formamidinium bromide was synthesized following a known procedure.[7] Formamidinium acetate was dissolved in a double molar excess of aqueous HBr (48 wt%), and stirred at 50 °C

for 60 minutes. The solvent and remaining HBr was removed by rotary evaporation to obtain a slightly yellow powder. Washing with dry diethyl ether and recrystallization from ethanol led to the white, crystalline product.

Solar cell preparation

Fluorine doped tin oxide (FTO) coated glass sheets (15 Ω/sq, Dyesol Italy) were patterned by etching with zinc powder and 3 M HCl. They were subsequently cleaned with a 2 % Hellmanex solution and rinsed with de-ionized water, acetone and ethanol. Directly before applying the blocking layer, last organic residues were removed by an oxygen plasma treatment for 5 minutes. The dense TiO_2 layer was prepared from a sol-gel precursor solution by spin-coating onto the substrates and calcining at 500 °C in air.[19] For the sol-gel solution a 27.2 mM solution of HCl in 2-propanol was added dropwise to a vigorously stirred 0.43 mM solution of titanium isopropoxide in 2-propanol. The solution stayed clear during the addition and was discarded otherwise.

An approximately 250 nm thick layer of $PbBr_2$ was prepared by spin-coating 75 µL of a 1 M $PbBr_2$ solution in dry *N*,*N*-Dimethylformamide (DMF) onto the TiO_2 covered substrates at 2000 RPM for 15 seconds. To obtain smooth, homogeneous layers it was important to heat both, the $PbBr_2$ solution and the substrate, to 60 °C before spin-coating and to perform the deposition dynamically with hot solution onto the hot substrate.

The lead bromide layer was transformed into either the $MAPbBr_3$ or $FAPbBr_3$ perovskite by immersing it into a 20 mM solution of either MABr or FABr in isopropanol respectively. For the $MAPbBr_3$ perovskite, the $PbBr_2$ coated substrates were immersed into 40 mL of the solution, which was heated to 60 °C for 5 minutes. For $FAPbBr_3$ the solution had to be heated

to 70 °C and the immersion was performed for 30 minutes. After taking the films out of the solution, they were rinsed in an isopropanol bath and carefully dried in a nitrogen stream.

Afterwards, the films were covered with a 400 nm layer of Spiro-OMeTAD (Borun Chemicals, 99.1 % purity) "spiro". 75 mg of spiro were dissolved in 1 mL of chlorobenzene and mixed with 10 mL 4-*tert*-Butylpyridine (*t*BP) and 30 μL of a 170 mg mL^{-1} bis(trifluoromethane)sulfonimide lithium salt (LiTFSI) solution in acetonitrile. This solution was spin-coated dynamically at 800 RPM for 45 seconds. In a second step the sample rotation was accelerated to 2000 RPM for 5 seconds to allow the solvent to dry completely. Before evaporating the gold electrodes, Spiro-OMeTAD was left to oxidize in air over night at room temperature and 15 – 20 % rel. humidity.

PL sample preparation

Perovskite samples for steady state and time resolved PL measurements were prepared as described for the solar cell preparation. In this case non-conductive glass substrates were used and the perovskite was covered with a poly(methyl methacrylate) (PMMA) layer to prevent degradation by ambient moisture. The layer was deposited by spin coating 75 μL of a 10 mg mL^{-1} solution of PMMA in chlorobenzene at 1000 RPM for 45 seconds.

Characterization details:

J-V curves were recorded with a Keithley 2400 sourcemeter under simulated AM 1.5 sunlight, calibrated to 100 mW cm^{-2} with a Fraunhofer ISE certified silicon cell. The active area of the solar cells was defined with a square metal aperture mask of 0.0831 cm^2.

Steady-state absorption spectra were acquired with a Lambda 1050 UV/Vis spectrophotometer (Perkin Elmer) using an integrating sphere.

Steady state and time resolved PL measurements were performed with a Fluotime 300 Spectrofluorometer (Picoquant GmbH). The excitation wavelength was fixed at 510 nm. The emission for time resolved measurements was monitored at the maximum intensity of the steady state photo emission.

Scanning electron microscopy (SEM) images were obtained using a Jeol JSM-6500F microscope equipped with a secondary electron detector.

Samples for powder XRD measurements were obtained by preparing perovskite films on glass substrates following the procedure described for solar cells and removing them from the glass. The measurements were performed on a Huber Imaging Plate Guinier Diffractometer G670 (Cu-$K_{\alpha 1}$-radiation). Rietveld refinement was performed using the Bruker TOPAS package.[25] The refinements are based on a structure published by Mashiyama et al.[16] To describe the rotation of methylammonium in MAPbBr$_3$, the nitrogen and carbon atoms were displaced around the center of the unit cell. For FAPbBr$_3$, the carbon atom was placed in the center of the unit cell and the nitrogen atoms were dislocated around it. As a consequence of the fast rotation of the organic cation, the U_{iso} of C and N was restrained in both cases.

The photoelectron spectroscopy experiments were performed using an Escalab 250 spectrometer equipped with a monochromatized Al anode X-ray source (hv = 1486.6 eV), and a helium discharge lamp (hv = 21.2 eV) as excitation sources for X-ray photoelectron spectroscopy (XPS) and UV photoelectron spectroscopy (UPS), respectively. The energetic resolution determined by the 2σ Gaussian broadening used to fit the Fermi edge of a freshly sputter-cleaned silver sample measured at room temperature is 0.35 eV for XPS and 0.13 eV for UPS. All spectra are referenced in binding energy to the Fermi level. The core level lines of in-situ cleaned Au, Ag and Cu metal foils were used to calibrate the XPS binding energy scale.

8.5 Literature

[1] H. J. Snaith, *J. Phys. Chem. Lett.* **2013**, *4*, 3623.

[2] S. D. Stranks, G. E. Eperon, G. Grancini, C. Menelaou, M. J. P. Alcocer, T. Leijtens, L. M. Herz, A. Petrozza, H. J. Snaith, *Science* **2013**, *342*, 341.

[3] G. Xing, N. Mathews, S. Sun, S. S. Lim, Y. M. Lam, M. Grätzel, S. Mhaisalkar, T. C. Sum, *Science* **2013**, *342*, 344.

[4] C. Wehrenfennig, M. Liu, H. J. Snaith, M. B. Johnston, I. Herz, *Energy Environ. Sci.* **2014**, *7*, 2269.

[5] S. De Wolf, J. Holovsky, S.-J. Moon, P. Löper, B. Niesen, M. Ledinsky, F.-J. Haug, J.-H. Yum, C. Ballif, *J. Phys. Chem. Lett.* **2014**, *5*, 1035.

[6] Z. M. Beiley, M. D. McGehee, *Energy Environ. Sci.* **2012**, *5*, 9173.

[7] G. E. Eperon, S. D. Stranks, C. Menelaou, M. B. Johnston, L. M. Herz, H. J. Snaith, *Energy Environ. Sci.* **2014**, *7*, 982.

[8] S. Ryu, J. H. Noh, N. J. Jeon, Y. C. Kim, W. S. Yang, J. W. Seo, S. I. Seok, *Energy Environ. Sci.* **2014**, *7*, 2614.

[9] J. H. Noh, S. H. Im, J. H. Heo, T. N. Mandal, S. I. Seok, *Nano Lett.* **2013**, *13*, 1764.

[10] P. Docampo, F. Hanusch, S. D. Stranks, M. Döblinger, J. M. Feckl, M. Ehrensperger, N. K. Minar, M. B. Johnston, H. J. Snaith, T. Bein, *Advanced Energy Materials* **2014**.

[11] E. Edri, S. Kirmayer, M. Kulbak, G. Hodes, D. Cahen, *J. Phys. Chem. Lett.* **2014**, *5*, 429.

[12] K. Liang, D. B. Mitzi, M. T. Prikas, *Chem. Mater.* **1998**, *10*, 403.

[13] R. Wasylishen, O. Knop, J. Macdonald, *Solid State Commun.* **1985**, *56*, 581.

[14] A. M. Glazer, *Acta Crystallogr., Sect. B* **1972**, *28*, 3384.

[15] A. Poglitsch, D. Weber, *J. Chem. Phys.* **1987**, *87*, 6373.

[16] H. Mashiyama, Y. Kurihara, T. Azetsu, *J. Korean Phys. Soc* **1998**, *32*, 156.

[17] G. E. Eperon, V. M. Burlakov, P. Docampo, A. Goriely, H. J. Snaith, *Adv. Funct. Mater.* **2014**, *24*, 151.

[18] P. Docampo, J. M. Ball, M. Darwich, G. E. Eperon, H. J. Snaith, *Nat Commun* **2013**, *4*, 2761.

[19] J. M. Ball, M. M. Lee, A. Hey, H. J. Snaith, *Energy Environ. Sci.* **2013**, *6*, 1739.

[20] J. Burschka, N. Pellet, S.-J. Moon, R. Humphry-Baker, P. Gao, M. K. Nazeeruddin, M. Grätzel, *Nature* **2013**, *499*, 316.

[21]   J. M. Frost, K. T. Butler, F. Brivio, C. H. Hendon, M. van Schilfgaarde, A. Walsh, *Nano Lett.* **2014**, *14*, 2584.

[22]   M. Saliba, K. W. Tan, H. Sai, D. T. Moore, T. Scott, W. Zhang, L. A. Estroff, U. Wiesner, H. J. Snaith, *The Journal of Physical Chemistry C* **2014**.

[23]   N. Kato, Y. Takeda, K. Higuchi, A. Takeichi, E. Sudo, H. Tanaka, T. Motohiro, T. Sano, T. Toyoda, *Sol. Energy Mater. Sol. Cells* **2009**, *93*, 893.

[24]   H. S. Kim, C. R. Lee, J. H. Im, K. B. Lee, T. Moehl, A. Marchioro, S. J. Moon, R. Humphry-Baker, J. H. Yum, J. E. Moser, M. Gratzel, N. G. Park, *Scientific Reports* **2012**, *2*.

[25]   R. Cheary, A. Coelho, J. Cline, *J. Res. Natl. Inst. Stand. Technol.* **2004**, *109*, 1.

9 Bright Light-Emitting Diodes based on Organometal Halide Perovskite

9.1 Introduction

Recent reports on earth-abundant organometal halide based perovskite for high efficiency photovoltaics have demonstrated this class of materials to be excellent semiconductors for optoelectronic devices.[1-7] Their primary advantages lie in the fact that they can be very easily solution processed, require no high temperature heating steps, and they possess an optical bandgap which is tunable in the visible to infrared regions,[8, 9] making them very attractive materials for use in low-cost and large area optoelectronic applications. Previous works have shown these perovskites to possess strong photoluminescent properties,[10, 11] hence making them potential candidates for use in light-emitting devices. There were previous attempts to fabricate light-emitting devices using related perovskite materials.[12-14] However, electroluminescence could only be achieved at liquid nitrogen temperatures, rendering those devices impractical for applications. In this work, we demonstrate the first high brightness near-infrared, green and red electroluminescence from solution-processed organometal halide perovskites, using both a standard and an inverted device architecture. All electroluminescence and device characteristics were measured in air at room temperature. We refer to electron injection from the transparent conductive electrode as the standard structure and hole injection from the transparent electrode as the inverted structure, following the convention in perovskite and dye-sensitized photovoltaics.

9.2 Results and Discussion

In our infrared PeLED, we use a simple 3-layered structure of $TiO_2/CH_3NH_3PbI_{3-x}Cl_x/F8$, sandwiched between indium tin oxide (ITO) and MoO_3/Ag as cathode and anode respectively (see Figure 9-1). We designed the perovskite to be placed between two large bandgap semiconductors, in a double heterostructure architecture, so as to confine injected charges for better light emission. A thin (25 nm) layer of TiO_2 was deposited using atomic layer deposition (ALD) onto an ITO coated glass substrate. The TiO_2 serves as an efficient electron injector, as well as a hole blocking layer for the perovskite device. A thin layer of perovskite precursor was deposited on the TiO_2 by spin coating. Annealing at 100 °C converts the precursor into a 15 nm $CH_3NH_3PbI_{3-x}Cl_x$ perovskite thin film (see Figure 9-1b for perovskite structure). The perovskite layer was designed to be thin in order to spatially confine electrons and holes for bimolecular recombination. Given the small exciton binding energy in this class of materials,[5, 15, 16] the confinement of injected charges within a thin "well" enhances electron-hole capture and improves radiative recombination. The perovskite film was capped with a 50 nm layer of F8 polymer by spin-coating from solution. The F8 polymer layer, with a deep ionization potential and a shallow electron affinity, was chosen to form a type-I heterojunction with the perovskite (see Figure 9-1c for energy level diagram). This allows holes to be confined within the perovskite well and electrons to be blocked from exiting via the anode. A high work function MoO_3/Ag anode was used to provide ohmic hole injection into the F8 polymer.[17] The ionization potentials of the materials are estimated from values in the literature,[18, 19] and the electron affinity values are estimated based on the optical bandgap of the materials.
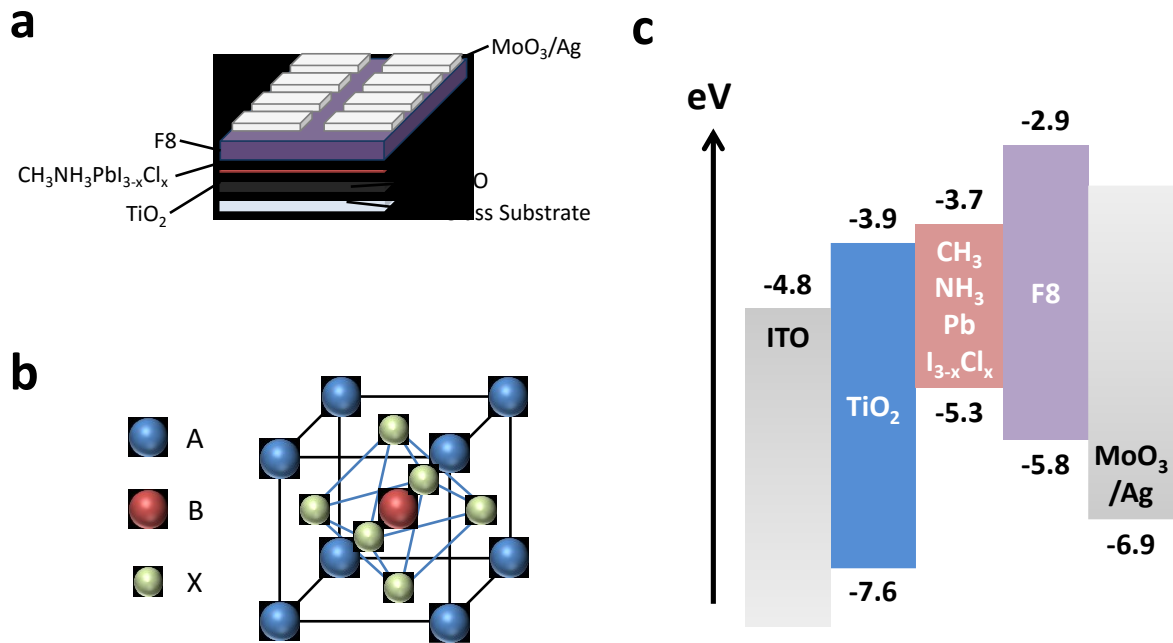
Figure 9-1: (a) Device architecture of CH₃NH₃PbI₃₋ₓClₓ perovskite light-emitting diode (PeLED). (b) Single unit-cell of an ABX₃ perovskite crystal, where A is methylammonium, B is Pb and X is I, Br or Cl. (c) Energy level diagram of different layers of materials in the infrared PeLED, showing conduction and valence band levels with respect to vacuum.

The optical absorption and emission spectra of the $CH_3NH_3PbI_{3-x}Cl_x$ perovskite thin film are shown in Figure 9-2. Absorption onset occurs at approximately 780 nm, consistent with previous reports.[1] The non-zero baseline in the absorption spectra can be attributed to light scattering and interference effects, since we measure a clear absorption edge in photothermal deflection spectroscopy (PDS), which is a technique immune to optical scattering artifacts (see Figure 9-3). A strong near-infrared photoluminescence (PL), centered at 773 nm, was measured when the perovskite thin film was excited with a 532 nm green cw-laser. Using the integrating sphere method,[20] we measured a relatively high photoluminescence quantum efficiency (PLQE) of 26 %. The electroluminescence (EL) of the infrared PeLED is slightly blue shifted from the PL, peaking at 754 nm. The emission band is narrow with a full width at half maximum (FWHM) of 35 nm. No electroluminescence was observed from the F8 polymer, indicating that F8 serves only as a hole transporting and an electron blocking layer, and does not participate in light emission.

9.2. Results and Discussion
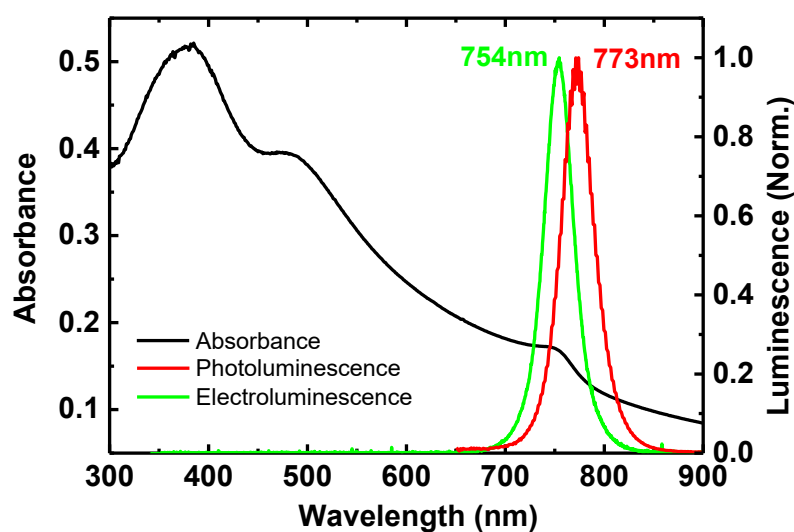
Figure 9-2. Absorbance (left y-axis), electroluminescence and photoluminescence (right y-axis) spectra of $CH_3NH_3PbI_{3-x}Cl_x$ perovskite.
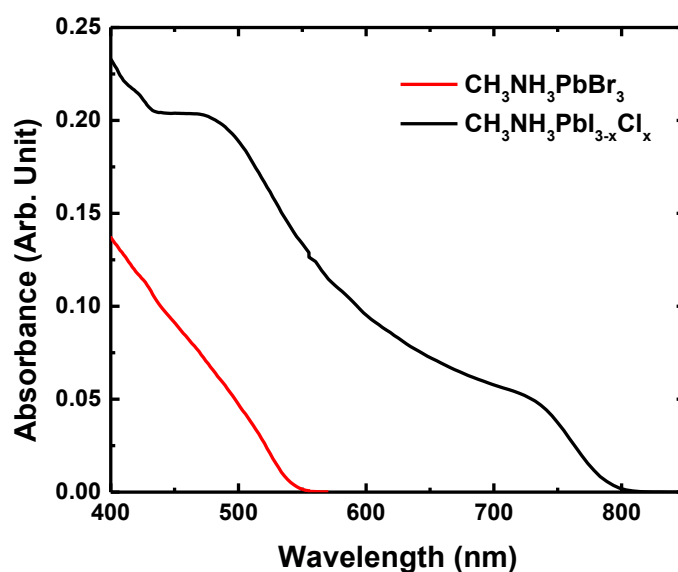
**Figure 9-3:** Photothermal deflection spectroscopy (PDS) of $CH_3NH_3PbI_{3-x}Cl_x$ and $CH_3NH_3PbBr_3$ perovskite thin films on fused silica substrate, showing the clear absorption edges of the materials.

The current density *vs.* voltage characteristics and the corresponding radiance of the infrared PeLED is shown in Figure 9-4a. A clear turn-on of light emission was observed at 1.5 V, close to the photon emission energy. A radiance of 6.8 W sr^{-1} m^{-2} was achieved at a driving voltage of 6.2 V, where the corresponding current density was 605 mA cm^{-2}. The highest external

quantum efficiency (EQE) of 0.23 % was achieved at 494 mA cm^{-2}, calculated assuming a Lambertian emission profile. This gives an internal quantum efficiency (IQE) of 1.0 %, calculated using the relation IQE = 2n^2 EQE.[21] We selected the refractive index of glass (n = 1.5) to estimate IQE because we consider light to be emitted isotropically into the glass substrate, given the thinness ($<< \lambda$) of our emissive perovskite layer. The EQE in our devices rises with increasing voltage and current density, indicating that a high density of charges is required for efficient radiative recombination.

To investigate the reasons for the decline in radiance and efficiency at higher current densities, we turned to pulse voltage measurements where a bias as high as 14 V was applied to drive currents up to 1500 mA cm^{-2} (see Figure 9-4b). Using 14 V square voltage pulses at a width of 1 ms and frequency of 100 Hz, we achieved a two-times higher radiance of 13.1 W sr^{-1} m^{-2} at a current density of 1467 mA cm^{-2}. This indicates that the device degradation and efficiency drop-off are driven by heating at high current densities since a higher radiance could be achieved when the device is given time to cool in between the pulses.
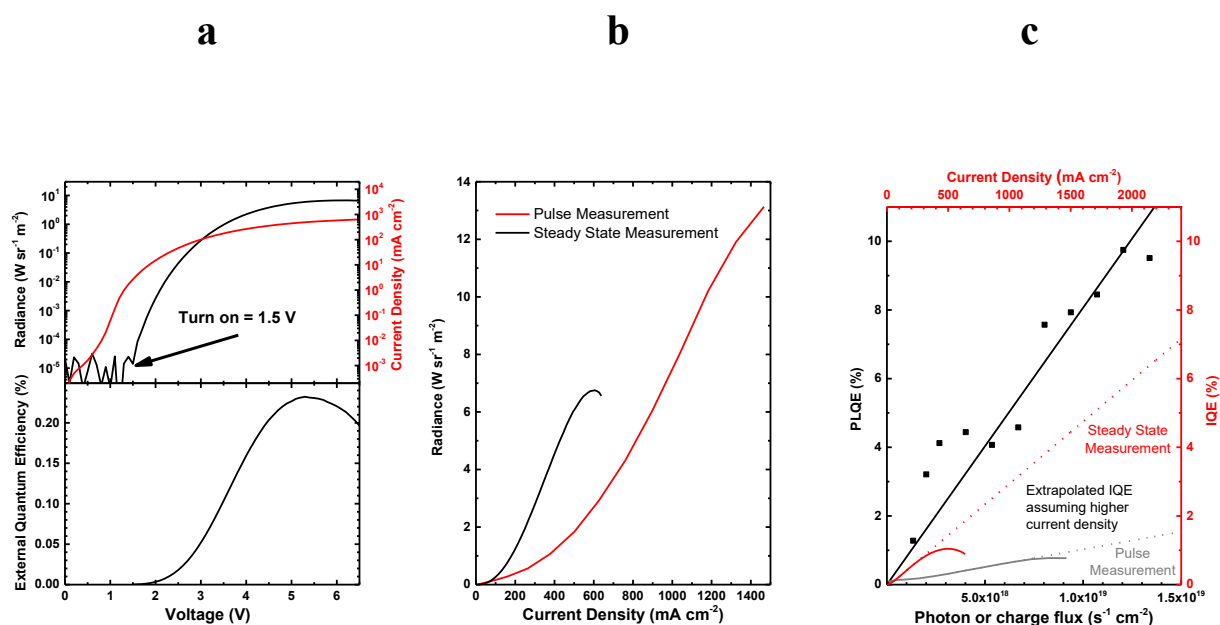

Figure 9-4. (a) Top graph: Combined radiance (black line) and current density (red line) vs. voltage characteristics of the infrared PeLED. Bottom graph: External quantum efficiency vs. voltage of PeLED.

9.2. Results and Discussion

(b) Radiance vs. current density of PeLED under steady state and pulse measurement conditions. For pulse measurement, 1 ms square voltage pulses were applied at a frequency of 100 Hz. (c) Photoluminescence quantum efficiency (PLQE) (black line) of TiO$_2$/CH$_3$NH$_3$PbI$_{3-x}$Cl$_x$/F8 film as a function of absorbed (~15%) photon flux. Internal quantum efficiency (IQE) (right axis) of PeLED is plotted against current density and extrapolated as comparison to PLQE. Red line represents device in steady state measurement and grey line represents device in pulse measurement.

Interestingly, we observed during our pulse experiments that the radiance and quantum efficiency of the PeLED increase across the duration of the voltage pulse, while the current density remains approximately constant (see Figure 9-5).
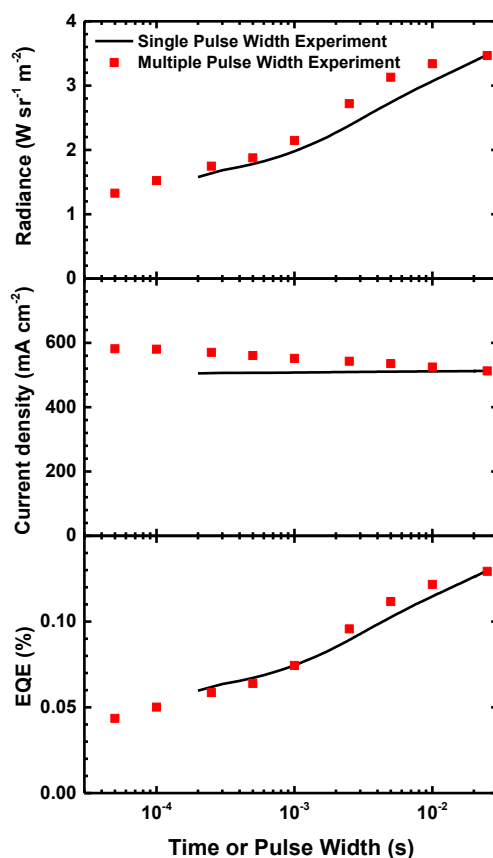

Figure 9-5: Plots of radiance, current density and external quantum efficiency vs. time (or pulse width) for the CH$_3$NH$_3$PbI$_{3-x}$Cl$_x$ PeLED at a driving voltage of 7 V. In the single pulse width experiment, 25 ms square voltage pulses with a period of 250 ms were applied and the radiance and current density were monitored over the duration of the 25 ms pulse. For the multiple pulse width experiment, square pulses with widths ranging from 50 μs to 25 ms were applied to the device, all with periods of 10X pulse width. Both experiments show that radiance and EQE increase with the pulse width while current density remains approximately constant.

We show, in Figure 9-6, that this increase in light-emitting efficiency is related to the history of electric field polarization across the device. In our experiments, a device which is pre-polarized with an external bias emits at a higher radiance and efficiency. Over the duration of the voltage pulse, the perovskite device becomes increasingly polarized, hence giving higher electroluminescence with longer pulse durations.
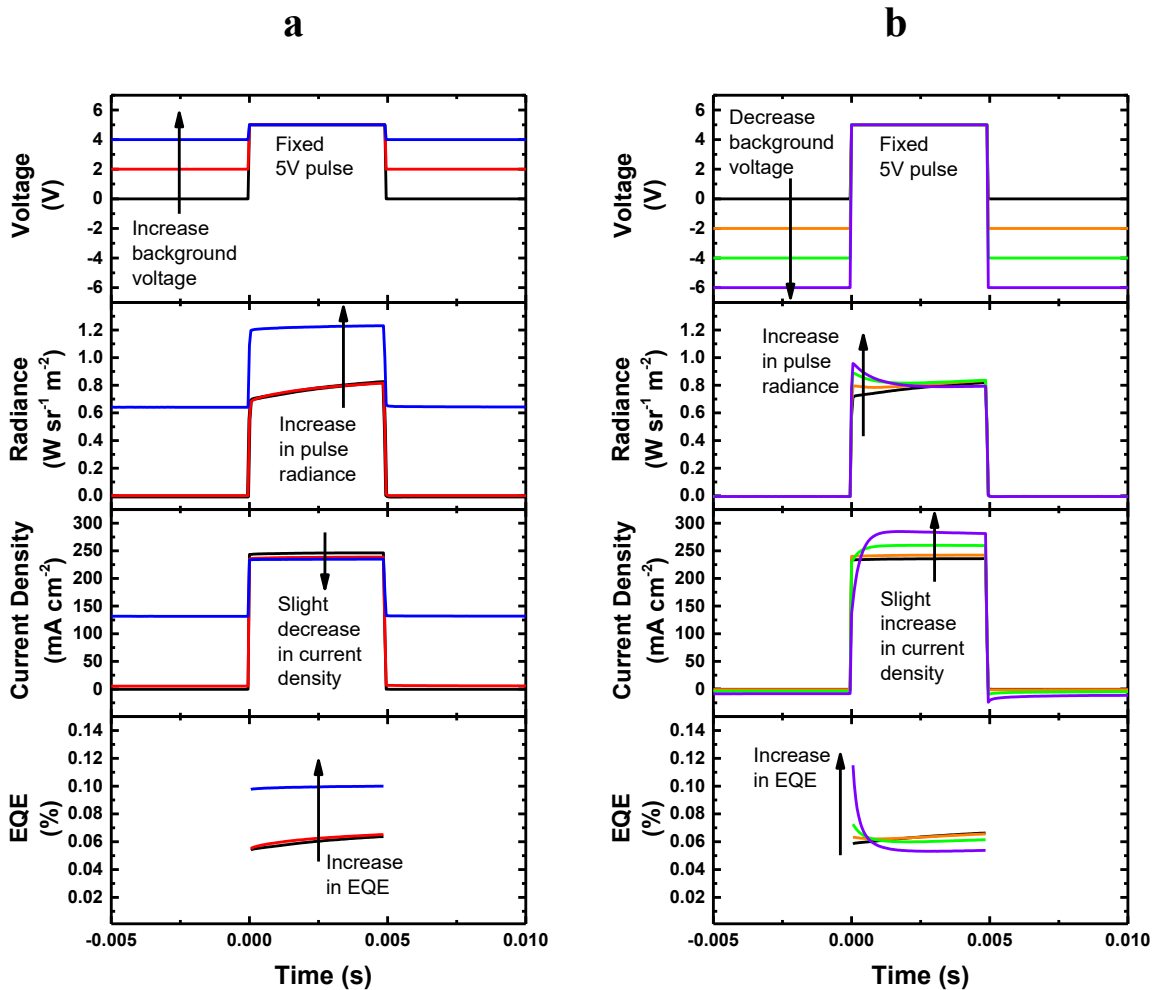

Figure 9-6: In this experiment, a fixed +5 V square voltage pulse with a width of 5 ms and a frequency of 20 Hz was applied to the CH$_3$NH$_3$PbI$_{3-x}$Cl$_x$ PeLED. The background voltage was varied from (a) 0 to +4 V and from (b) 0 to -6 V, and the resulting changes in radiance, current density and EQE were monitored over the duration of the pulse. The profiles of the applied voltage are presented in the top-most graph.

This polarization effect is also reflected in the hysteretic current-voltage characteristics of the PeLED, as shown in Figure 9-7. A potential sweep from forward bias to reverse bias (i.e. larger polarization history to smaller polarization) leads to higher radiance and EQE, compared to a

9.2. Results and Discussion

sweep from reverse to forward bias. We postulate that a high polarization voltage drives the ionic traps out of the bulk emissive layer, therefore suppressing non-radiative trap-mediated recombination and enhancing the radiative bimolecular recombination.
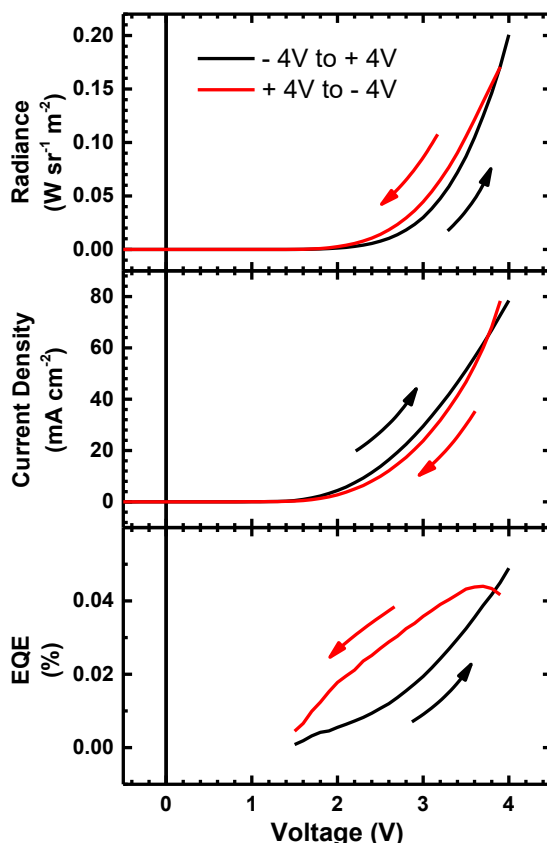

Figure 9-7: Hysteresis effects in radiance, current density and external quantum efficiency during current-voltage measurements. When the device is swept from -4 V (reverse bias) to +4 V (forward bias), the radiance and EQE are lower but the current density is higher, as compared to a voltage sweep from +4 V to -4 V. This is due to the polarization history of the device during the voltage sweep where a history of higher polarization (i.e. +4 V decreasing to -4 V) leads to higher radiance and EQE and a smaller current density, consistent with observations in the pulse experiments.

In our experiments, we observe an increase in EL quantum efficiency with both increasing voltage and increasing current density (see Figure 9-4a and c). In order to investigate the relation of radiative recombination with respect to charge (or excitation) density, we measured photoluminescence quantum efficiency (PLQE) as a function of laser excitation flux (see Figure 9-4c). We used a thin film structure of $TiO_2/CH_3NH_3PbI_{3-x}Cl_x/F8$ that is identical to our devices

for measurement. The PLQE rises with laser photon flux in a trend that is similar to the rise of device quantum efficiency with current density, confirming that high charge densities are essential for efficient radiative recombination. In Figure 9-4c, we compare IQE *vs.* current density in the same plot as PLQE *vs.* absorbed photon flux and find good agreement between the quantum efficiencies obtained via laser excitation and electrical injection. The extrapolation of the IQE suggests that higher electroluminescence quantum efficiency may be achievable at higher current densities. We note that the quantum efficiency of the pulsed device also exhibits the same linear increase with current density, although efficiencies are lower compared to the steady state measurements due to the relatively short 1 ms pulse width used (see Figure 9-5). The lower device EL quantum efficiencies compared to PLQE suggest non-radiative losses by electrical injection, which may be reduced by the optimization of device fabrication process if these losses are predominantly due to high leakage currents.

We have previously demonstrated that radiative recombination in $CH_3NH_3PbI_{3-x}Cl_x$ perovskites is bimolecular in nature.[10] The need for high excitation densities for efficient radiative recombination suggests the presence of a competing non-radiative pathway. Since bimolecular recombination kinetics follow an n^2 relationship (where n = excitation density), a radiative bimolecular pathway can dominate at higher charge densities. With the fluxes produced in our devices, charge densities are relatively low and the competing non-radiative channels dominate, giving rise to a modest EL quantum efficiency.

It is interesting to note that a PLQE of 10 % can be achieved in a $TiO_2/CH_3NH_3PbI_{3-x}Cl_x/F8$ film structure. This is compared to a PLQE of 26 % for a pristine perovskite film of equivalent thickness (15 nm) at an equivalent laser excitation flux. This confirms the formation of a charge confining well structure in our devices, where excitations are only slightly quenched at the heterojunctions, despite an emissive layer thickness of only 15 nm. To further demonstrate the effectiveness of our thin well structure, we fabricated devices using thicker perovskite films

9.2. Results and Discussion

(see Figure 9-8). The radiance and quantum efficiency of the devices decrease markedly at larger perovskite thicknesses, demonstrating the need for spatial confinement of charges to ensure a high rate of electron-hole capture and radiative recombination. In addition, reabsorption losses are likely to be lower in the thinner films.
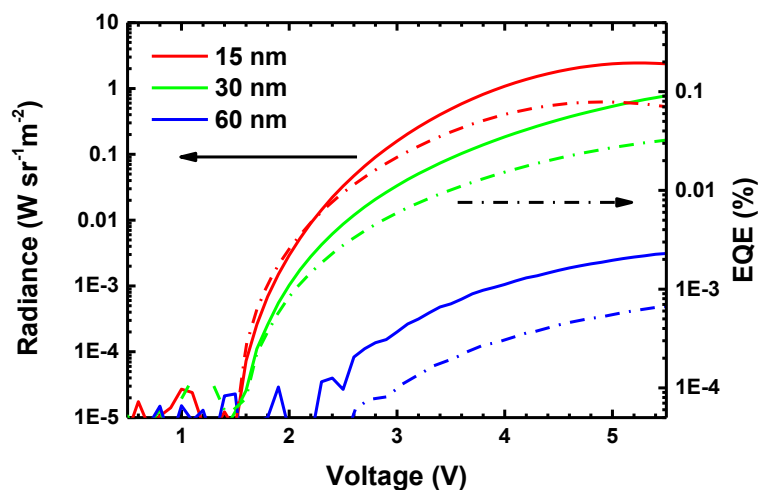

Figure 9-8: Combined plots of radiance vs. voltage (solid lines) and EQE vs. voltage (dash lines) of CH₃NH₃PbI₃₋ₓClₓ PeLED devices with different perovskite layer thicknesses. Both the radiance and the efficiency of the devices decrease at larger perovskite thicknesses. We note that these perovskite films are annealed for a longer time (30 min) to ensure the complete formation of perovskites for the thicker layers.

Our findings so far suggest that higher charge densities, higher polarization and thinner emission layers are possible routes towards enhancing the electroluminescence efficiency. However, we note that the surface coverage of the $CH_3NH_3PbI_{3-x}Cl_x$ perovskite is incomplete (~30 % voids) in such thin layers (see Figure 9-9), causing possible contact between the TiO_2 and F8 layers.
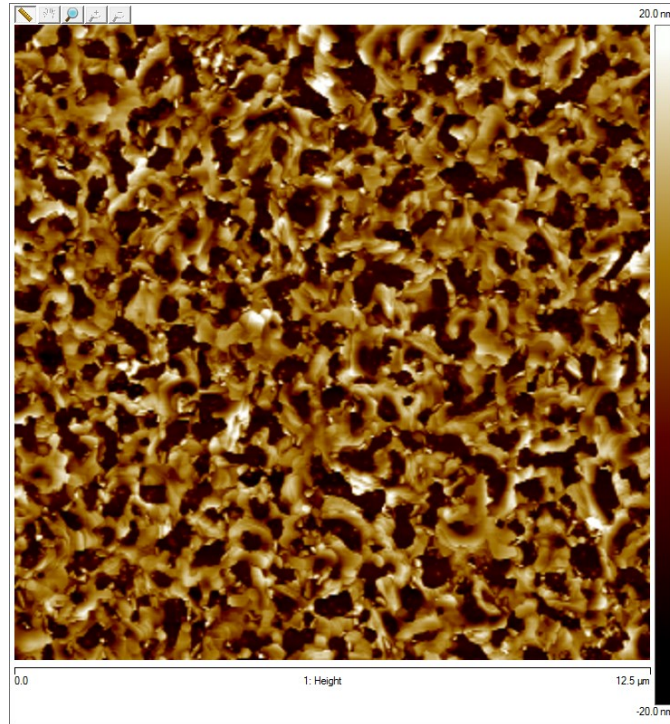
Figure 9-9: Atomic Force Microscopy (AFM) image of the CH₃NH₃PbI₃₋ₓClₓ perovskite thin film, showing incomplete film coverage over a TiO2 coated substrate. Approximately 30 % of the layer is composed of voids.

In order to investigate the effects of electrical shunts at TiO_2/F8 interfaces, we fabricated a TiO_2/F8 device without the thin perovskite interlayer. We find the current density of the TiO_2/F8 device to be several times higher than the perovskite device at forward bias (see Figure 9-10), indicating that there are possible current losses at the TiO_2/F8 interface that do not contribute to electroluminescence. Optimization of thin film formation and morphology towards complete perovskite coverage is therefore expected to enhance device radiance and quantum efficiency. We further note that the EL photon flux from the F8-only device is 3 orders of magnitude lower than the perovskite device, confirming that the F8 layer does not participate in light emission but serves only as a hole transport and electron blocking layer.
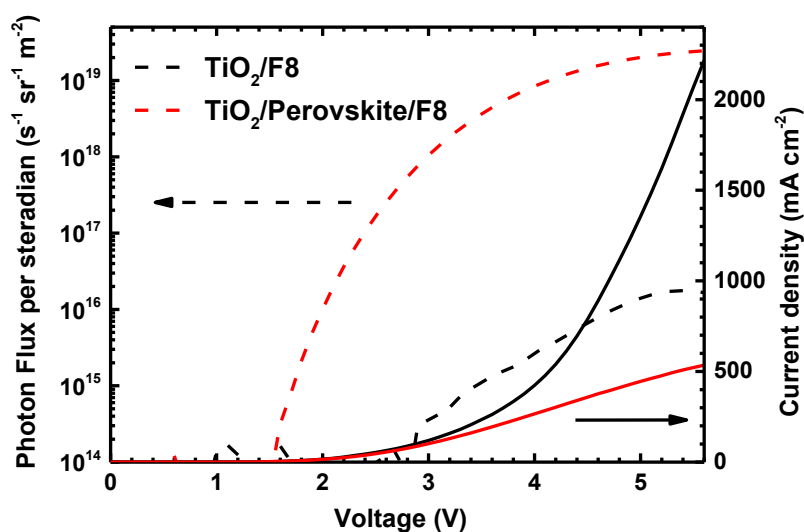
Figure 9-10: Combined photon flux per steradian (dash lines) and current density (solid lines) vs. voltage characteristics of TiO₂/F8 and TiO₂/ CH₃NH₃PbI₃₋ₓClₓ /F8 devices. TiO₂/F8 device gives higher current density compared to the perovskite device. Electroluminescence in TiO₂/F8 device is negligible.

In an effort to optimize our device efficiencies and to minimize luminescence quenching at the TiO₂/perovskite interface, we inserted an ultra-thin (1 nm) layer of Al₂O₃ in between the TiO₂ and the perovskite layers using atomic layer deposition. With this minor modification, we achieved a two-fold enhanced radiance of 13.2 W sr⁻¹ m⁻² at a lower current density of 363 mA cm⁻² (see Figure 9-11). Consequently, the device EQE and IQE increased by more than 3 times to 0.76 % and 3.4 % respectively. This level of performance is comparable or better than some of the best colloidal quantum dot infrared light-emitting devices.[22, 23] This enhancement in luminescent efficiency is likely due to the surface-induced nano-structuring of the perovskite layer[24] and the suppression of luminescence quenching at the TiO₂/perovskite interface.
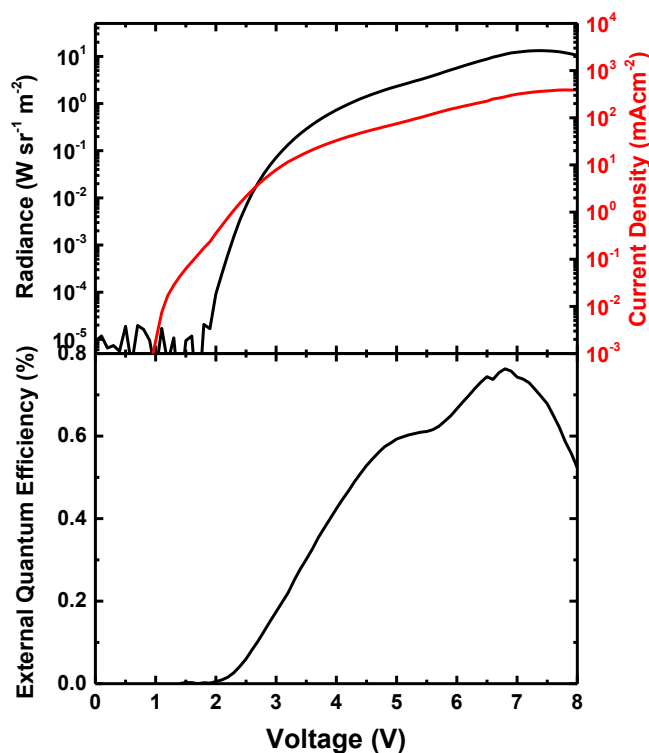
Figure 9-11. Top graph: Combined radiance (black line) and current density (red line) vs. voltage characteristics of a modified ITO/TiO$_2$/Al$_2$O$_3$(1nm)/CH$_3$NH$_3$PbI$_{3-x}$Cl$_x$/F8/MoO$_3$/Ag infrared PeLED. Bottom graph: External quantum efficiency vs. voltage of modified infrared PeLED.

In order to demonstrate the application of organometal halide perovskite as visible light emitters, we utilized the larger bandgap CH$_3$NH$_3$PbBr$_3$ as a green emitter in our PeLED devices. Since a larger bandgap makes it more difficult to achieve electron injection from TiO$_2$ into the perovskite conduction band, we turned to an inverted device structure with an ITO/PEDOT:PSS/CH$_3$NH$_3$PbBr$_3$/F8/Ca/Ag architecture. PEDOT:PSS and calcium were utilized as ohmic hole and electron injectors respectively. The F8 polymer (50 nm) serves as a spacer layer for electron transport and to prevent emission quenching near the Ca metal interface. In order to spatially confine injected charges for efficient radiative recombination, we fabricated CH$_3$NH$_3$PbBr$_3$ to a thickness of 20 nm). As shown in Figure 9-12a, bright green electroluminescence was achieved at 517 nm. The CH$_3$NH$_3$PbBr$_3$ perovskite PL is slightly red-shifted from the EL, peaking at 524 nm with a PLQE of 7 % when excited with a 405 nm blue cw-laser. The device turns on at 3.3 V and reaches a maximum luminance of 364 cd m^{-2} at a

current density of 123 mA cm^{-2}, as shown in Figure 9-12b. This gives an efficiency of 0.3 cd A^{-1}, or an EQE of 0.1 % and IQE of 0.4 % assuming a Lambertian emission profile. Similar to the infrared device, the EL quantum efficiency increases with injection current density (see Figure 9-12c), demonstrating a need for high charge densities to achieve efficient radiative recombination. We also demonstrate red electroluminescence at 630 nm using a CH$_3$NH$_3$PbBr$_2$I mixed halide perovskite in the same device architecture, showing the versatility and wide bandgap tunability of these organometal halide perovskite materials.
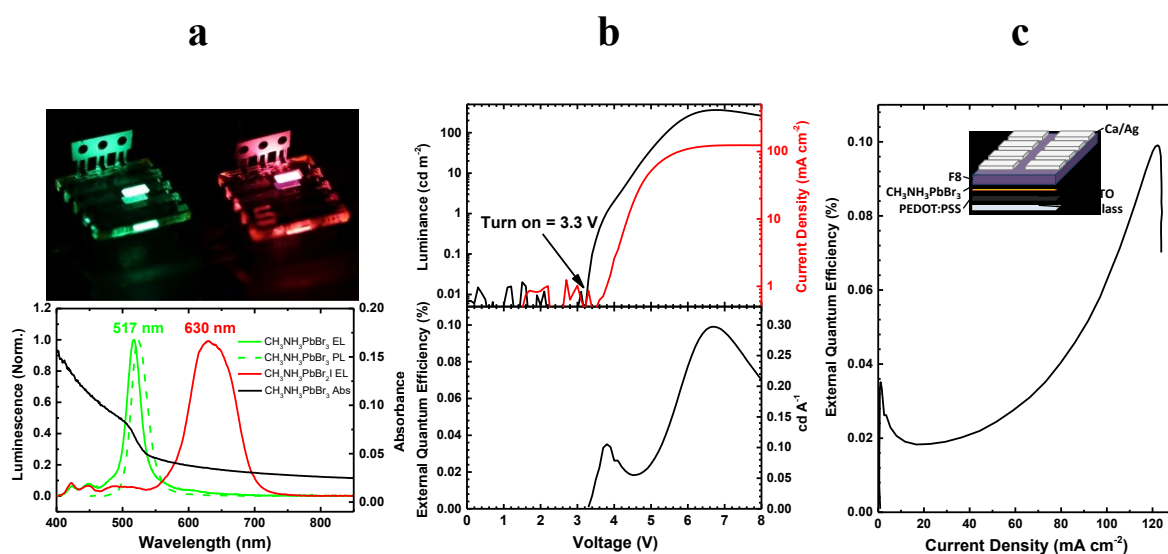
Figure 9-12. (a) Electroluminescence, photoluminescence and absorbance spectra of CH$_3$NH$_3$PbBr$_3$ perovskite on PEDOT:PSS covered substrate. Image shows bright uniform green and red electroluminescence from ITO/PEDOT:PSS/CH$_3$NH$_3$PbBr$_3$/F8/Ca/Ag and ITO/PEDOT:PSS/CH$_3$NH$_3$PbBr$_2$I/F8/Ca/Ag PeLED respectively. (b) Top graph: Combined luminance (black line) and current density (red line) vs. voltage characteristics of green PeLED. Bottom graph: External quantum efficiency vs. voltage of green PeLED. (c) External quantum efficiency vs. current density of green PeLED.

9.3   Conclusion

Our demonstration of bright visible and infrared electroluminescence from organometal halide based perovskite shows great promise in the development of this class of materials for large area optoelectronic or electrically-pumped lasing applications. Furthermore, our work exemplifies the fact that an efficient solar cell material is generally also a good light emitter, as given by the Shockley-Queisser detailed balance limit calculations.[25, 26] It is interesting that

bright electroluminescence could be achieved using a simple thin emitter realized by solution processing. Given the versatility and low-cost processability of these organometal halide perovskite materials, they may quickly find their way into the displays and lighting industry.

9.4 Experimental Section

F8 polymer was provided by Cambridge Display Technology (CDT) and was used as received. All other chemicals were purchased from Sigma-Aldrich and were used as received.

$CH_3NH_3PbI_{3-x}Cl_x$ Perovskite Synthesis.

Methylammonium iodide (CH_3NH_3I) was prepared by adding 33 wt % methylamine solution in ethanol (24 mL) and 57 wt % hydroiodic acid in water (10 mL) to 100 mL of absolute ethanol. The reaction mixture was stirred at room temperature in a nitrogen atmosphere. The solvent was removed by rotary evaporation until white crystals started to appear. The product was collected using Büchner funnel filtration and was dried overnight under vacuum at 80 °C. The mixed halide perovskite precursor solution was prepared by mixing CH_3NH_3I and $PbCl_2$ in a 3:1 molar ratio in anhydrous N,N-dimethylformamide to give a concentration of 5 wt %.

$CH_3NH_3PbBr_3$ Perovskite Synthesis.

Methylammonium bromide (CH_3NH_3Br) was prepared by adding 33 wt % methylamine solution in ethanol (24 mL) and 48 wt % hydrobromic acid in water (8.5 mL) to 100 mL of absolute ethanol. The reaction mixture was stirred at room temperature. The solvent was removed by rotary evaporation. The obtained white crystals were washed with anhydrous diethyl ether and recrystallized in ethanol. The perovskite precursor solution was prepared by mixing CH_3NH_3Br and $PbBr_2$ in a 3:1 molar ratio in anhydrous N,N-dimethylformamide to give a concentration of 5 wt %. For the $CH_3NH_3PbBr_2I$ mixed-halide precursor solution, we

9.4. Experimental Section

mixed the individual $CH_3NH_3PbBr_3$ and $CH_3NH_3PbI_3$ precursor solutions in a molar ratio of 2:1 to give an overall concentration of 5 wt %.

Infrared PeLED Fabrication.

ITO coated glass substrates were cleaned successively with acetone and isopropanol. TiO_2 (25 nm) was grown onto the cleaned substrates at 225 °C with atomic layer deposition (ALD), using titanium tetrachloride ($TiCl_4$) and water as precursors. The substrates were transferred into a nitrogen filled glovebox for further fabrication. The *$CH_3NH_3PbI_{3-x}Cl_x$* perovskite precursor solution was spin coated onto the TiO_2 at 3000 rpm for 60 seconds, and annealed at 100 °C for 5 minutes to give a thin perovskite film with an average thickness of ~15 nm, as determined by atomic force microscopy (AFM). A solution of F8 in chlorobenzene (10 mg/mL) was spin coated onto the perovskite layer at 3000 rpm for 60 seconds to give a 50 nm film. MoO_3 (5 nm) and Ag (100 nm) were successively deposited by vacuum thermal evaporation. Devices were tested in air without encapsulation.

Green PeLED Fabrication.

ITO coated glass substrates were cleaned successively with acetone and isopropanol, followed by 10 minutes oxygen plasma treatment. PEDOT:PSS (Clevios P VP AI 4083) was spin coated onto the substrate at 6000 rpm for 30 seconds, and annealed at 140 °C for 30 minutes in a nitrogen atmosphere. The $CH_3NH_3PbBr_3$ perovskite precursor solution was spin coated onto PEDOT:PSS at 3000 rpm for 30 seconds and annealed at 100 °C for 15 minutes to give a perovskite film thickness of ~20 nm. A solution of F8 in chlorobenzene (10 mg/mL) was spin coated onto the perovskite layer at 3000 rpm for 30 seconds to give a 50 nm film. Ca (20 nm) and Ag (100 nm) were successively deposited by vacuum thermal evaporation. Devices were tested in air without encapsulation.

PeLED Characterization.

Current *vs.* voltage characteristics were measured using a Keithley 2400 Source Measure Unit (SMU). Photon flux was measured simultaneously using a calibrated silicon photodiode centered over the light-emitting pixel. Radiance in W sr^{-1} m^{-2} and luminance in cd m^{-2} were calculated based on the emission function of the PeLED, and on the known spectral response of the silicon photodiode. External quantum efficiency was calculated, assuming a Lambertian emission profile. Electroluminescence spectra were measured using a Labsphere CDS-610 spectrometer.

PLQE Measurement.

The PLQE of the thin film samples was measured using an integrating sphere method, as reported in the literature.[20] A continuous wave 532 nm green diode laser with an excitation power of 10 – 100 mW and a focused beam spot of ~0.3 mm^2 was used to photo-excite the samples. Emission was measured using an Andor iDus DU490A InGaAs detector. During measurements, the samples were kept at room temperature under a constant stream of nitrogen. Samples were prepared in the structure TiO$_2$/CH$_3$NH$_3$PbI$_{3-x}$Cl$_x$/F8 on top of a spectrosil fused silica substrate, similar to the PeLED device structure.

Pulse LED Measurement.

A square voltage pulse with a pulse width of 1 ms and frequency of 100 Hz was applied to the device using a HP8116A Pulse/Function generator. A dual-channel Agilent Technologies DSO6032A oscilloscope, set to 50 Ω impedance, was connected in series to the device and the function generator to determine the current through the device. The electroluminescence was monitored using a calibrated Si photodiode, connected to the 2nd channel of the oscilloscope (1 MΩ) via a Thorlabs PDA200C photodiode amplifier.

9.5 Literature

[1] M. M. Lee, J. Teuscher, T. Miyasaka, T. N. Murakami, H. J. Snaith, *Science* **2012**, *338*, 643.

[2] H.-S. Kim, C.-R. Lee, J.-H. Im, K.-B. Lee, T. Moehl, A. Marchioro, S.-J. Moon, R. Humphry-Baker, J.-H. Yum, J. E. Moser, M. Gratzel, N.-G. Park, *Sci. Rep.* **2012**, *2*.

[3] J. Burschka, N. Pellet, S.-J. Moon, R. Humphry-Baker, P. Gao, M. K. Nazeeruddin, M. Gratzel, *Nature* **2013**, *499*, 316.

[4] M. Liu, M. B. Johnston, H. J. Snaith, *Nature* **2013**, *501*, 395.

[5] S. D. Stranks, G. E. Eperon, G. Grancini, C. Menelaou, M. J. P. Alcocer, T. Leijtens, L. M. Herz, A. Petrozza, H. J. Snaith, *Science* **2013**, *342*, 341.

[6] G. Xing, N. Mathews, S. Sun, S. S. Lim, Y. M. Lam, M. Grätzel, S. Mhaisalkar, T. C. Sum, *Science* **2013**, *342*, 344.

[7] J. H. Heo, S. H. Im, J. H. Noh, T. N. Mandal, C.-S. Lim, J. A. Chang, Y. H. Lee, H.-j. Kim, A. Sarkar, K. NazeeruddinMd, M. Gratzel, S. I. Seok, *Nat. Photon.* **2013**, *7*, 486.

[8] C. C. Stoumpos, C. D. Malliakas, M. G. Kanatzidis, *Inorg. Chem.* **2013**, *52*, 9019.

[9] J. H. Noh, S. H. Im, J. H. Heo, T. N. Mandal, S. I. Seok, *Nano Lett.* **2013**, *13*, 1764.

[10] F. Deschler, M. Price, S. Pathak, L. E. Klintberg, D.-D. Jarausch, R. Higler, S. Hüttner, T. Leijtens, S. D. Stranks, H. J. Snaith, M. Atatüre, R. T. Phillips, R. H. Friend, *J. Phys. Chem. Lett.* **2014**, *5*, 1421.

[11] L. C. Schmidt, A. Pertegás, S. González-Carrero, O. Malinkiewicz, S. Agouram, G. Mínguez Espallargas, H. J. Bolink, R. E. Galian, J. Pérez-Prieto, *J. Am. Chem. Soc.* **2014**, *136*, 850.

[12] M. Era, S. Morimoto, T. Tsutsui, S. Saito, *Appl. Phys. Lett.* **1994**, *65*, 676.

[13] T. Hattori, T. Taira, M. Era, T. Tsutsui, S. Saito, *Chem. Phys. Lett.* **1996**, *254*, 103.

[14] K. Chondroudis, D. B. Mitzi, *Chem. Mater.* **1999**, *11*, 3028.

[15] K. Tanaka, T. Takahashi, T. Ban, T. Kondo, K. Uchida, N. Miura, *Solid State Commun.* **2003**, *127*, 619.

[16] M. Hirasawa, T. Ishihara, T. Goto, K. Uchida, N. Miura, *Phys. B* **1994**, *201*, 427.

[17] L.-P. Lu, D. Kabra, K. Johnson, R. H. Friend, *Adv. Funct. Mater.* **2012**, *22*, 144.

[18] A. Abrusci, S. D. Stranks, P. Docampo, H.-L. Yip, A. K. Y. Jen, H. J. Snaith, *Nano Lett.* **2013**, *13*, 3124.

[19] J. Hwang, E.-G. Kim, J. Liu, J.-L. Brédas, A. Duggal, A. Kahn, *J. Phys. Chem. C* **2006**, *111*, 1378.

[20]   J. C. de Mello, H. F. Wittmann, R. H. Friend, *Adv. Mater.* **1997**, *9*, 230.

[21]   N. C. Greenham, R. H. Friend, D. D. C. Bradley, *Adv. Mater.* **1994**, *6*, 491.

[22]   N. Tessler, V. Medvedev, M. Kazes, S. Kan, U. Banin, *Science* **2002**, *295*, 1506.

[23]   L. Sun, J. J. Choi, D. Stachnik, A. C. Bartnik, B.-R. Hyun, G. G. Malliaras, T. Hanrath, F. W. Wise, *Nat. Nanotechnol.* **2012**, *7*, 369.

[24]   J. J. Choi, X. Yang, Z. M. Norman, S. J. L. Billinge, J. S. Owen, *Nano Lett.* **2013**, *14*, 127.

[25]   W. Shockley, H. J. Queisser, *J. Appl. Phys.* **1961**, *32*, 510.

[26]   O. D. Miller, E. Yablonovitch, S. R. Kurtz, *IEEE J. Photovoltaics* **2012**, *2*, 303.

10 Conclusion

This thesis focused on the preparation of hybrid organic-inorganic perovskites and their application in solution processed thin film solar cells. In the beginning, a new 2-step deposition approach for a facile, efficient and low-temperature synthesis of thin film perovskite materials is introduced. In the first step, a thin layer of the lead precursor is deposited on the substrate and converted into the perovskite phase by immersion into a solution of the other structural components in the second step.

This preparation pathway produced films with 100 % surface coverage and the fabricated solar cells achieved 15 % efficiency. It was observed that the temperature of the immersion bath has a critical influence on the orientation of the individual perovskite crystals on the surface. Depending on the crystal orientation the efficiencies varied, while the highest efficiency was achieved with an orientation of the long axis of the tetragonal unit cell perpendicular to the surface.

Although the perovskite synthesis was already performed at low temperatures, the electron selective contact still required a high temperature sintering step. It was possible to substitute this layer with a solution processed fullerene layer, while still maintaining reasonable efficiencies of around 10 %. It was, however, necessary to photopolymerize the fullerene layer to obtain a high degree of reproducibility. The polymerization reaction reduces the solubility of the fullerene in the following steps and therefore prevents the formation of pinholes in the electron selective contact.

Furthermore, the band-gap tunability of $MAPbI_3$ by substituting part of the iodide with bromide was investigated. A change in band-gap energy from 1.5 eV (pure iodide) to 2.25 eV (pure

bromide) was observed. Independent of the degree of substitution, pure phases of the mixed halide perovskites are formed, as proven by photothermal deflection spectroscopy (PDS).

The pure bromide perovskite $MAPbBr_3$, however, is not suitable for the fabrication of planar heterojunction solar cells. The diffusion length of the electrons and holes does not suffice to ensure efficient charge extraction. It was possible to increase the diffusion length by substituting the MA cation with formamidinium. The resulting perovskite $FAPbBr_3$ is structurally and energetically very similar to $MAPbBr_3$. Due to the increased lifetime of the photoexcited species, however, the efficiency of the resulting solar cells is improved from about 1 % for $MAPbBr_3$ to 7 % for the FA-based compound.

In the end, a different application of perovskite materials is presented. When the semiconducting material is prepared as a thin film between two charge injection layers, the excess electrons and holes recombine and light is emitted. This has been shown for $MAPbBr_3$ and a mixture of bromide and iodide perovskite. The observed light emission was green and red, respectively.

Although the almost exponential increase in solar cell efficiencies for the demonstrated perovskite materials is very impressive, they are still far from being industrially produced and employed in large installations. One important reason relates to the toxicity of lead, especially since it is soluble in water. To make perovskite-based solar cells more attractive, alternative structures using non-toxic metal cations have to be found. First results suggest that tin-based perovskites could be an attractive alternative, already achieving efficiencies around 6 %.

The efficiencies of the best lead-based perovskite solar cells are already getting close to the maximum theoretically achievable efficiency. One attractive way of bypassing this limit is the combination of perovskite absorbers with conventional photovoltaic technologies in tandem

structures. Calculations show that the use of state-of-the-art perovskite cells on a silicon or CIGS bottom cell could potentially lead to efficiencies of up to 30 %.

There will still be much research necessary in the next years to overcome the problems presented by perovskite solar cells. However, looking at the 4 years of research invested so far in perovskites compared to almost 50 years of silicon solar cell research and the achieved efficiencies for both technologies, there are good reasons to be optimistic and curious about the future developments.

11 Publications and Presentations

11.1 Journals

1. "Efficient Planar Heterojunction Perovskite Solar Cells Based on Formamidinium Lead Bromide"

   F. C. Hanusch, E. Wiesenmayer, E. Mankel, A. Binek, P. Angloher, C. Fraunhofer, N. Giesbrecht, J. M. Feckl, W. Jaegermann, D. Johrendt, T. Bein and P. Docampo, *J. Phys. Chem. Lett.*, **2014**, 5, 2791-2795.

2. "Solution Deposition-Conversion for Planar Heterojunction Mixed Halide Perovskite Solar Cells"

   P. Docampo, F. Hanusch, S. D. Stranks, M. Döblinger, J. M. Feckl, M. Ehrensperger, N. K. Minar, M. B. Johnston, H. J. Snaith and T. Bein, *Adv. Energy Mater.*, **2014**, 4, DOI: 10.1002/aenm.201400355.

3. "Influence of the Orientation of Methylammonium Lead Iodide Perovskite Crystals on Solar Cell Performance"

   P. Docampo, F. C. Hanusch, N. Giesbrecht, P. Angloher, A. Ivanova and T. Bein, *APL Mater.*, **2014**, 2, 081508.

4. "Stabilization of the Trigonal High-Temperature Phase of Formamidinium Lead Iodide"

   A. Binek, F. C. Hanusch, P. Docampo and T. Bein, *J. Phys. Chem. Lett.*, **2015**, 6, 1249-1253.

5. "A Closer Look into Two-Step Perovskite Conversion with X-ray Scattering"

J. Schlipf, P. Docampo, C. J. Schaffer, V. Körstgens, L. Bießmann, F. Hanusch, N. Giesbrecht, S. Bernstorff, T. Bein and P. Müller-Buschbaum, *J. Phys. Chem. Lett.*, **2015**, 6, 1265-1269.

6. "Preparation of Single-Phase Films of CH_3NH_3Pb $(I_{1-x}Br_x)_3$ with Sharp Optical Band Edges"

A. Sadhanala, F. Deschler, T. H. Thomas, S. n. E. Dutton, K. C. Goedel, F. C. Hanusch, M. L. Lai, U. Steiner, T. Bein, P. Docampo D. Cahen and R. H. Friend, *J. Phys. Chem. Lett.*, **2014**, 5, 2501-2505.

7. "Bright Light-Emitting Diodes based on Organometal Halide Perovskite"

Z. K. Tan, R. S. Moghaddam, M. L. Lai, P. Docampo, R. Higler, F. Deschler, M. Price, A. Sadhanala, L. M. Pazos, D. Credgington, F. Hanusch, T. Bein, H. J. Snaith and R. H. Friend, *Nat. Nanotechnol.*, **2014**, 9, 687-92.

8. "A Highly-Ordered 3D Covalent Fullerene Framework"

N. K. Minar, K. Hou, C. Westermeier, M. Döblinger, J. Schuster, F. C. Hanusch, B. Nickel, G. A. Ozin and T. Bein, *Angew. Chem.*, **2015**, *54*, 7577-7581.

11.2 Bookchapter

F. C. Hanusch, M. L. Petrus, P. Docampo (2015). *Towards Optimum Solution-processed Planar Heterojunction Perovskite Solar Cells.* in E. da Como, F. de Angelis, H. Snaith and A. Walker (Eds.), *Unconventional Thin Film Photovoltaics: Organic and Perovskite Solar Cells*. Cambridge, UK.

11.3 Patents

Z. K. Tan, R. S. Moghaddam, M. L. Lai, P. Docampo, F. Deschler, M. Price, A. Sadhanala, F. Hanusch, H. J. Snaith, R. H. Friend. *Electroluminescent Device*. WO2015166006A1, **2015**.

11.4 Oral presentations

1. Low temperature solution based synthesis of thin film MAPbI3 perovskite solar cells
   Fabian Hanusch, Pablo Docampo, Samuel D. Stranks, Henry Snaith, Thomas Bein

   6th international Conference on Hybrid and Organic Photovoltaics (HOPV), **2014,** Sevilla, Spanien.

2. Low temperature solution based synthesis of thin film MAPbI$_3$ perovskite solar cells
   Fabian Hanusch, Pablo Docampo, Samuel D. Stranks, Henry Snaith, Thomas Bein

   E-MRS Spring Meeting, **2014**,Lille, Frankreich.

3. Development of Novel Materials for Perovskite-based Photovoltaics

   Fabian Hanusch, Michiel L. Petrus, Pablo Docampo, Thomas Bein

   Soltech Workshop, 2015, Wildbad Kreuth, Deutschland.

4. Efficient and planar wide bandgap perovskite solar cells

   Fabian Hanusch, Thomas Bein, Pablo Docampo

   MRS Spring Meeting, San Francisco, USA.

11.5 Poster presentations

1. Polymerization of fullerene in various mesoporous hosts.

   Fabian Hanusch, Thomas Bein

   CeNS Workshop "Nanosciences: Soft, Solid, Alive and Kicking", **2012**, Venice, Italy.

2. Polymerization of fullerene in various mesoporous hosts.

Fabian Hanusch, Thomas Bein

25. Deutsche Zeolith-Tagung, **2010**, Hamburg, Germany.

3. in situ photopolymerization of C_{60}.

Fabian Hanusch, Thomas Bein

Soltech Workshop, 2013, Kloster Banz, Germany.

4. in situ photopolymerization of C_{60}.

Fabian Hanusch, Thomas Bein

CeNS Workshop "Nanosciences: Great Adventures on Small Scales", **2013**, Venice, Italy.

5. Low temperature solution based synthesis of thin film $MAPbI_3$ perovskite solar cells.

Fabian Hanusch, Pablo Docampo, Samuel D. Stranks, Henry Snaith, Thomas Bein

Soltech Workshop, 2014, Wildbad Kreuth, Germany.

6. Nanostructuring for new perovskite solar cell absorber materials.

Fabian Hanusch, Benjamin Mandlmeier, Alesja Ivanova, Pablo Docampo, Thomas Bein

CeNS Workshop "Walk and Talk at the Nanoscale", **2014**, Venice, Italy.

7. Efficient wide bandgap perovskite solar cells.

Fabian Hanusch, Pablo Docampo, Erwin Wiesenmayer, Eric Mankel, Andreas Binek, Philipp Angloher, Christina Fraunhofer, Nadja Giesbrecht, Johann M. Feckl, Wolfram Jaegermann Dirk Johrendt, Thomas Bein

International Conference Solution processed Semiconductor Solar Cells (SSSC), **2014**, Oxford, UK.

8. Efficient and planar wide bandgap perovskite solar cells.

Fabian Hanusch, Thomas Bein, Pablo Docampo

Soltech Workshop, 2015, Kloster Banz, Germany.